Summer 8-2024

Bi-Modal Excitation of a Supersonic Rectangular Jet

Benjamin Malczewski
Embry-Riddle Aeronautical University, malczewb@my.erau.edu

Bi-Modal Excitation of a Supersonic Rectangular Jet

By

Benjamin Malczewski

A Dissertation Submitted to the Faculty of Embry-Riddle Aeronautical University

In Partial Fulfillment of the Requirements for the Degree of

Doctor of Philosophy in Aerospace Engineering

August 2024

Embry-Riddle Aeronautical University

Daytona Beach, Florida

To my family who has always encouraged me to push the boundaries of what I am capable of

ACKNOWLEDGMENTS

Financial support is provided by the Office of Naval Research under Grant No. N00014-21-1-2102 monitored by Dr. Steven Martens. Computations were carried out using Embry-Riddle's VEGA system and DoD HPC.

ABSTRACT

This work addresses the issue of supersonic rectangular jet noise via bi-modal excitation. A Mach 1.5 heated rectangular jet with a 2:1 aspect ratio is considered. Theoretical work is presented in which a Reduced-Order Model (ROM) is used in conjunction with the Linearized Euler Equations to predict the nonlinear growth and decay of various frequencies due to the interaction between harmonically related modes and the mean flow. Scope is limited to a symmetric disturbance. The case of no interaction is used to help identify a dominant coherent structure, referred to as "f". For the symmetric disturbance, a Strouhal number of 0.15, based on the height of the jet, is found to be the most amplified frequency. The ROM is then used including interaction where either the subharmonic (f/2) or harmonic (2f) are added to reduce "f". It was found that adding harmonics are effective at reducing the peak of the fundamental depending on the initial phase angle. By assuming "f" to be the dominant noise source, it is possible that this is an effective noise reduction mechanism.

To validate the ROM, Large-Eddy Simulations (LES) are conducted starting with a previously validated case. The unexcited case is first considered. Using FFT, Strouhal number 0.15 is identified as the dominant coherent structure in the near field, which is consistent with the ROM. However in the far field, $St_H = 0.25$ appears as the dominant frequency at the peak emissivity angle, though $St_H = 0.15$ still appeared as a secondary peak and dominated lower angles. The ROM shows the requirement of natural amplification, thus $St_H = 0.15$ is taken as the fundamental. Based on guidance from the ROM, the jet is excited with the harmonic, $St_H = 0.30$, assuming $St_H = 0.15$ to be naturally amplified. A second set of cases is considered where both $St_H = 0.30$ and $St_H = 0.15$ are excited with varying initial phase lags. In both cases, excitation is imposed using a pressure fluctuation. For all excitation cases, the coherent structure at $St_H = 0.15$ in the near field, and the amount of reduction correlates to the amount of amplification of $St_H = 0.30$, supporting the proposal of energy exchange between the two modes. In the far field, peak noise in the minor plane is not reduced since $St_H = 0.25$ was not reduced. However, considerable noise reduction is

observed at lower emissivity angles up to 2dB. It is shown that this noise reduction comes from reductions in $St_H = 0.15$, which was the intended effect of the excitation.

The final aspect of this work focuses on the use of a feed-forward controller to control the actuation. Excitation studies have traditionally used open-loop control where only a single frequency is excited with an analytic function. There are very few published studies that have used real time sensing to excite jet flows. In this work, 4 actuators are placed along the span of the upper and lower nozzle surfaces for a total of 8 actuators. Upstream, each actuator has its own sensor that read the instantaneous pressure disturbance. Each actuator then responds with the opposite of that pressure disturbance, but out of phase 180°. In addition, the actuator response is scaled with a proportional gain constant, K_p. In the near field, all feed-forward cases with positive gain values reduced the RMS pressure fluctuations in the initial shear layer, whereas the single-mode excitation increased it. The reduction in downstream pressure fluctuations is shown to have effects with the best results coming from $K_p = 1.0$. For all feed-forward cases, the near field reductions occur for a broad range of Strouhal numbers in the range of the peak radiated noise. In the far field, the feed-forward cases successfully reduced the low-angle noise by up to 2dB for the case of $K_p = 1.0$. Analysis of spectra shows that the feed-forward cases reduce a broad range of Strouhal numbers. The feed-forward case with $K_p = 1.0$ ultimately reduced the noise by more and for a wider range of Strouhal numbers than the single-mode excitation case. An additional set of cases with negative gain values are considered to create additive waves. Near field reduction is considerably lower for these cases and the minor plane far field noise was amplified. Amplification occurred for a large range of Strouhal numbers. It is ultimately suggested that the feed-forward control with gain values close to 1.0 can effectively reduce the noise.

TABLE OF CONTENTS

LIST OF FIGURES

Figure **Page**

NOMENCLATURE

α	Streamwise wavenumber
β_0	Initial phase lag, rad
μ	Dynamic viscosity
ω	Angular frequency, rad/s
ψ	Streamwise phase function
ρ	Density, kg/m^3
θ	Momentum thickness
$\widetilde{r}_{ij}$	Reynolds stress
E	Amplitude
g	Generic flow variable
H	Jet height, m
I	Integral term
K, Q, q	Mean flow, large-scale structure, and fine-scale turbulence kinetic energy
m	Frequency mode
n	Spanwise wavenumber
p	Pressure, Pa
Re	Reynolds number
St_H	Strouhal number based on height
t	Time, s

u, v, w Streamwise, transverse, and spanwise velocity components

x, y, z Streamwise, transverse, and spanwise directions, m

1 Introduction

Jet noise is a major concern in both civilian and military aviation. Jet noise a nuisance to those living near airstrips and can result in adverse health effects on personnel working near aircraft. The focus of this work is active noise reduction in supersonic rectangular jets, which is of particular interest for military applications. The rectangular jet is of interest due to it being easier to manufacture and integrate into an airframe.

A specific use case for this work is to reduce noise of jets taking off from aircraft carriers. Carrier decks regularly see personnel working in close proximity to aircraft during takeoff where noise levels can reach above 150 dB. This is beyond the noise levels that personal protective equipment can protect against. The U.S. Department of Veterans Affairs spends approximately $1 billion per year on hearing loss cases with around 28% coming from the Department of the Navy [3]. Ideally, any noise reduction technology that comes from this work can be actively turned on during takeoff while having minimal impact on vehicle thrust.

Jet noise is a very complex problem. The dominant noise is generated by the large-scale coherent structures [4], which can be characterized as wave packets of various frequencies and azimuthal mode that can interact with each other as well as the mean flow and fine-scale turbulence (Mankbadi, 1991). In supersonic jets, noise is distinguished between mixing noise and shock associated noise. Mixing noise is generated from convecting quadrupole sources as originally proposed by Lighthill [5]. Shock associated noise is generated by the interaction between large-scale structures in the shear layer and the shock cells in the jet core [6, 7]. Gojon et al. [8] show where these different types of noise originate in the near field and propagate to the far field. They show the mixing noise generated further downstream and appearing at low directivity angles. The shock associated noise appears further upstream and is dominant at higher polar angles and contains higher frequency components.

1.1 Review of Computational Aeroacoustics

This work examines jet noise using computations rather than experiments. Computational Aeroacoustics (CAA) offers several tools with varying levels of accuracy and com-

putational expense. On the highest end of expense, but also the highest fidelity are Direct Numerical Simulations (DNS). DNS resolves turbulence all the way down to the Kolmogorov scales, but doing so requires very fine computational grids. This generally restricts these type of simulations to low Reynolds number flows [9]. Large-Eddy Simulations (LES) offer the ability to resolve large-scale turbulence and model the fine scales. The large-scale turbulence is the primary source of noise in the jet [5, 10], making LES one of the best methods for computing noise sources. Although more cost-effective compared to DNS, LES cases still require significant computational resources, especially when analyzing 3-dimensional cases. An example of the computational expense is shown by Nichols et al. [11], who ran a supersonic jet with up to 80M control volumes on up to 20,000 processors. Even in the present study, the computational grid consists of roughly 300M nodes and is run using 1024 processors. It takes around 7 days time to run a case for a duration of $330D_{eq}/U_{jet}$. Some reviews of LES for jet noise and computational methods can be found in Refs. [12–15].

Another set of CAA tools are the Linearized Euler Equations (LEE), whereby the Euler equations are linearized about a mean flow. Governing equations and numerical methods for LEE can be found in several previous publications [16–20]. LEE is more computationally affordable than LES, but there are trade offs. Being linear, LEE cannot accurately predict nonlinear interactions between multiple frequency components of the turbulence. Another drawback of LEE is that it does not have a way to handle shocks that may be present in the underlying mean flow, which affects the linear growth of disturbances. This limitation is later shown in the present work in Sec. 3.2.1. However, LEE can reasonably predict far field directivity for a single frequency if that frequency is chosen close to the peak radiated frequency (i.e. obtained froma higher fidelity study). This was shown by Mankbadi et al. [21] and more recently by Salehian et al. [20]. In linear flow regions, LEE can also be used as an alternative extension technique as was done by Shih et al. [22]. Of more relevance to this work is that LEE can also be used to obtain disturbance shapes in the jet when considering a single frequency, which was previously done by Dahl et al. [23].

1.2 Review of Rectangular Jets

There are multiple features of rectangular jets that set them apart from axisymmetric jets. An earlier experimental study on supersonic rectangular jets by Gutmark et al. [24] found the jet to be nearly symmetric near sonic conditions. As the Mach number increased, flapping in the minor plane of the jet was observed as well as a screech tone propagating upstream, while the major plane remained symmetric. More recent works have also found screech tones in rectangular jets to be asymmetric [8, 25], previous work by Raman and Rice [26] found the instability mode in a shear layer at the screech frequency to also be asymmetric. Another common phenomenon observed in rectangular jets is axis switching whereby the plume starts with a rectangular cross section in oriented one direction and then switches to rectangular in the direction 90° to the original. Axis switching is not always observed, though it is more common in higher aspect ratio jets. Nichols et al. [11] did not observe axis switching on their Mach 1.4 jet with a 4:1 aspect ratio while Chakrabarti et al. [27] for a Mach 1.3 jet and Wu et al. [28] for a Mach 1.69 jet of the same aspect ratio did. For the same jet considered in this work with an aspect ratio of 2, Chakrabarti et al. [29] did not observe axis switching.

Jet flows can be decomposed into azimuthal modes with different energy levels. Most of the energy is contained in the first 5-7 modes, with much of it contained within the 1st and 2nd mode [27]. It's also been shown that higher modes damp out further downstream, and that the far field acoustics are closer to symmetric [29]. However, the first screech mode in a supersonic rectangular jet has been shown to be asymmetric [25, 26]. Many of the past experimental works have focused on exciting at moderate to high frequencies that are more in line with the screech frequency, for which it has been found to be more effective to excite with flapping or helical modes [30]. Chakrabarti et al. [27] also showed that the large-scale structure (LSS) accounts for the low frequency noise from the jet, corresponding to the jet column mode, which is considered in the present work.

1.3 Active Noise Control in Jets

Active research areas for jet noise reduction include passive methods such as chevrons at the nozzle exit [31, 32] and shielding noise with an airframe [1, 33, 34]. Of more relevance to this work is the use of the active noise control method, excitation, where a disturbance is forced. Much of the early work on active control began with low-speed round jets. Early experiments on low-speed round jets have found that two-frequency excitation can be more effective than single-frequency and that initial amplitude and phase angle play a significant role in whether the subharmonics are suppressed or amplified [35]. An early example of excitation in computations is given in Mankbadi et al. [36] where LES of a supersonic round jet had a forced inflow disturbance.

In experiments, plasma actuators have been used with much success to excite high speed round jets and have shown ability to reduce peak noise [37–39]. This same group has also found success using plasma actuators for twin rectangular jets [25, 40]. These plasma actuators have also been explored computationally for supersonic round jets [41, 42]. Other experiments by Sinha et al. [43] on a single rectangular jet have found steady blowing effective in reducing noise, while unsteady blowing resulted in additive tones. More recently Prasad and Unnikrishnan [44] performed excited LES of a supersonic rectangular jet, replicating the use of plasma actuators in computation, found that unsteady excitation could reduce the peak noise at small amplitudes depending on the forcing frequency. The present work is significant in that it is the first LES computations of multi-frequency excitation in a supersonic rectangular jet and one of only a handful of computational studies on excited rectangular jets.

Past theoretical work has given insight to the mechanism by which waves of different modes in a jet interact with one another, the mean flow, and background turbulence. For a turbulent round jet, a set of differential equations was developed using an integral technique, which described the nonlinear amplitudes of a fundamental and subharmonic wave along the length of the jet, where it was shown that adding subharmonics could amplify the

fundamental depending on initial phase angle [45], which was later verified in experiments [35]. A similar integral technique was also used by Lee and Liu [46] with 5 modes interacting in a round jet. This idea was later used to describe the development of a single mode in a round jet using results from Linear Stability Theory (LST) [47] and the Linearized Euler Equations (LEE) [23]. More recently, this theory has been applied to a supersonic shear layer for two harmonically related modes [48]. The conditions of this shear layer had the same conditions as the jet considered in the current work. This work found a most amplified Strouhal number corresponding to the peak noise in the jet column mode from [25]. Theory like this is significant research dealing with excitation because it can provide guidance for expensive computations and experiments in a relatively short period of time. The ROM has been extended into three dimensions using LEE [49, 50] and is used here to guide the setup of excitation, which is described with more detail in Chapter 2.

Of particular interest to the ROM are earlier studies on multifrequency excitation. The first example is the work of Arbey and Ffowcs-Williams [51] where a low-speed round jet was forced at harmonically related frequencies. By varying the initial phase between the forced modes, control over the process of harmonic generation was achieved. Both harmonic and subharmonic interaction was studied, and it was found that harmonics were easier to control. Later computations by Mankbadi [52] also showed a dependence on the initial phase angle of the excitation. This work also found that the excitation increased the turbulence in the jet; high frequencies increased turbulence close to the nozzle exit while lower frequencies increased the turbulence further downstream.

1.4 Controls for Jet Noise Reduction

There are a limited number of studies that have attempted to employ closed loop control for jet noise. Natarajan et al. [53] developed a closed loop controller based on global instability modes of a supersonic round jet. Depending on controller gain, they were able to show a reduction in the noise for a wide range of polar angles. More recently, Karban et al. [54] developed a closed-loop controller based on a linear Ginzburg-Landau model to

reduce installed jet noise and were successful depending on sensor placement. Maia et al. [55] examined a forced low Mach number turbulent round jet and developed a closed-loop control strategy utilizing wave cancellation. The controller successfully reduced velocity fluctuations by an order of magnitude and reductions persisted significantly downstream. Acoustic impacts were not reported in this publication, but is an example of a similar control strategy to the one used in the present study.

The control strategy in this work attempts to use cancelling waves that either reduce the initial disturbance value at the jet exit and reduce the maximum downstream amplification in the jet plume. Theoretical work has shown that lower initial disturbance amplitudes lead to lower disturbance peaks downstream [56]. The boundary layer at the nozzle exit has been shown to be important on the downstream dynamics of the jet and how it responds to excitation. Bogey and Bailly [57] show that lower inflow turbulence intensities resulted in a lower presence of high frequency noise, but higher presence of lower frequency noise because due to the development of the initially laminar shear layer. Speth and Gaitonde [58] examine the effects of boundary layer thickness and found that increasing boundary layer thickness reduces control authority from excitation.

1.5 Contribution of Research

The primary contribution of this work is the development and validation of a Reduced-Order Model (ROM) that can reasonably predict the interactions between harmonically-related noise sources in the jet. This ROM has successfully guided experiments in low-speed round jets [35, 45], and had some limited use on high-speed round jets [23], but without considering mode-mode interactions or followup high-fidelity studies. Prior efforts with this ROM are valuable because they provide insight to the flow physics utilizing lower-fidelity tools such as LST or LEE, which are much less demanding compared to LES or experiments. Contemporary interests in rectangular jets require re-derivation of the ROM using Cartesian coordinates, which is presented in Sec. 2.1. The process for evaluating the ROM using LEE is detailed in Sec. 3.1 and 3, which followed as a guide for future studies. The ROM work

only focuses on the case of a symmetric disturbance, but it is shown in Sec. 2.5 how more modes and higher-order modes can be incorporated.

A powerful implication of the ROM is that it can take some of the guesswork out of prescribing an unsteady excitation in high-fidelity studies. In this case, LES is utilized. An unexcited, baseline case is first considered to identify amplified near field coherent structures in the jet and evaluate their contribution to the far field noise. From here, a fundamental frequency is identified that needs reduced. Using the ROM, interactions between the fundamental and either its harmonic or subharmonic can be modelled. It can be evaluated whether fundamental-harmonic or fundamental-subharmonic interactions are more effective in reducing the fundamental, giving a forcing frequency to implement in LES. Other factors such as relative magnitudes between the fundamental and forcing frequency can also be evaluated with the ROM and whether or not there is an ideal initial phase lag between the fundamental and forcing frequency. Implementation in LES is presented in Chapter 6.

Though a bit of a side tangent from the ROM approach, this work also presents some use of controls for jet noise control. One of the approaches taken is that of a pure cancellation whereby sensors read in a disturbance upstream in the nozzle, and the actuators respond with the same signal, but 180° out of phase. Although this is not closed-loop control, it is a step beyond the current methodology of open-loop control. If successful, this will ideally generate more interest in controls for jet noise control. This is presented in 7.

2 Reduced-Order Model Formulation

To predict optimal excitation parameters and obtain insight into the flow physics, a Reduced-Order Model (ROM) is used. This ROM follows the same approach originally used for low-speed round jets [45, 46], which successfully provided guidance for excitation in experiment [35]. Similar ROM's were also used for the supersonic round jet [23, 47] and the compressible shear layer [48]. The derivation for the 3D rectangular jet is given in Malczewski et al. [49] with some preliminary results.

2.1 Formulation

A supersonic rectangular jet being issued from a converging-diverging nozzle is considered as shown in Fig. 2.1. The formulation starts with the Navier-Stokes equations where triple decomposition is applied to each flow component splitting each variable into a mean flow, large-scale coherent wave-like structure, and random turbulence. Equations of motion for the mean flow, large-scale structures, and background turbulence are derived. Corresponding energy equations are then derived. The energy equations are then integrated across the transverse cross sections (y, z), and shape assumptions are made, yielding a set of nonlinear ODEs. Similar derivations have been done in Malczewski et al. [59] for the 2D shear layer. The detailed derivation for the 3D rectangular jet has previously been given in refs. [49, 50].

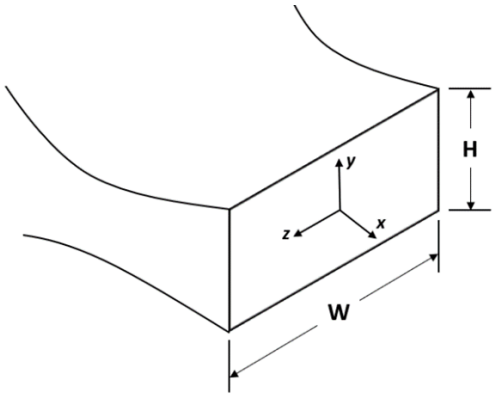

Figure 2.1 Jet Schematic.

2.1.1 Equations of Motion

The equations of motion start with the nondimensional continuity and momentum equations in Cartesian coordinates. Lengths are nondimensionalized by the height of the jet, density by the ambient density, and velocities by the jet exit velocity. Compressibility effects of the viscous terms are neglected.

$$\rho_t + (\rho u)_x + (\rho v)_y + (\rho w)_z = 0 \tag{2.1}$$

$$(\rho u)_t + \left(\rho u^2 + p\right)_x + (\rho uv)_y + (\rho uw)_z = \frac{1}{Re}\nabla^2 u \tag{2.2}$$

$$(\rho v)_t + (\rho vu)_x + \left(\rho v^2 + p\right)_y + (\rho vw)_z = \frac{1}{Re}\nabla^2 v \tag{2.3}$$

$$(\rho w)_t + (\rho wu)_x + (\rho wv)_y + \left(\rho w^2 + p\right)_z = \frac{1}{Re}\nabla^2 w \tag{2.4}$$

Reynolds number and Laplacian operator are defined as:

$$Re = \frac{\rho_{jet} U_{jet} H}{\mu}; \quad \nabla^2 = \frac{\partial^2}{\partial x^2} + \frac{\partial^2}{\partial y^2} + \frac{\partial^2}{\partial z^2} \tag{2.5}$$

Above, ρ_{jet} and U_{jet} are the jet exit density and velocity, respectively, and H is the height of the jet as depicted in Fig. 2.1. In addition to Reynolds number, Strouhal number is defined, also using the height of the jet, $St_H = fH/U_{jet}$. Next, triple decomposition is applied to the flow components.

$$g_i(x,y,z,t) = \bar{G}_i(x,y,z) + g_i'(x,y,z,t) + g_i''(x,y,z,t) \tag{2.6}$$

Above, flow components are split into mean flow ($\bar{}$), large-scale structure ($'$), and fine-scale random turbulence ($''$). The coherent mode is modelled as in Mankbadi [52] by a wave-packet of various frequencies and spanwise wave numbers interacting with each other,

as well as with the mean flow and turbulence.

$$g'(x,y,z,t) = \sum_{m,n} g'_{mn}(x,y,z)\exp(-i\omega_m t + inz) + CC \tag{2.7}$$

Here, CC denotes the complex conjugate. Phase averaging is denoted by $\langle \quad \rangle$ with respect to a particular mode (mn). This can separate each mode from the wave packet.

$$\left\langle \sum_{m,n} g'_{mn}(x,y,z)\exp(-i\omega_m t + inz) \right\rangle = g'_{mn}(x,y,z)\exp(-i\omega_m t + inz) \tag{2.8}$$

The triple decomposition is then substituted into Eqs. 2.1-2.4 for all flow components. For compactness, the following are additionally defined:

$$\widetilde{u}_i = \bar{\rho}u'_i + \rho'\bar{U}_i; \quad \widetilde{u}''_i = \bar{\rho}u''_i + \rho''\bar{U}_i; \quad \widetilde{u}_a = \widetilde{u}_i + \widetilde{u}''_i \tag{2.9}$$

Using these relations yield:

$$(\bar{\rho} + \rho' + \rho'')_t + \left(\overline{\rho U} + \widetilde{u}_a\right)_x + \left(\overline{\rho V} + \widetilde{v}_a\right)_y + \left(\overline{\rho W} + \widetilde{w}_a\right)_z = 0 \tag{2.10}$$

$$\begin{bmatrix} \left(\overline{\rho U} + \widetilde{u}_a\right)_t + \left[\bar{P} + p' + p'' + \left(\bar{U} + u' + u''\right)\left(\overline{\rho U} + \widetilde{u}_a\right)\right]_x \\ + \left[\left(\bar{V} + v' + v''\right)\left(\overline{\rho U} + \widetilde{u}_a\right)\right]_y \\ + \left[\left(\bar{W} + w' + w''\right)\left(\overline{\rho U} + \widetilde{u}_a\right)\right]_z \end{bmatrix} = \frac{1}{Re}\nabla^2\left(\bar{U} + u' + u''\right) \tag{2.11}$$

$$\begin{bmatrix} \left(\overline{\rho V} + \widetilde{v}_a\right)_t + \left[\left(\bar{U} + u' + u''\right)\left(\overline{\rho V} + \widetilde{v}_a\right)\right]_x \\ + \left[\bar{P} + p' + p'' + \left(\bar{V} + v' + v''\right)\left(\overline{\rho V} + \widetilde{v}_a\right)\right]_y \\ + \left[\left(\bar{W} + w' + w''\right)\left(\overline{\rho V} + \widetilde{v}_a\right)\right]_z \end{bmatrix} = \frac{1}{Re}\nabla^2\left(\bar{V} + v' + v''\right) \tag{2.12}$$

$$\begin{bmatrix} \left(\overline{\rho W} + \widetilde{w}_a\right)_t + \left[\left(\bar{U} + u' + u''\right)\left(\overline{\rho W} + \widetilde{w}_a\right)\right]_x \\ + \left[\left(\bar{V} + v' + v''\right)\left(\overline{\rho W} + \widetilde{w}_a\right)\right]_y \\ + \left[\bar{P} + p' + p'' + \left(\bar{W} + w' + w''\right)\left(\overline{\rho W} + \widetilde{w}_a\right)\right]_y \end{bmatrix} = \frac{1}{Re}\nabla^2\left(\bar{W} + w' + w''\right) \tag{2.13}$$

2.1.2 Mean Flow Kinetic Energy Equation

To obtain the mean flow kinetic energy equation, Eqs. 2.10-2.13 are first time averaged. The resultant momentum equations are then multiplied by their respective mean flow velocity component. Those resultant momentum equations are then added together. Mean flow kinetic energy is defined as $K = \frac{1}{2}\left(\bar{U}^2 + \bar{V}^2 + \bar{W}^2\right)$, giving:

$$\begin{bmatrix} \frac{\partial}{\partial x_j}\left(\bar{\rho}\bar{U}_j K\right) \\ +\frac{\partial}{\partial x_j}\left[\overline{(u_i' + u_i'')\widetilde{u}_{ja}}\bar{U}_i + \bar{U}_j\bar{P}\right] \end{bmatrix} = \begin{bmatrix} \bar{P}\frac{\partial U_j}{\partial x_j} + \left(\overline{u_i'\widetilde{u}_j + u_i''\widetilde{u}_j''}\right)\frac{\partial \bar{U}_i}{\partial x_j} \\ +\frac{1}{Re}\left[\nabla^2 K - \left(\frac{\partial \bar{U}_i}{\partial x_j}\right)^2\right] \end{bmatrix} \tag{2.14}$$

It is noted that the coherent perturbation in the above equation includes that of the entire coherent modes.

2.1.3 Large-Scale Kinetic Energy Equations

The continuity and momentum equations for the large-scale structures are obtained by first phase-averaging the full momentum equations for a given frequency, m, and a given spanwise number, n. The notation, "m" refers to the frequency components f, f/2, or 2f. The mean flow equations are then subtracted from the corresponding phase-averaged ones. The resulting equation contains the entire spanwise modes of that frequency. Higher order terms are neglected, as well as the $(u_i'\widetilde{u}_j - \overline{u_i'\widetilde{u}_j})$ terms. The governing momentum equations for an (mn) large-scale structures component become:

$$\widetilde{\rho}_t + \widetilde{u}_x + \widetilde{v}_y + \widetilde{w}_z = 0 \tag{2.15}$$

$$\begin{bmatrix} \widetilde{u}_t + \left(p' + \bar{\rho}\bar{U}u' + \widetilde{u}\bar{U}\right)_x + \left(\bar{\rho}\bar{U}v' + \widetilde{u}\bar{V}\right)_y \\ +\left(\bar{\rho}\bar{U}w' + \widetilde{u}\bar{W}\right)_z + \frac{\partial}{\partial x_j}\left[\left\langle u_j''\widetilde{u}''\right\rangle - \overline{u_j''\widetilde{u}''}\right] \end{bmatrix} = \frac{1}{Re}\nabla^2 u' \tag{2.16}$$

$$\begin{bmatrix} \widetilde{v}_t + \left(\bar{\rho}\bar{V}u' + \widetilde{v}\bar{U}\right)_x + \left(p' + \bar{\rho}\bar{V}v' + \widetilde{v}\bar{V}\right)_y \\ +\left(\bar{\rho}\bar{V}w' + \widetilde{v}\bar{W}\right)_z + \frac{\partial}{\partial x_j}\left[\left\langle u_j''\widetilde{v}''\right\rangle - \overline{u_j''\widetilde{v}''}\right] \end{bmatrix} = \frac{1}{Re}\nabla^2 v' \tag{2.17}$$

$$\begin{bmatrix} \widetilde{w}_t + \left(\bar{\rho}\bar{W}u' + \widetilde{w}\bar{U}\right)_x + \left(\bar{\rho}\bar{W}v' + \widetilde{w}\bar{V}\right)_y \\ + \left(p' + \bar{\rho}\bar{W}w' + \widetilde{w}\bar{W}\right)_z + \frac{\partial}{\partial x_j}\left[\left\langle u_j''\widetilde{w}''\right\rangle - \overline{u_j''\widetilde{w}''}\right] \end{bmatrix} = \frac{1}{Re}\nabla^2 w' \tag{2.18}$$

Similar to the mean flow, the resultant momentum equations are multiplied by their respective Large-Scale Structure (LSS) velocity component: u'_{mn}, v'_{mn}, and w'_{mn}. These equations are then summed and time-averaged. This results in the kinetic energy equation for the frequency, m, and spanwise wavenumber, n, of the fundamental or subharmonic component. The fundamental is defined as the most amplified frequency, which is further discussed in Section 3.2.1, with the subharmonic being the frequency half that of the fundamental. The kinetic energy of the LSS is defined as $Q = \frac{1}{2}\left(u'^2 + v'^2 + w'^2\right)$. The kinetic energy equations for an (mn) component become:

$$\begin{bmatrix} \frac{\partial\left(\bar{\rho}\bar{U}_j\bar{Q}_{mn}\right)}{\partial x_j} \\ + \frac{\partial}{\partial x_j}\left[\overline{\widetilde{u}_i\widetilde{r}_{ij}} + \overline{\widetilde{u}_j p'} + \overline{\widetilde{u}_i\left\langle u_i'\widetilde{u}_j\right\rangle}\right]_{mn} \end{bmatrix} = \begin{bmatrix} \frac{\left(\overline{u_j'\frac{\partial p'}{\partial x_j}}\right)_{mn} - \left(\overline{u_i'\widetilde{u}_j}\right)_{mn}\overline{\frac{\partial U_i}{\partial x_j}}}{+\left\langle u_i'\widetilde{u}_j\right\rangle_{mn}\left(\frac{\partial u_i'}{\partial x_j}\right)_{mn} + \left(\widetilde{r}_{ij}\frac{\partial u_i'}{\partial x_j}\right)_{mn}} \\ + \frac{1}{Re}\left[\nabla^2\bar{Q}_{mn} - \frac{\partial\left(\overline{u_{ij}'}_{mn}\right)^2}{\partial x_j}\right] \end{bmatrix} \tag{2.19}$$

where:

$$\widetilde{r}_{ij} = \left\langle u_i''\widetilde{u}_j''\right\rangle - \overline{u_i''\widetilde{u}_j''} \tag{2.20}$$

2.1.4 Small-Scale Turbulence Kinetic Energy Equation

To obtain the kinetic energy equation for the small-scale turbulence, the mean flow and LSS continuity and momentum equations are subtracted from the full ones given in Eqs. 2.10-2.13. The resultant momentum equations are then multiplied by their respective small-scale turbulence velocity, u'', v'', and w''. The resultant equations are then time-averaged and added together. Triple correlations with an odd number of random components are taken to be zero, while those with an even number of random components are non-zero. The

small-scale turbulence kinetic energy is defined as $q = \frac{1}{2}\left(\overline{u''^2} + \overline{v''^2} + \overline{w''^2}\right)$, which gives:

$$\frac{\partial\left(\bar{\rho}\bar{U}q\right)}{\partial x_j} + \frac{\partial}{\partial x_j}\left[\overline{\widetilde{r}_{ij}u_i'} + \overline{\widetilde{u}_j''(p''+q)} + \overline{\widetilde{u}_j q}\right] = \begin{bmatrix} \overline{-u_i''\widetilde{u}_j''}\frac{\partial \bar{U}}{\partial x_j} - \overline{\widetilde{r}_{ij}\frac{\partial u_i'}{\partial x_j}} \\ +\frac{1}{Re}\left[\overline{u_j''\nabla^2 u_j''}\right] \end{bmatrix} \tag{2.21}$$

2.2 Integral Form of the Energy Equation

From Eqs. 2.14 and 2.19, the integral equations are obtained. First, some assumptions will be made. The advection of the kinetic energy from each flow component by the mean flow is much greater than that of the perturbation quantities. Consequently, the second term on the LHS of the KE equations can be neglected relative to the first. The pressure-velocity correlation of the mean flow will be neglected, $\left(\overline{u'p_x'} + \overline{v'p_y'} + \overline{w'p_z'}\right)$. This term was kept in [47, 60], but was later shown in ref. [23] to be negligible. Mixing layer approximations are made such that $\bar{U}$ is greater than $\bar{V}$ and $\bar{W}$, and that $\frac{\partial(\bar{})}{\partial x} \ll \frac{\partial(\bar{})}{\partial y}, \frac{\partial(\bar{})}{\partial z}$ for all mean quantities. This approximation will not be applied to fluctuating quantities. The Reynolds stresses of the coherent structure component, $\left(\overline{u'\widetilde{v}}\right)$ and $\left(\overline{u'\widetilde{w}}\right)$, are much larger than the others. Computations by Salehian and Mankbadi [1] have shown this. With these assumptions, the equations are then integrated over the y and z directions.

$$\frac{d}{dx}\int_{-\infty}^{\infty}\int_{-\infty}^{\infty}\frac{1}{2}\bar{\rho}\bar{U}^3 dydz = \begin{bmatrix} \int_{-\infty}^{\infty}\int_{-\infty}^{\infty}\left[\left(\overline{-u'\widetilde{v}}\right)\bar{U}_y + \left(\overline{-u'\widetilde{w}}\right)\bar{U}_z\right]dydz \\ -\int_{-\infty}^{\infty}\int_{-\infty}^{\infty}(\overline{-u''\widetilde{v}''})\bar{U}_y dydz \\ -\frac{1}{Re}\int_{-\infty}^{\infty}\int_{-\infty}^{\infty}\left(\bar{U}_y^2 + \bar{U}_z^2\right)dydz \end{bmatrix} \tag{2.22}$$

The Reynolds stresses of the coherent structure here contain that of all (mn) frequencies and spanwise modes considered. The integrated equations for an (mn) mode and turbulence

then become:

$$\frac{d}{dx}\int_{-\infty}^{\infty}\int_{-\infty}^{\infty}\bar{\rho}\bar{U}\bar{Q}_{mn}dydz = \begin{bmatrix} \int_{-\infty}^{\infty}\int_{-\infty}^{\infty} -\left(\overline{v'\widetilde{u}}\bar{U}_y + \overline{w'\widetilde{u}}\bar{U}_z\right)dydz \\ -\int_{-\infty}^{\infty}\int_{-\infty}^{\infty}\left(\overline{\left\langle -u_j'\widetilde{u}_j\right\rangle\frac{\partial u_i'}{\partial x_j}}\right)_{mn}dydz \\ -\frac{1}{Re}\int_{-\infty}^{\infty}\int_{-\infty}^{\infty}\left(\nabla^2\bar{Q}_{mn} - \frac{\partial\left(\overline{u'_{ij,mn}}\right)^2}{\partial x_j}\right)dydz \end{bmatrix} \tag{2.23}$$

$$\frac{d}{dx}\int_{-\infty}^{\infty}\int_{-\infty}^{\infty}\bar{\rho}\bar{U}\bar{q}dydz = \begin{bmatrix} \int_{-\infty}^{\infty}\int_{-\infty}^{\infty}\left[(\overline{-u''\widetilde{v}''})\bar{U}_y + (\overline{-u''\widetilde{w}''})\bar{U}_z\right]dydz \\ +\int_{-\infty}^{\infty}\int_{-\infty}^{\infty}\Phi dydz - \frac{1}{Re}\int_{-\infty}^{\infty}\int_{-\infty}^{\infty}\left(\overline{-u_j''\nabla^2u_j''}\right)dydz \end{bmatrix} \tag{2.24}$$

where:

$$\Phi = \widetilde{r}_{ij}\frac{\partial u_i'}{\partial x_j} \tag{2.25}$$

It is noted that:

$$\overline{v'\widetilde{u}} = \overline{\rho u'v'} + \overline{\rho'v'U}; \quad \overline{u'\widetilde{v}} = \overline{\rho u'v'} + \overline{\rho'u'V} \tag{2.26}$$

In both of the above equations, Dahl and Mankbadi [47] kept the second term on the right-hand side, but it was later shown that this term is negligible relative to the first [23]. This term will be neglected here, and likewise for the other stress terms.

The stresses and strain appearing in the integral equations, in general, contain periodic terms in the z direction. By integrating over z and time-averaging, the explicit periodicity in z disappears from the time and z-averaged integral equations. Though it is noted that the wave components will include a spanwise wavenumber, n. Thus, it becomes consistent with the assumption that the mean flow is not periodic in the z direction in the average. Thus, these equations represent integrated cross-sectional energy as it evolves along the streamwise direction.

2.3 Physical Interpretations of the Integral Equations

The physical interpretation of the terms appearing in the energy equation is clear. For the mean flow, the energy equation can be written as:

$$\frac{d\theta}{dx}\frac{d}{dx}\int_{-\infty}^{\infty}\int_{-\infty}^{\infty}\frac{1}{2}\rho\bar{U}^3 dydz = -MW - MT \tag{2.27}$$

Above, θ is the momentum thickness and MW is the production of the coherent structures while the last term encompasses the dissipation by both viscous and turbulent effects. The equation states that the growth of the momentum thickness, or equivalently, the drain of the mean flow energy, is governed by the flow production of the coherent structure and the dissipation effects. The coherent mode equation can be written as:

$$\frac{\partial\left(\bar{\rho}\bar{U}_j\bar{Q}_{mn}\right)}{\partial x_j} = MW_{mn} + WW_{mn} - WT_{mn} \tag{2.28}$$

This states that the development of the wave energy is governed by the mean flow production of this particular wave component MW_{mn}, the second term WW_{mn} is its interaction with the other modes and the last term written as WT_{mn} are the combined viscous and turbulence dissipations.

2.4 Turbulence and Effective Reynolds Number

The goal here is to replicate a high Reynolds number turbulent rectangular jet. Mankbadi [45, 52] has shown how to properly account for turbulence where two-way turbulence-coherent structure interactions are considered. However, due to the complexity of the two-way turbulence interactions, a simpler approach is adopted. First, it is assumed that the effect of the coherent structure on the background random turbulence is negligible. However, the effect of the random turbulence on the coherent structure is considered. Thus, in the present analysis, an effective Reynolds number is used, replacing Re by Re_{eff}. Thus, instead of linking the turbulence explicitly in the integrated equation, it is absorbed into the effective

Reynolds number. The integrated equations for the rectangular jet reduce to:

$$\frac{d}{dx}\int_{-\infty}^{\infty}\int_{-\infty}^{\infty}\frac{1}{2}\rho\bar{U}^3 dydz = \begin{bmatrix} -\int_{-\infty}^{\infty}\int_{-\infty}^{\infty}\left[\left(\overline{-u'\widetilde{v}}\right)\bar{U}_y + \left(\overline{-u'\widetilde{w}}\right)\bar{U}_z\right]dydz \\ -\frac{1}{Re_{eff}}\int_{-\infty}^{\infty}\int_{-\infty}^{\infty}\left(\bar{U}_y^2+\bar{U}_z^2\right)dydz \end{bmatrix} \tag{2.29}$$

$$\frac{d}{dx}\int_{-\infty}^{\infty}\int_{-\infty}^{\infty}\bar{\rho}\bar{U}\bar{Q}_{mn}dydz = \begin{bmatrix} \int_{-\infty}^{\infty}\int_{-\infty}^{\infty}\left[\left(\overline{-u'_{mn}\widetilde{v}_{mn}}\right)\bar{U}_y + \left(\overline{-u'_{mn}\widetilde{w}_{mn}}\right)\bar{U}_z\right]dydz \\ -\int_{-\infty}^{\infty}\int_{-\infty}^{\infty}\left[\overline{\left\langle -u'_j\widetilde{u}_j\right\rangle\frac{\partial u'_i}{\partial x_j}}\right]_{mn}dydz \\ -\frac{1}{Re_{eff}}\int_{-\infty}^{\infty}\int_{-\infty}^{\infty}\left[\left(\overline{u'_{ix}}\right)^2+\left(\overline{u'_{iy}}\right)^2+\left(\overline{u'_{iz}}\right)^2\right]_{mn}dydz \end{bmatrix} \tag{2.30}$$

Using the form of the ODE given in Eqs. 2.29 and 2.30, the case of zero excitation is considered, thus only Eq. 2.29 is solved with only the viscous terms. Effective Reynolds number is then governed purely by the mean flow of the jet and can be simply solved for and is shown in Fig. 2.2.

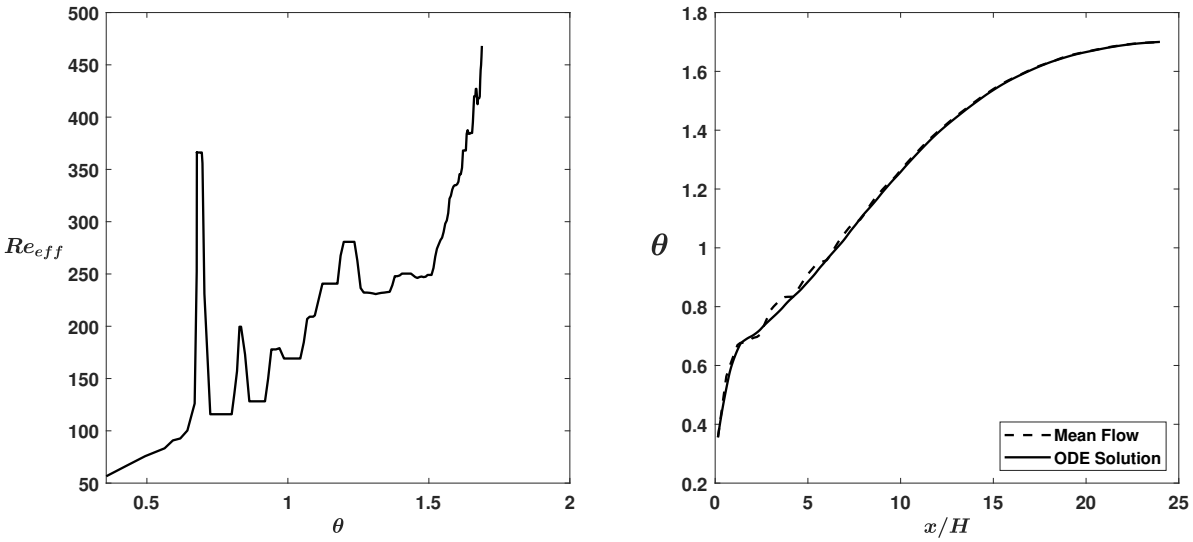

Figure 2.2 Effective Reynolds number (left) and corresponding ODE solution (right) for the momentum thickness compared with data [1].

2.5 Mode Decomposition

It is noted that in the above equations:

$$g'(x,y,z,t) = \sum_{m,n} g'_{mn}(x,y,z)\exp(-i\omega_m t + inz) + CC \tag{2.31}$$

So, for the mean flow, the stress term can be written as:

$$\left(\overline{-v'\widetilde{u}}\right) = \sum_{mn}(v'_{mn}\widetilde{u}^*_{mn}) + CC + \sum_{m,k,l;k\neq l} v'_{ml}\widetilde{u}^*_{mk}\exp(i(N_k - N_l)z) + CC \tag{2.32}$$

The first summation is independent of z. The second summation is dependent on z and can change the interaction in the z-direction. But its average over z is zero. They can redistribute the mean flow energy over z, but goes to zero when integrated over z. Thus, the mean flow production of the waves is given by the linear superposition of each frequency component stress:

$$MW = \sum_{m,n} MW_{mn} \tag{2.33}$$

Thus, the mean flow production is the sum of the production of each wave. Wave-wave interactions are now considered, which is formed from stress multiplied by strain.

$$\int_{-\infty}^{\infty}\int_{-\infty}^{\infty}\left(\overline{\langle -u'_i\widetilde{u}_j\rangle\frac{\partial u'}{\partial x_j}}\right)dydz \tag{2.34}$$

Because of the time averaging the interaction among three waves, m,k,l, is generally zero, unless:

$$\omega_k \pm \omega_l = \pm\omega_m \tag{2.35}$$

$$n_k \pm n_l = \pm n_m \tag{2.36}$$

For the case of only two frequency modes considered here, this will necessitate that their frequencies will be related to each other via the fundamental-harmonic relations. Thus, the analysis is limited to two frequency modes ($m = 1, 2$) and they are related to each other by

the harmonic relation:

$$\omega_2 = 2\omega_1 \tag{2.37}$$

For the z-periodic modes, the two cases of $(n = 0, 1)$ are considered. These can generate nonlinearly with other waves, but only those at the jet inlet are considered here. With this set of modes there are generally three classifications of the wave-wave interactions: Among purely z-periodic modes, between purely planar waves, and mixed planar-periodic interactions. For purely periodic modes, the integrated interactions over z are zero. And with the energy defined here as the integration over z, then these purely periodic modes produce zero averaged interaction and are of no interest here. This is an interesting result since it indicates that that unlike the planar waves, the first two asymmetric frequency components cannot generate other frequency components. This is also consistent with experimental observations in Cohen and Wygnanski [61, 62] that the helical modes themselves cannot destroy the axis symmetry of a round jet. For the case of two planar waves $mn = (1, 0) + (2, 0)$, their interactions and their energy equations can be written as:

$$\frac{d}{dx}\int_{-\infty}^{\infty}\int_{-\infty}^{\infty}\frac{1}{2}\rho\bar{U}^3 dydz = \begin{bmatrix} -\int_{-\infty}^{\infty}\int_{-\infty}^{\infty}\left[\left(\overline{-u'_{10}\widetilde{v}_{10}}\right)\bar{U}_y + \left(\overline{-u'_{10}\widetilde{w}_{10}}\right)\bar{U}_z\right]dydz \\ -\int_{-\infty}^{\infty}\int_{-\infty}^{\infty}\left[\left(\overline{-u'_{20}\widetilde{v}_{20}}\right)\bar{U}_y + \left(\overline{-u'_{20}\widetilde{w}_{20}}\right)\bar{U}_z\right]dydz \\ -\frac{1}{Re}\int_{-\infty}^{\infty}\int_{-\infty}^{\infty}\left[\left(\bar{U}_y\right)^2 + \left(\bar{U}_z\right)^2\right]dydz \end{bmatrix} \tag{2.38}$$

$$\frac{d}{dx}\int_{-\infty}^{\infty}\int_{-\infty}^{\infty}\bar{\rho}\bar{U}\bar{Q}_{10}\,dydz = \begin{bmatrix} \int_{-\infty}^{\infty}\left[\left(\overline{-u'_{10}\widetilde{v}_{10}}\right)\bar{U}_y + \left(\overline{-u'_{10}\widetilde{w}_{10}}\right)\bar{U}_z\right]dydz \\ -\int_{-\infty}^{\infty}\int_{-\infty}^{\infty}\left[\overline{\left\langle -u'_j\widetilde{u}_j\right\rangle_{10}\left(\frac{\partial u'_i}{\partial x_j}\right)_{20}}\right]dydz \\ -\frac{1}{Re_{\text{eff}}}\int_{-\infty}^{\infty}\int_{-\infty}^{\infty}\left[\left(\overline{u'_{ix}}\right)^2 + \left(\overline{u'_{iy}}\right)^2 + \left(\overline{u'_{iz}}\right)^2\right]_{10}dydz \end{bmatrix} \tag{2.39}$$

$$\frac{d}{dx}\int_{-\infty}^{\infty}\int_{-\infty}^{\infty}\bar{\rho}\bar{U}\bar{Q}_{20}\,dydz=\begin{bmatrix}\int_{-\infty}^{\infty}\left[\left(\overline{-u'_{20}\widetilde{v}_{20}}\right)\bar{U}_y+\left(\overline{-u'_{20}\widetilde{w}_{20}}\right)\bar{U}_z\right]dydz\\+\int_{-\infty}^{\infty}\int_{-\infty}^{\infty}\left[\overline{\left\langle -u'_j\widetilde{u}_j\right\rangle_{10}\left(\frac{\partial u'_i}{\partial x_j}\right)_{20}}\right]dydz\\-\frac{1}{Re_{\text{eff}}}\int_{-\infty}^{\infty}\int_{-\infty}^{\infty}\left[\left(\overline{u'_{ix}}\right)^2+\left(\overline{u'_{iy}}\right)^2+\left(\overline{u'_{iz}}\right)^2\right]_{20}dydz\end{bmatrix}\tag{2.40}$$

For the case of the mixed interactions among the planar and z-periodic wave: This can produce non-zero interactions after integrating and averaging over z if the conditions given above (Eqs. 2.38-2.40) are satisfied. The simplest examples are those of three modes with $(m,n)=(2,1)+(1,1)+(1,0)$. The equations can now be written as:

$$\frac{d}{dx}\int_{-\infty}^{\infty}\int_{-\infty}^{\infty}\frac{1}{2}\rho\bar{U}^3dydz=\begin{bmatrix}-\int_{-\infty}^{\infty}\int_{-\infty}^{\infty}(-u'_{10}\bar{\widetilde{v}}_{10})\bar{U}_y dydz-\int_{-\infty}^{\infty}\int_{-\infty}^{\infty}(-u'_{11}\bar{\widetilde{v}}_{11})\bar{U}_y dydz\\-\int_{-\infty}^{\infty}\int_{-\infty}^{\infty}(-u'_{21}\bar{\widetilde{v}}_{21})\bar{U}_y dydz-\int_{-\infty}^{\infty}\int_{-\infty}^{\infty}(-u'_{10}\bar{\widetilde{w}}_{10})\bar{U}_z dydz\\-\int_{-\infty}^{\infty}\int_{-\infty}^{\infty}(-u'_{11}\bar{\widetilde{w}}_{11})\bar{U}_z dydz-\int_{-\infty}^{\infty}\int_{-\infty}^{\infty}(-u'_{21}\bar{\widetilde{w}}_{21})\bar{U}_z dydz\\-\frac{1}{Re_{eff}}\int_{-\infty}^{\infty}\int_{-\infty}^{\infty}\left[\left(\bar{U}_y\right)^2+\left(\bar{U}_z\right)^2\right]dydz\end{bmatrix}\tag{2.41}$$

$$\frac{d}{dx}\int_{-\infty}^{\infty}\int_{-\infty}^{\infty}\bar{\rho}\bar{U}\bar{Q}_{10}dydz=\begin{bmatrix}\int_{-\infty}^{\infty}\int_{-\infty}^{\infty}\left[\left(\overline{-u'_{10}\widetilde{v}_{10}}\right)\bar{U}_y+\left(\overline{-u'_{10}\widetilde{w}_{10}}\right)\bar{U}_z\right]dydz\\+\int_{-\infty}^{\infty}\int_{-\infty}^{\infty}\left[\overline{\left\langle -u'_{j21}\widetilde{u}_{j11}\right\rangle\left(\frac{\partial u'_i}{\partial x_j}\right)_{10}}\right]dydz\\-\frac{1}{Re_{eff}}\int_{-\infty}^{\infty}\int_{-\infty}^{\infty}\left[\left(\overline{u'_{ix}}\right)^2+\left(\overline{u'_{iy}}\right)^2+\left(\overline{u'_{iz}}\right)^2\right]_{10}dydz\end{bmatrix}\tag{2.42}$$

$$\frac{d}{dx}\int_{-\infty}^{\infty}\int_{-\infty}^{\infty}\bar{\rho}\bar{U}\bar{Q}_{11}dydz=\begin{bmatrix}\int_{-\infty}^{\infty}\int_{-\infty}^{\infty}\left(\overline{-u'_{11}\widetilde{v}_{11}}\right)\bar{U}_y dydz\\+\int_{-\infty}^{\infty}\int_{-\infty}^{\infty}\left[\overline{\left\langle -u'_{j10}\widetilde{u}_{j11}\right\rangle\left(\frac{\partial u'_i}{\partial x_j}\right)_{21}}\right]dydz\\-\int_{-\infty}^{\infty}\int_{-\infty}^{\infty}\left[\overline{\left\langle -u'_{j21}\widetilde{u}_{j11}\right\rangle\left(\frac{\partial u'_i}{\partial x_j}\right)_{10}}\right]dydz\\-\frac{1}{Re_{eff}}\int_{-\infty}^{\infty}\int_{-\infty}^{\infty}\left[\left(\overline{u'_{ix}}\right)^2+\left(\overline{u'_{iy}}\right)^2+\left(\overline{u'_{iz}}\right)^2\right]_{11}dydz\end{bmatrix}\tag{2.43}$$

$$\frac{d}{dx}\int_{-\infty}^{\infty}\int_{-\infty}^{\infty}\bar{\rho}\bar{U}\bar{Q}_{21}dydz = \begin{bmatrix} \int_{-\infty}^{\infty}\int_{-\infty}^{\infty}\left(\overline{-u'_{21}\widetilde{v}_{21}}\right)\bar{U}_y dydz \\ +\int_{-\infty}^{\infty}\int_{-\infty}^{\infty}\left(\overline{-u'_{21}\widetilde{w}_{21}}\right)\bar{U}_z dydz \\ +\int_{-\infty}^{\infty}\int_{-\infty}^{\infty}\left[\overline{\left\langle -u'_{j10}\widetilde{u}_{j11}\right\rangle\left(\frac{\partial u'_i}{\partial x_j}\right)_{21}}\right]dydz \\ -\frac{1}{Re_{eff}}\int_{-\infty}^{\infty}\int_{-\infty}^{\infty}\left[\left(\overline{u'_{ix}}\right)^2+\left(\overline{u'_{iy}}\right)^2+\left(\overline{u'_{iz}}\right)^2\right]_{21}dydz \end{bmatrix} \tag{2.44}$$

Again, the Reynolds number appearing in the above equations is the effective Reynolds number including the turbulence effects. The mean flow is affected by the coherent structure since the equation for the momentum thickness includes the energy absorbed by the coherent structure from the mean flow on the right-hand side.

2.6 Shape Assumptions

Shape assumptions regarding the transverse and spanwise components of the disturbance are made to solve the integral ODE's system. The coherent structure is assumed to be in the form of travelling waves. Its streamwise development is obtained from the nonlinear interactions with the mean flow, turbulence as well as the mode-mode interaction. Its transverse profile, however, is obtained from the LEE solution normalized such that it is taken as the profile to be used to integrate the integral equations along y and z.

$$\begin{pmatrix} u'_i(x,y,z,t) \\ p'(x,y,z,t) \\ \rho'(x,y,z,t) \end{pmatrix} = A(x)e^{i\psi(x)}\begin{pmatrix} \hat{u}_i(y,z) \\ \hat{p}(y,z) \\ \hat{\rho}(y,z) \end{pmatrix} e^{-i\omega t+inz} \tag{2.45}$$

The shape functions, denoted by $\widehat{(\ )}$, and axial phase function, $\psi(x)$, are to be determined from LEE and are both functions of the streamwise location, x, and frequency, ω. Thus, these are both assumed to be linear. The nonlinear amplitude, $A(x)$, is evaluated by solving nonlinear ODEs and described in detail later. To remove the effects of linear amplification

from LEE, the shape functions are normalized at each streamwise location such that:

$$\int_{-\infty}^{\infty}\int_{-\infty}^{\infty}\left(|\hat{u}|^2+|\hat{v}|^2+|\hat{w}|^2\right)dydz=1 \tag{2.46}$$

When considering more than a single wave, then there could be phase lag between the interacting waves. In this case, the initial phase lag, $\beta_0=\psi(0)$. Here, β_0 is the initial phase difference between the two modes. Thus,

$$g_f'(x,y,z,t)=A(x)\,e^{i\psi_f(x)}\hat{g}_f(y,z)\exp\left[-i\omega_f t+inz+i\beta_0\right]+CC \tag{2.47}$$

$$g_s'(x,y,z,t)=B(x)\,e^{i\psi_s(x)}\hat{g}_s(y,z)\exp\left[-i\omega_s t+inz\right]+CC \tag{2.48}$$

It is noted that the β_0 in the term for the fundamental denotes an initial phase difference between the two modes, which can be 0, $\pi/2$, π, or $3\pi/2$.

As previously indicated, the mean flow is characterized by the momentum thickness, θ, rather than a physical distance, x, therefore making the integral terms in the ODE's functions of momentum thickness. With this shape assumption, the system of ODE's describing the mean flow and 2 nonlinear amplitudes, $(mn)=(1,0)+(2,0)$, become:

$$\frac{d\theta}{dx}\frac{dI_{am}}{d\theta}=-E_{10}I_{mw10}-E_{20}I_{mw20}-\frac{1}{Re_{eff}}I_{md} \tag{2.49}$$

$$\frac{d\left(I_{aw10}E_{10}\right)}{dx}=E_{10}\left(I_{mw10}-\frac{1}{Re_{eff}}I_{wd10}\right)-I_{ww10}E_{10}\sqrt{E_{20}} \tag{2.50}$$

$$\frac{d\left(I_{aw20}E_{20}\right)}{dx}=E_{20}\left(I_{mw20}-\frac{1}{Re_{eff}}I_{wd20}\right)+I_{ww10}E_{10}\sqrt{E_{20}} \tag{2.51}$$

where:

$$|A|^2=E_{20};\quad |B|^2=E_{10} \tag{2.52}$$

Above, there is an equation describing the mean flow (Eq. 2.49) and two equations describing nonlinear amplitudes for a fundamental and subharmonic mode (Eqs. 2.50 &

2.51). The Reynolds number here is an effective Reynolds number as described in Section 2.4, making it also a function of momentum thickness. The integral terms are defined below.

$$I_{am} = \int_{-\infty}^{\infty}\int_{-\infty}^{\infty} \frac{1}{2}\bar{\rho}\bar{U}^3 dydz \tag{2.53}$$

$$I_{md} = \int_{-\infty}^{\infty}\int_{-\infty}^{\infty} \left(\bar{U}_y^2 + \bar{U}_z^2\right) dydz \tag{2.54}$$

$$I_{aw} = \int_{-\infty}^{\infty}\int_{-\infty}^{\infty} \frac{1}{2}\bar{\rho}\bar{U}\left(|\hat{u}|^2 + |\hat{v}|^2 + |\hat{w}|^2\right)_{mn} dydz \tag{2.55}$$

$$I_{mw} = -\int_{-\infty}^{\infty}\int_{-\infty}^{\infty} \bar{\rho}\left[\left(\hat{v}\hat{u}^* + CC\right)\frac{\partial \bar{U}}{\partial y} + \left(\hat{w}\hat{u}^* + CC\right)\frac{\partial \bar{U}}{\partial z}\right]_{mn} dydz \tag{2.56}$$

$$I_{wd} = \begin{bmatrix} \int_{-\infty}^{\infty}\int_{-\infty}^{\infty} 2\left[\left(\alpha^2 + n^2\right)\left(|\hat{u}|^2 + |\hat{v}|^2 + |\hat{w}|^2\right)\right. \\ \left. + \left(\left|\frac{\partial \hat{u}}{\partial y}\right|^2 + \left|\frac{\partial \hat{v}}{\partial y}\right|^2 + \left|\frac{\partial \hat{w}}{\partial y}\right|^2\right) \right. \\ \left. + \left(\left|\frac{\partial \hat{u}}{\partial z}\right|^2 + \left|\frac{\partial \hat{v}}{\partial z}\right|^2 + \left|\frac{\partial \hat{w}}{\partial z}\right|^2\right)\right]_{mn} dydz \end{bmatrix} \tag{2.57}$$

where:

$$\alpha = \frac{d\psi}{dx} \tag{2.58}$$

which is obtained from the LEE solution. The integral term, I_{ww}, represents the interaction between the fundamental and subharmonic modes. It takes the following form:

$$I_{ww} = -\left\{\left(e^{i\beta_0 + i\epsilon}\right) I_{fs} + CC\right\} \tag{2.59}$$

where $\varepsilon = \psi_{20} - 2\psi_{10}$ and:

$$I_{fs} = \begin{bmatrix} \int_{-\infty}^{\infty}\int_{-\infty}^{\infty}\left[\left(\hat{u}^*\hat{v}^*\right)_{10}\frac{\partial \hat{u}_{20}}{\partial y} + \left(\hat{u}^*\hat{w}^*\right)_{10}\frac{\partial \hat{u}_{20}}{\partial z} + \left(\hat{v}^*\hat{v}^*\right)_{10}\frac{\partial \hat{v}_{20}}{\partial y}\right. \\ \left. + \left(\hat{v}^*\hat{w}^*\right)_{10}\left(\frac{\partial \hat{v}_{20}}{\partial z} + \frac{\partial \hat{w}_{20}}{\partial y}\right) + \left(\hat{w}^*\hat{w}^*\right)_{10}\frac{\partial \hat{w}_{20}}{\partial z}\right] dydz \end{bmatrix} \tag{2.60}$$

The integral term, I_{fs} is a complex quantity, where both real and imaginary components are important. In the case that $\psi_{f\approx}2\psi_s$, $\epsilon \approx 0$ and can be neglected. When considering

more than a single wave, then there could be phase lag between the interacting waves. In this case, the initial phase lag, $\beta_0 = \psi(0)$. Here, β_0 is the initial phase difference between the two modes. The β_0 term for the fundamental denotes an initial phase difference between the two modes, which can be 0, $\pi/2$, π, or $3\pi/2$. The interaction integral becomes:

$$I_{ww} = -2\,|I_{fs}|\,cos[\phi_{fs} + \beta_0] \tag{2.61}$$

3 Evaluation of the Reduced-Order Model

The ROM is now evaluated. The shape functions in Eqs. 2.53-2.60 are first obtained using LEE, which is described in Sec. 3.1. Single mode solutions are first considered in Sec. 3.2.1 in order to determine the fundamental frequency. Mode-Mode interactions are then considered in Sec. 3.2.2 between the fundamental and either its subharmonic or harmonic. Insights to the physics of the mode-mode interaction mechanism are presented in Sec. 3.3 and closing remarks in Sec. 3.4.

3.1 Use of the Linearized Euler Equations

To obtain the shape functions mentioned in Section 2.6, the Linearized Euler Equations (LEE) are used, which was also done in Dahl et al. [23] for a round jet. In LEE, a disturbance can be propagated through a mean flow profile. The jet considered in refs. [29, 33, 63] is used, for which a schematic is provided in Fig. 3.1. The jet is a Mach 1.5 heated rectangular jet with a 2:1 aspect ratio and a temperature ratio of $T_0/T_\infty = 3$. The jet is also perfectly expanded, but due to the geometry of the nozzle, shocks are still present.

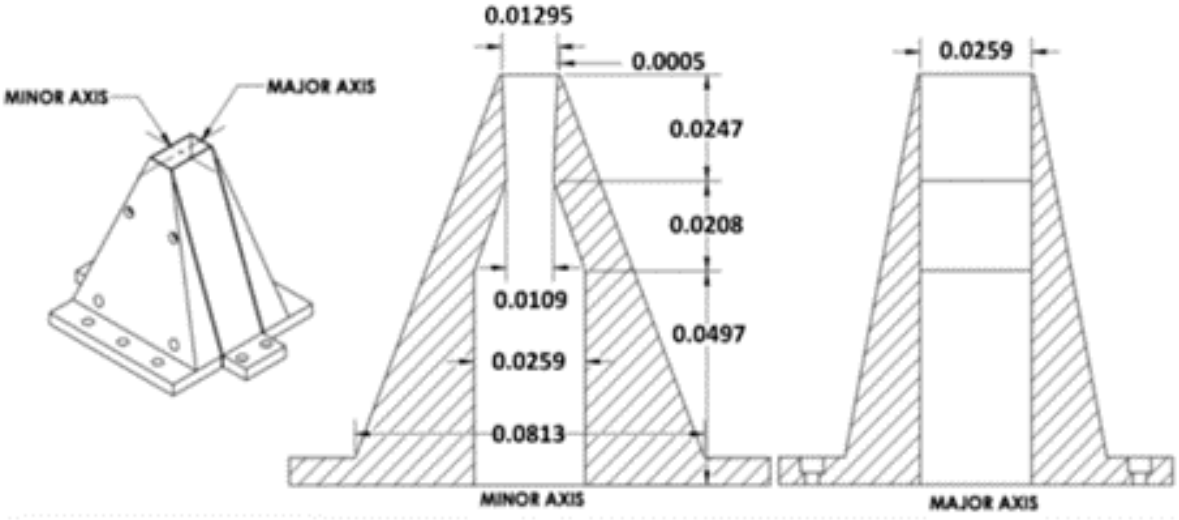

Figure 3.1 Rectangular jet schematic from [2].

The mean flow of the jet used in this work is the Reynolds-Averaged Navier-Stokes (RANS) data from Salehian and Mankbadi [64]. To reiterate nondimensional parameters,

lengths are nondimensionalized by the height of the jet, 0.01295 m, velocities by the jet exit velocity, 750 m/s, and densities by the ambient density, 1.15 kg/m^3.

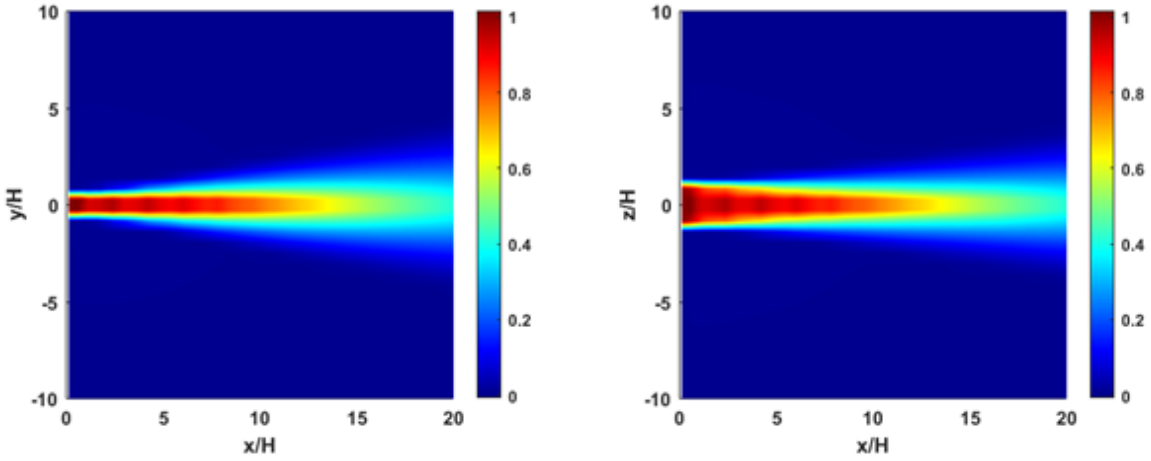

Figure 3.2 Nondimensionalized mean u-velocity in minor plane (left) and major plane (right).

LEE is performed using the OpenFOAM solver, "*leeFoam*", which is described in detail in ref. [20]. In summary, the governing equations for LEE are discretized using a 2nd order central differencing interpolation scheme in space. First order Euler discretization is used in time. For this case, an inflow disturbance is prescribed at the jet nozzle exit for a specified forcing frequency. The disturbance is placed in upper and lowermost cells within the jet exit plane and is uniform within the confines of the jet width. The disturbance is prescribed with a u-velocity of 10% nominal value of the jet exit velocity. Pressure and density disturbances are then prescribed using planar wave relations. Though simplified, this is closer to what was done in previous LEE studies for round jets, where the eigenfunctions from Linear Stability Theory were used [21, 23]. In the far field, an acoustic damping field is used starting at a radial distance $r/H = 55$, which is far beyond where data is collected. The damping field is frequency-dependent and comprehensively described in Salehian et al. [20]. OpenFOAM's "*acousticWaveTransmissive*" boundary condition is then used at the outflow boundaries. Additionally, a small artificial viscosity is also implemented for numerical stability. For the computational grid, a structured mesh was used and grid spacing was chosen such that a

minimum of 15 points per wavelength was achieved for each forced frequency. The cases were run with a physical time step of $10^{-6}s$. This resulted in approximately 1400 iterations per cycle. A pressure contour snapshot is shown in Fig. 3.3.

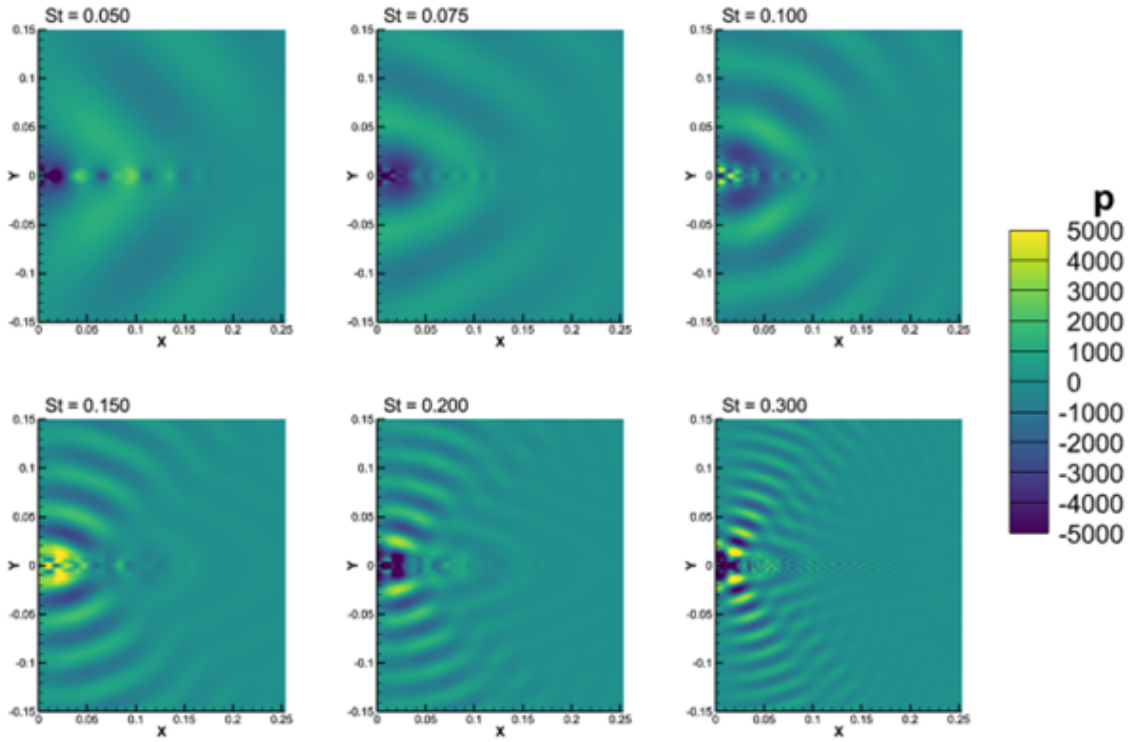

Figure 3.3 Instantaneous minor plane pressure contours from LEE.

To obtain the shape functions, the time history of the LEE solution was collected starting at a dimensional time of 0.005 seconds, and Fast Fourier Transform (FFT) was used. For each case, a total of 8000 samples were collected at a rate of 500 kHz. FFT was performed at every point within the 3D domain, but the solution was only outputted for the forced frequency. This was done for the components of velocity and for pressure. The results contain a real and imaginary component, both of which are periodic in x. In the shape assumption, transverse shape functions are multiplied by a periodic function in x, thus the shape functions themselves are not periodic. To rectify the periodicity in x, it is assumed that the streamwise phase function, $\psi(x)$, can be linearly obtained from the FFT result by taking the complex phase along the shear layer and multiplying by $e^{-i\psi(x)}$. The streamwise phase function is additionally used to compute the wavenumber using Eq. 2.58. Pressure

shape functions are displayed in Fig. 3.4.

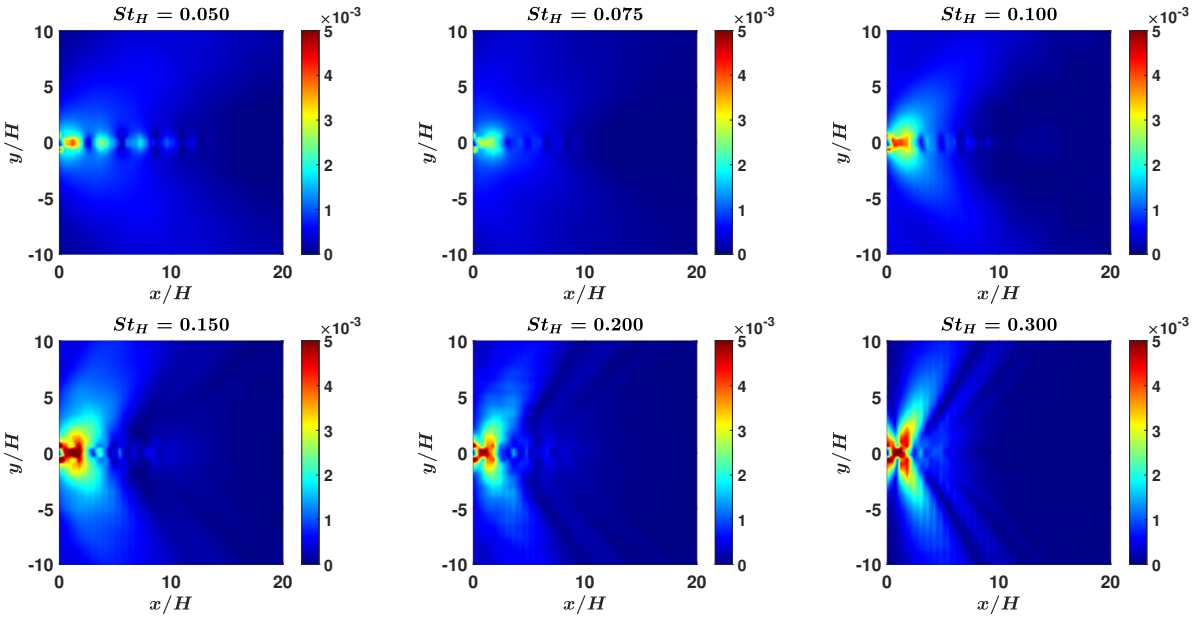

Figure 3.4 Pressure shape functions in minor plane at various St_H.

The integrals are now evaluated using Eqs. 2.53-2.57. We note that some are purely functions of the mean flow, while others are dependent on the shape functions. As done in the previous works [48, 49], the integrals are presented as a function of momentum thickness, rather than a physical coordinate. Thus, the integrals are unique for each Strouhal number and dependent on momentum thickness. Momentum thickness is defined in the minor plane at the jet centerline, making it a function of x. Effective Reynolds number is also a function of momentum thickness.

$$\theta\left(x\right) = \int_{-\infty}^{\infty} U\left(1-U\right) dy \tag{3.1}$$

The presented integral terms in Figs. 3.5 and 3.6 trend well with previous studies using a similar integral approach. The advection integral, I_{aw}, grows and decays which was also shown for a round jet [23, 47]. They also showed an increase in dissipation with momentum thickness, which is also shown here. The production integral, I_{mw}, grows, peaks, and decays. Higher frequency modes have a higher peak, but also have a sharper decay, which was

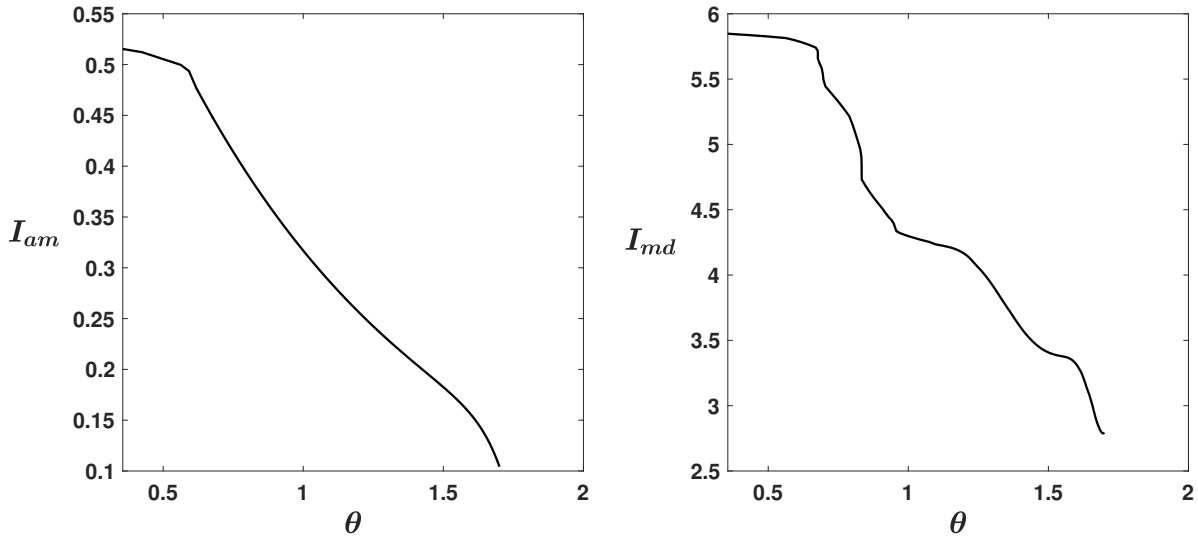

Figure 3.5 Mean flow integrals.

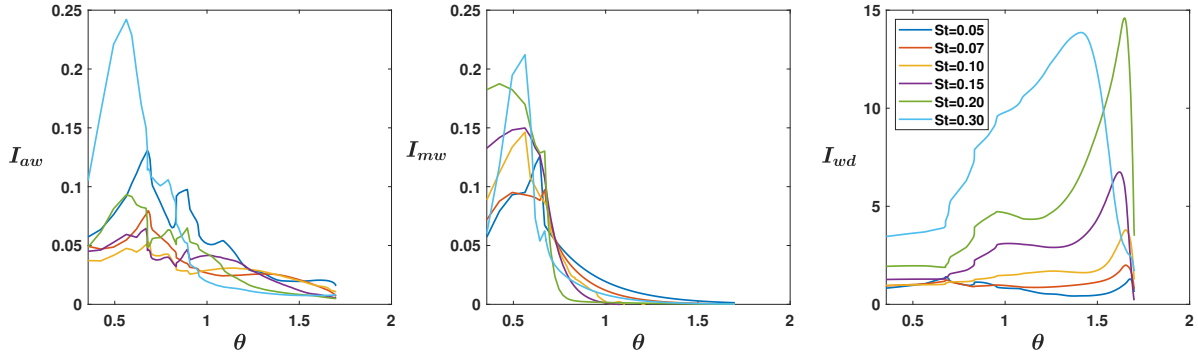

Figure 3.6 Shape function integrals.

previously seen in the compressible shear layer [48]. For each of the integral terms, there are some discontinuities that occur, most notably at $\theta = 0.70$. These correspond with and are attributed to the presence of shocks in the mean flow.

3.2 ROM Solution

The set of ODEs given in Eqs. 2.49-2.51 can now be solved. In this process, the shape functions obtained via linear methods are extended to the nonlinear regime via the integral equations. Interaction of a single mode with the mean flow is first considered; thus, only two equations (Eqs. 2.49 & 2.50) are being solved. From this, the different solutions are compared when the initial amplitudes are small, which is when amplification is maximized. This gives insight into what the most amplified Strouhal number is, which will be referred

to as the fundamental (f). The fundamental can then be modified by adding either its subharmonic (f/2) or harmonic (2f). As a practical consideration, initial amplitudes are kept small such that the performance of a physical propulsion device is minimally impacted, and it is also important that whatever is added does not get significantly amplified such that an additional noise source is not introduced.

3.2.1 Single-Mode Solutions

Single-mode ODE solutions are first considered, thus only the interaction of a mode with the mean flow is accounted for, and not any interactions with other modes. This is an initial value problem, where an initial momentum thickness is prescribed, which is obtained from the mean flow. An initial amplitude is also defined for the single mode. This is chosen to be small, ranging from $10^{-8} - 10^{-2}$.

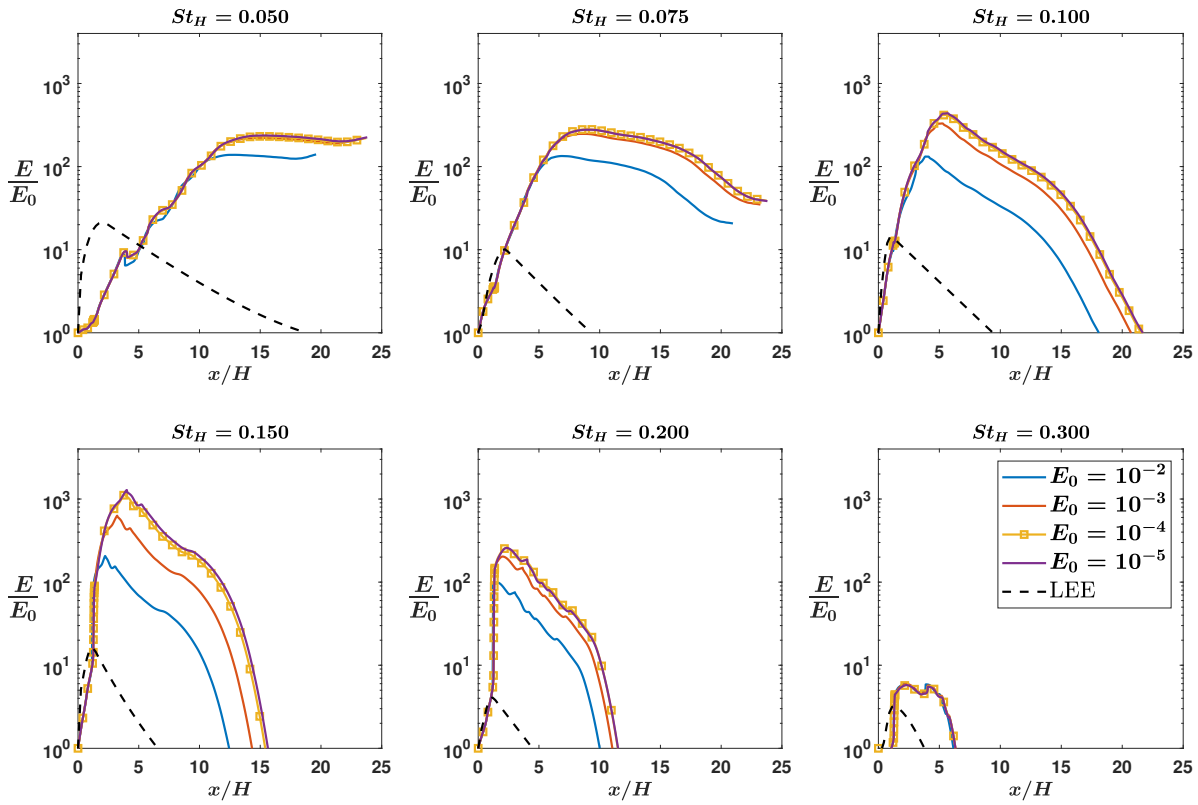

Figure 3.7 Single-Mode solutions for various Strouhal numbers.

Figure 3.7 shows the nonlinear amplitudes for the single-mode solutions with various initial amplitudes. A trend seen here that is consistent with the past work [35, 46, 48] is that

as the initial amplitude increases, the peak and lifespan are reduced. There is also a limit to how small an initial amplitude can be such that the amplification is maximized. In the above cases, this occurs when $E_0 = 10^{-4}$. The initial growth of the LEE solution compares well with the nonlinear solutions. However, at $x/H \approx 1.5$, each of the LEE amplitudes peak and decay. This streamwise location corresponds to the first shock in the mean flow, which LEE does not have treatment for. This kills the amplification in LEE, but the disturbances still propagate, and the effect of LEE amplification is removed via Eq. 2.46. The single-mode solutions compare very well with those from the compressible shear layer [48]. A direct comparison is made for Strouhal numbers 0.05, 0.10, and 0.20, and is shown in Fig. 3.8. Both sets of cases show similar levels of amplification, and the peaks occur at similar streamwise locations.

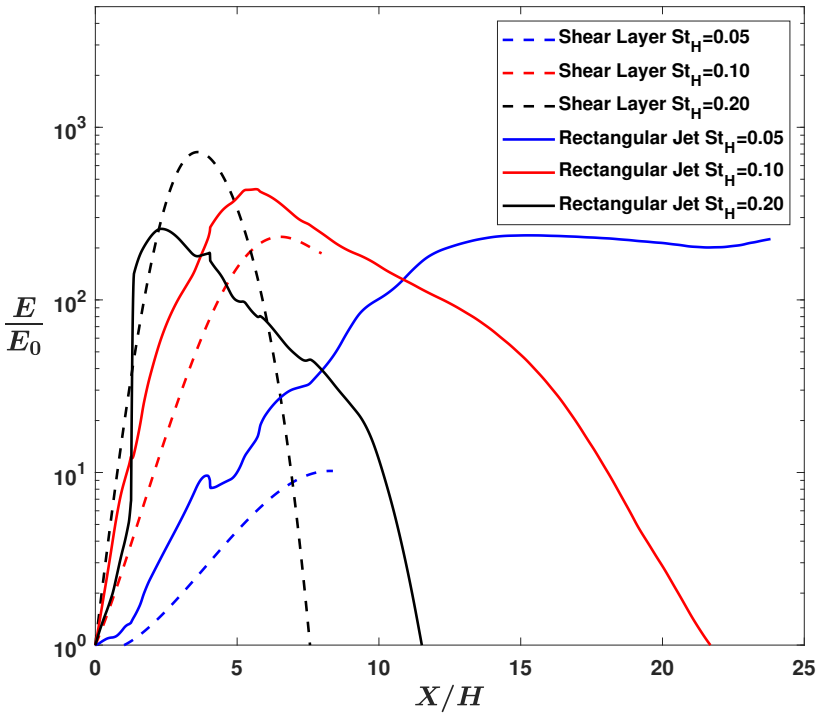

Figure 3.8 Comparison of single-mode solutions for the compressible shear layer [17] and rectangular jet with initial amplitude $E_0 = 10^{-5}$.

Figure 3.9 compares the single-mode nonlinear amplitudes. A trend seen here is that for higher Strouhal number, the peak comes sooner and also has a faster decay. This has previously been shown in the past works with the compressible shear layer [48, 59, 65]. In

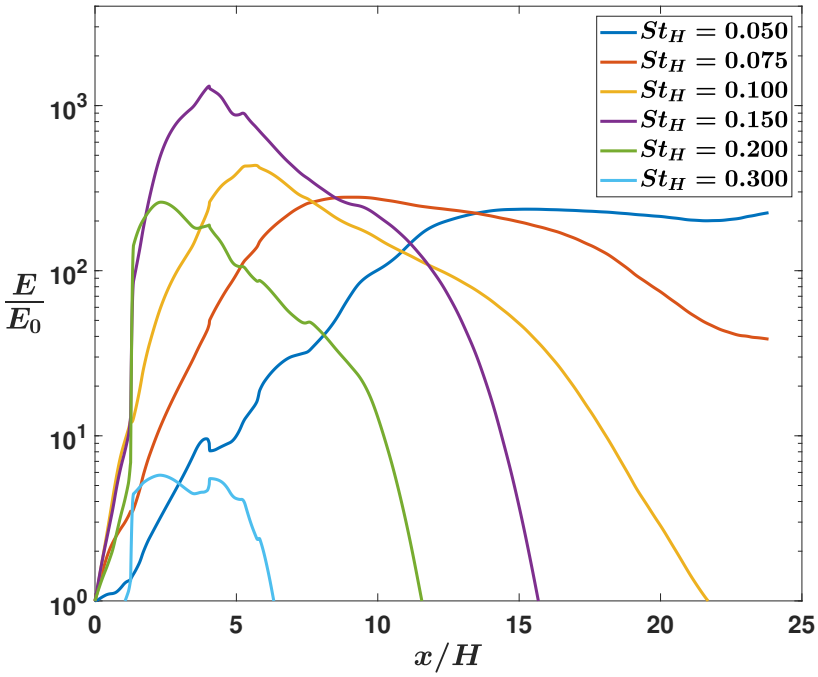

Figure 3.9 Comparison of all single-mode solutions for $E_0 = 10^{-8}$.

the present work, it is found that $St_H = 0.15$ is the most nonlinearly amplified. This differs slightly from the past work with the compressible shear layer, which found $St_H = 0.20$ to be the most amplified, though this Strouhal number is still shown to be significantly amplified. This result also agrees well with what other groups have found to be the peak broadband noise in higher fidelity studies of the same jet. Accounting for differences in length scale, these studies have generally found peak noise ranging around $St_H = 0.13$ [33, 63] to $St_H = 0.11$ [30]. From Fig. 3.9, $St_H = 0.15$ is the most amplified and needs reduced. In the subsequent section, this is addressed by adding either the subharmonic, $St_H = 0.075$, or harmonic, $St_H = 0.30$.

3.2.2 Bi-Modal Solutions

The case of interaction introduces a new integral term, I_{ww}, which governs the interaction between two harmonically related modes. The interaction term is strictly real, but dependent on the magnitude and phase of the complex integral, I_{fs}, which is shown in Fig. 3.10. The dominant terms in this integral are the strain of a higher frequency, multiplied by the stress of the lower frequency, similar to the definition of production by the mean flow. Like the

other integral terms, there is a sharp jump around $\theta = 0.70$, which corresponds to the first shock in the mean flow.

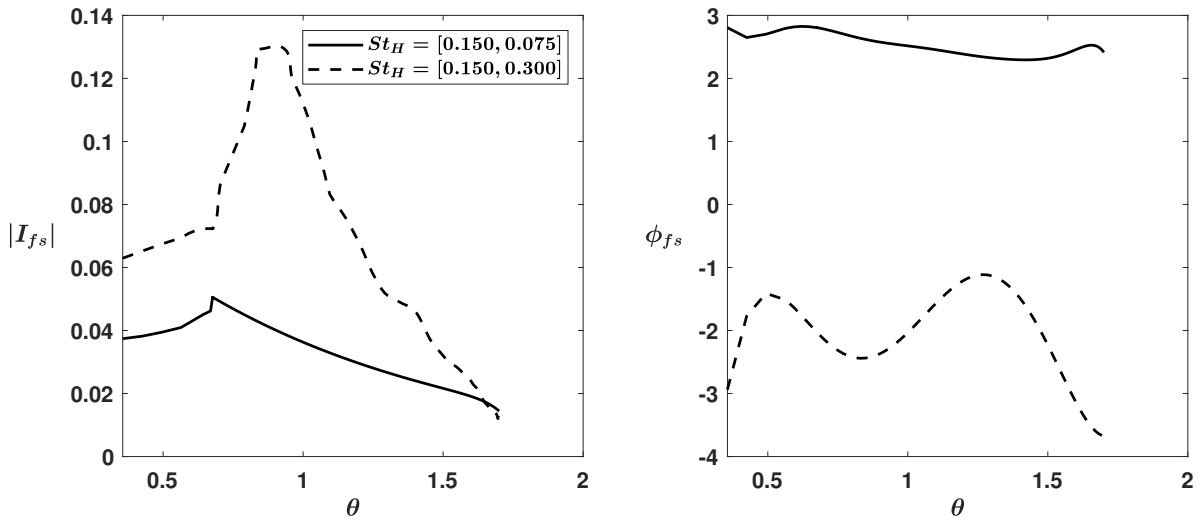

Figure 3.10 Magnitude (left) and phase (right) of interaction integral.

As in Section 3.2.1, this is an initial value problem. In addition to the initial momentum thickness and amplitudes of each mode, an initial phase angle between the two modes, β_0, is also defined which can take values of 0, $\pi/2$, π, or $3\pi/2$. In an experiment or computation, this initial phase cannot be easily controlled, and may in fact be changing with time if only a single frequency is being added via excitation. As is shown later, the direction and magnitude of energy transfer are highly dependent on this initial phase angle, thus the success criteria will also include the reduction of the fundamental at favorable phase angles and minimal amplification at unfavorable phase angles. Results at specified phase angles are considered upper and lower bounds for any amplification/reduction of individual modes, thus any actual reduction should lie somewhere in between.

The solutions for fundamental-subharmonic interactions are shown in Fig. 3.11. Adding the subharmonic has minimal success at reducing the peak of the fundamental. Some reduction was obtained for an initial phase angle of $\beta_0 = 0$. The effects of interaction are more evident for large initial amplitudes, which is consistent with past findings [48]. For initial phase angles of 0 and $\pi/2$, the lifespan of the fundamental was significantly shortened, but

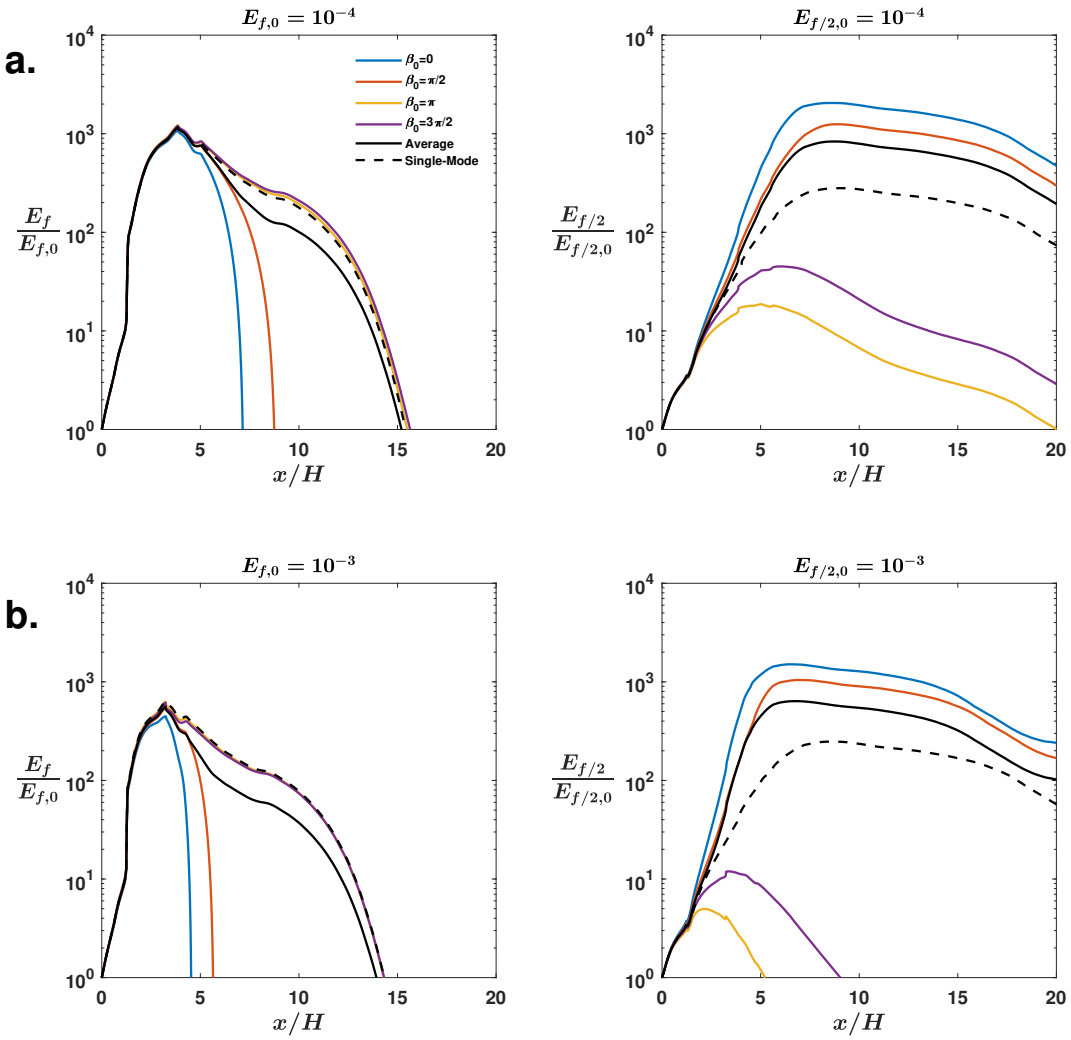

Figure 3.11 Interactions between Strouhal pair 0.15 (left) and 0.075 (right) for a) $E_{f,0} = E_{f/2,0} = 10^{-4}$ and b) $E_{f,0} = E_{f/2,0} = 10^{-3}$.

this phenomenon does not occur until after the fundamental peaks, thus it is difficult to definitively claim this mechanism can reduce the peak radiated noise. It is also shown that when the fundamental is reduced, the subharmonic is significantly amplified. Looking at the average, the subharmonic has significant amplification on the order of the fundamental's natural growth, which can mean the introduction of an additional noise source. This mechanism is ultimately not recommended for noise reduction.

The case of fundamental-harmonic interaction between Strouhal numbers 0.15 and 0.30 are now considered. Figure 3.12 clearly shows a reduction of the fundamental's peak for initial phase angles of π and $3\pi/2$. At the other unfavorable phase angles, there is minimal

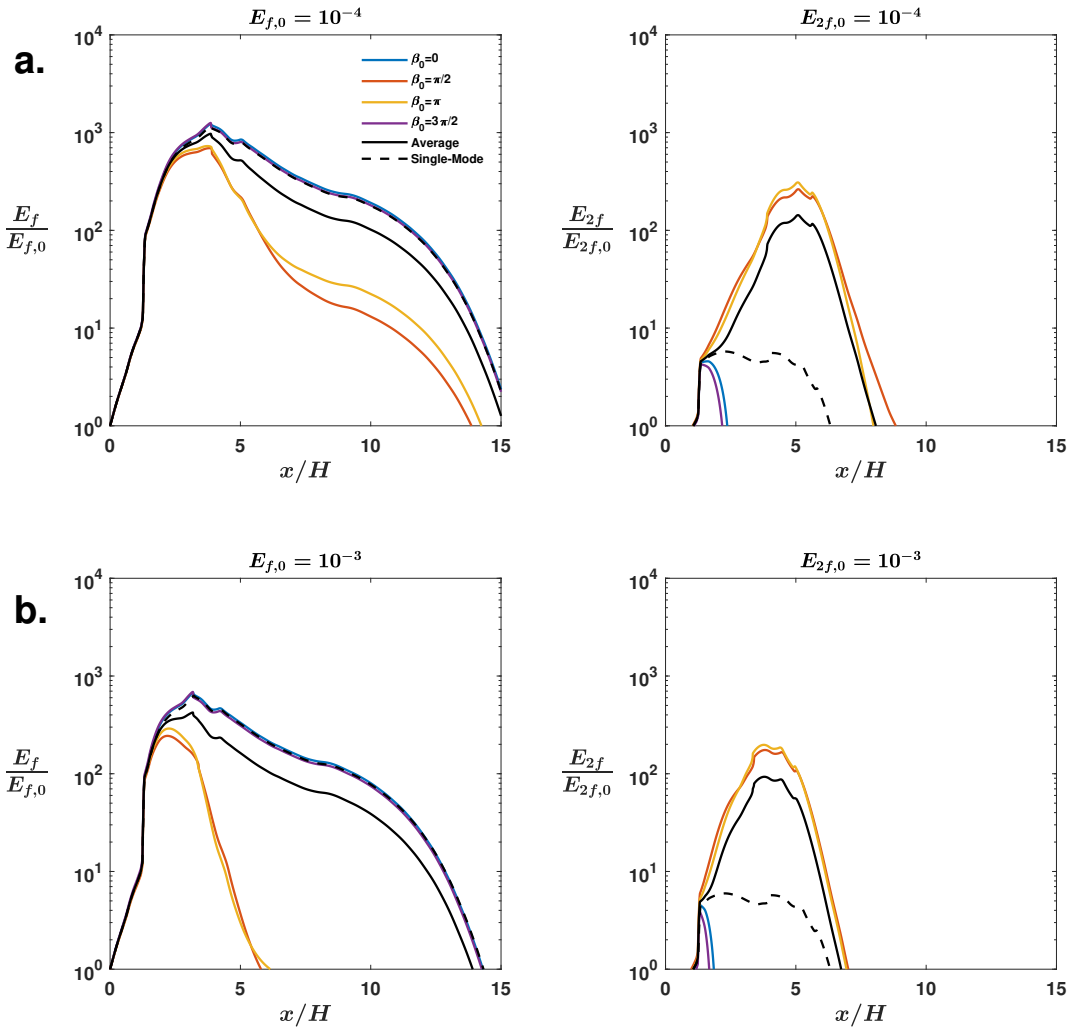

Figure 3.12 Interactions between Strouhal pair 0.15 (left) and 0.30 (right) for a) $E_{f,0} = E_{2f,0} = 10^{-4}$ and b) $E_{f,0} = E_{2f,0} = 10^{-3}$.

amplification of the fundamental. As expected, when the fundamental is reduced, the harmonic is amplified, and the reverse is true when the fundamental is amplified. Comparing these results to those of the subharmonic interactions, there is a more dramatic impact on the reduction or amplification of the harmonic. This is because of the large difference in the initial self-amplification between Strouhal numbers 0.15 and 0.30. The magnitude of interaction has contributions from both modes; thus, this behavior is expected. Considering the average between the different phase angles, there is an overall reduction of the peak of the fundamental and some reduction of its lifespan. Meanwhile, there is large amplification of the harmonic, but this peak amplitude remains well below that of the fundamental.

Ultimately, this can be recommended as a mechanism for noise reduction.

The harmonic is shown to be more effective at reducing the fundamental. This observation is consistent with similar reduced-order modelling on a compressible shear layer at the same operating conditions [48]. Experiments have also shown that exciting with moderate to high frequencies can reduce noise in the rectangular jet [30]. Samimy et al. [25] also found for twin rectangular jets that exciting at higher Strouhal numbers higher than the screech frequency can reduce the noise. Though the harmonic of the jet column mode is not into the screech range, it is an additional observation that adding higher frequencies can reduce the noise. Experiments in supersonic round jets with periodic blowing have shown exciting with twice the peak broadband frequency can reduce the peak, but also results in additive tones [43].

3.3 Discussion of Energy Exchange Mechanism

The nonlinear development of two harmonically related modes is presented mathematically in Eqs. 2.50 and 2.51. Physically, each mode grows and decays naturally due to the balance between the mean flow production and dissipation, regardless of if there is interaction from another frequency. The addition of a harmonic or subharmonic then acts as a modifier to the natural development of both modes. The reduction or amplification of either mode is determined by the natural development of the nonlinear amplitudes and initial phase angle between the two modes. Focusing now on both sets of interacting cases when initial amplitudes are 10^{-4}, these two aspects are further explored.

In both sets of results, there are unique solutions depending on the initial phase angle. Referring to the definition of this integral term in Eq. 2.61, the sign, and thus the direction of energy transfer is dependent on the net phase angle. This consists of the phase between the strain of a higher frequency and the stress of its subharmonic and is then shifted with the addition of an initial phase lag, β_0. Figure 3.13 shows the development of the interaction term for both fundamental-subharmonic and harmonic interactions. The way to interpret this is that positive values indicate a transfer of energy from a higher frequency to a lower one. Thus,

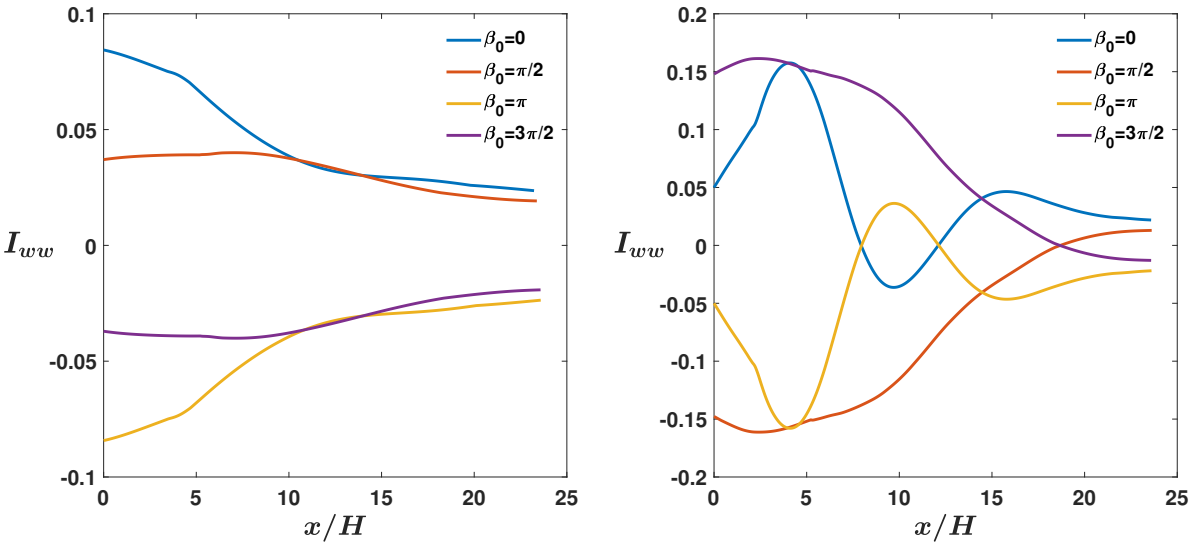

Figure 3.13 Comparison of energy transfer direction at various phase lags for fundamental-subharmonic (left) and fundamental-harmonic (right) interactions.

positive values indicate draining of the fundamental for fundamental-subharmonic interactions, while negative values indicate draining the fundamental for fundamental-harmonic interactions. Comparing the initial magnitudes in Fig. 3.13 to the maximum reduction and amplification in Figs. 3.11 and 3.12, it is shown that extrema on the initial values of I_{ww} result in the maximum reduction and amplifications in the ROM results. It is concluded that maximizing I_{ww} in the initial region of the jet will produce the most pronounced interaction, which was also concluded in Mankbadi et al. [48].

While looking at initial phase angle is helpful for predicting the magnitude of interaction, it gives little to no explanation as to why harmonic interactions are more effective at reducing the peak of the fundamental compared to subharmonic ones. To explain this, the role of natural amplification in the interaction process is analyzed. The interaction is dependent on the amplitude of both interacting modes, thus both modes need to be sufficiently amplified at the same streamwise location to maximize interaction. This is visualized in Fig. 3.14, which includes the magnitude of the interaction. It highlights that interaction occurs sooner for harmonic interactions. Figures 3.11 and 3.12, show the fundamental peaking at a streamwise location of x/H around 4. This location also coincides with where the interaction peaks for

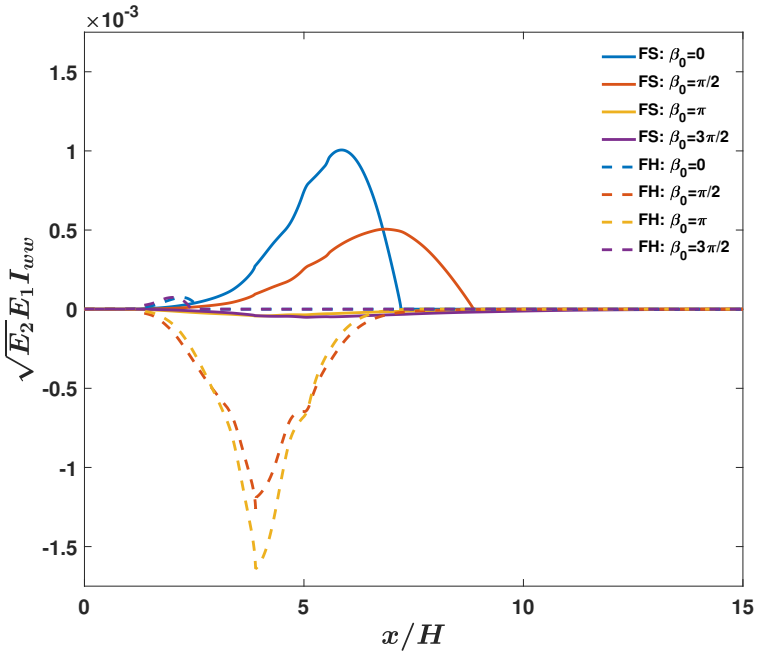

Figure 3.14 Comparison of interaction magnitude for various phase lags.

fundamental-harmonic interactions at favorable phase angles. There is significant leadup to this peak as well, so the harmonic can drain energy from the fundamental before it peaks. Compare this to fundamental-subharmonic interactions which have a more gradual growth and do not peak until x/H greater than 5. By that time, the fundamentals have already peaked, and interaction only shortens its lifespan. Past and present observations show higher frequencies peaking earlier than lower ones; thus, interaction can occur sooner to reduce the peak of the fundamental.

The present results also show that amplification of the subharmonic or harmonic is required for the interaction process to take place. To highlight this, harmonic interactions between Strouhal numbers 0.15 and 0.30 are first considered. Up until x/H of 1, the amplitude of the harmonic is very small and then sharply grows to near its natural peak. At this point the interaction becomes significant for the harmonic since its amplitude is naturally small, but now has a contribution from the fundamental. Depending on phase angle, it either absorbs or gives energy to the fundamental. In the case where it gives energy to the fundamental, the harmonic is reduced, stopping the interaction process from proceeding

and the fundamental develops as it naturally would. This is the case for initial phase lags of 0 and $3\pi/2$. However, when the harmonic drains the fundamental, it is amplified at an order of magnitude more than the fundamental gets reduced. This in turn increases the interaction, draining more energy from the fundamental until the harmonic peaks around x/H of 4, at which point dissipation overcomes the production and reduces the harmonic, ending the cycle. This same process occurs with subharmonic interactions, but at a later streamwise location.

3.4 ROM Conclusions

A methodology is presented whereby lower fidelity computations can be used to predict the nonlinear development and interaction of two harmonically related modes. This begins with the formulation of a Reduced-Order Model (ROM) that reduces the full Navier-Stokes equations to a set of coupled ODEs using an integral technique and appropriate shape assumptions. The ROM is used in conjunction with the Linearized Euler Equations where a symmetric disturbance is introduced at the nozzle exit of a supersonic rectangular jet. Fast Fourier Transform is used to obtain shape functions for various disturbance frequencies. ROM solutions without mode-mode interactions are first considered, which identified $St_H = 0.15$ as the most amplified frequency. This Strouhal number was taken as the fundamental and assumed to be the dominant noise source in the jet that needs to be reduced by adding Strouhal number 0.075 or 0.30. Fundamental-subharmonic interactions between Strouhal numbers 0.15 and 0.075 are first considered. It is shown that adding the subharmonic can be effective in reducing the lifespan of the fundamental, but not in reducing its peak, thus it is not concluded to be an effective noise reduction mechanism. Fundamental-harmonic interactions are then considered between Strouhal numbers 0.15 and 0.30, where it is shown that the peak of the fundamental can be reduced at optimal phase lags. Further examination of the interaction term in the ROM reveals that the initial phase lag is responsible for the direction of energy transfer, and only in part the magnitude. The magnitude of interaction is largely determined by the amplification or reduction of the added mode. Since

the magnitude of both interacting modes are important for the interaction process, interaction is maximized when the subharmonic or harmonic is most amplified. Natural growth explains why adding the harmonic is more effective than the subharmonic. The harmonic has a higher initial growth, which allows the interaction process to begin sooner before the peak of the fundamental is reached. Compare this to the subharmonic, which has a more gradual growth and interaction is not significant until the fundamental has already peaked. This reduced-order model has value in its ability to provide quick estimations and insight to the flow physics that can be used to guide the excitation setup of expensive computations or experiments, which can more accurately evaluate the effectiveness of the noise reduction mechanism.

4 Methodology for Large-Eddy Simulations

To apply the theory established in Chapter 3, Large-Eddy Simulations (LES) are used. The jet considered is the same as before and depicted in Fig. 3.1. This is the same jet used at the University of Cincinnati (REFS) and at The Ohio State University (REFS), establishing a strong basis for comparison. The nozzle geometry is a converging-diverging nozzle with an aspect ratio of 2:1 ($12.95mm \times 25.91mm$) and a design Mach number of 1.5. This jet is perfectly expanded with a nozzle pressure ratio of 3.67 and also heated with a total temperature ratio of $T_0/T_\infty = 3$. To non-dimensionalize quantities: lengths are non-dimensionalized by the jet exit velocity $U_{jet} = 750m/s$, density by the ambient density $\rho_\infty = 1.225kg/m^3$, and temperature by ambient temperature $T_\infty = 300K$. The equivalent jet diameter, $D_{eq} = 20.65mm$, is also defined as an alternate length scale that is used by much of the literature on rectangular jets.

4.1 Numerical Methods

The LES code used in this work is Scalible Agile Fluid Framework (SAFF), which was developed by Visbal and Gaitonde [66]. This code solves the compressible Navier-Stokes equations in strong conservative form with a curvilinear coordinate system.

$$\frac{\partial}{\partial \tau}\left(\frac{q}{J}\right) + \frac{\partial \hat{F}}{\partial \xi} + \frac{\partial \hat{G}}{\partial \eta} + \frac{\partial \hat{H}}{\partial \zeta} = \frac{1}{Re}\left[\frac{\partial \hat{F}_\nu}{\partial \xi} + \frac{\partial \hat{G}_\nu}{\partial \eta} + \frac{\partial \hat{H}_\nu}{\partial \zeta}\right] \tag{4.1}$$

Above, J is the Jacobian of the curvilinear transformation given by $J = \partial(\xi, \eta, \zeta, \tau)/\partial(x, y, z, t)$. The solution vector is denoted by $q = [\rho, \rho u, \rho v, \rho w, \rho E]^T$. Fluxes are denoted by $\hat{F}$, $\hat{G}$, and $\hat{H}$ for the ξ, η, and ζ directions respectively. The flux vectors are further described in refs. [29, 67]. The subscript, $(\ _\nu)$, denotes viscous flux vectors. Energy is defined as:

$$E = \frac{T}{\gamma\left(\gamma - 1\right) M_\infty^2} + \frac{1}{2}(u^2 + v^2 + w^2) \tag{4.2}$$

SAFF has been successfully used in several prior efforts with jet flows [29, 42, 68]. As described in ref. [29], the code uses third-order upwind-biased reconstruction in conjunction

with a Roe flux-difference split scheme [69] and harmonic limiter [70]. Viscous terms are discretized using second-order finite differencing. No explicit turbulence model is used, thus classifying this as implicit-LES (ILES). Temporal integration is performed using a second-order approximately factored Beam-Warming scheme with two sub-iterations [71].

In the code, velocities are normalized by the ambient speed of sound, c_∞, density by ambient density, ρ_∞, and pressure by ρc_∞^2. The ideal gas law is considered, $p = \rho T/\gamma$ and a constanst Prandl number of 0.7 is used. Sutherland's law is used to relate viscosity as a function of temperature and the Stoke's hypothesis is assumed for the bulk viscosity coefficient, $\lambda = -\frac{2}{3}\mu$. For all simulations, the Reynolds number is set to 570,000.

The computational domain here uses the same structured mesh as in Chakrabarti et al. [29], who previously confirmed dominant flow features to be grid independent. The grid is a single block composed of $915 \times 529 \times 629$ points in the x, y, and z directions respectively, giving the grid approximately 300 million points in total. The domain extends $40D_{eq}$ in the x-direction and $12.5D_{eq}$ in the y and z directions. Two planes of interest are defined: the minor plane, which is along the short end of the jet (height), and the major plane along the long end (width). These planes are denoted by $\psi = 0°$ for the minor plane, and $\psi = 90°$ for the major plane. Slices of the minor and major planes are shown in Fig. 4.1.

The ILES solver was run with a time step of 5×10^{-4} non-dimensional time units based on the ambient speed of sound and jet major axis length (jet width). For all statistics presented, snapshots are collected every 50 iterations for a total of 4200 samples. This gives a sampling frequency of $536kHz$ and duration of $285D_{eq}/U_{jet}$. For excited cases, a delay of $48D_{eq}/U_{jet}$ was used before sampling commenced.

4.2 Ffowcs Williams-Hawking Equations

To compute the far field noise, a Ffowcs WIlliams-Hawkings (FWH) solver was developed and used. From Di Francescantonio [72], the new variables can be defined based on ambient and fluctuation components flow variables. Here subscript ($_0$) implies ambient conditions, superscript ($'$) implies disturbances (e.g. $\rho = \rho_o + \rho'$), ρ is the density, u is the fluid velocity,

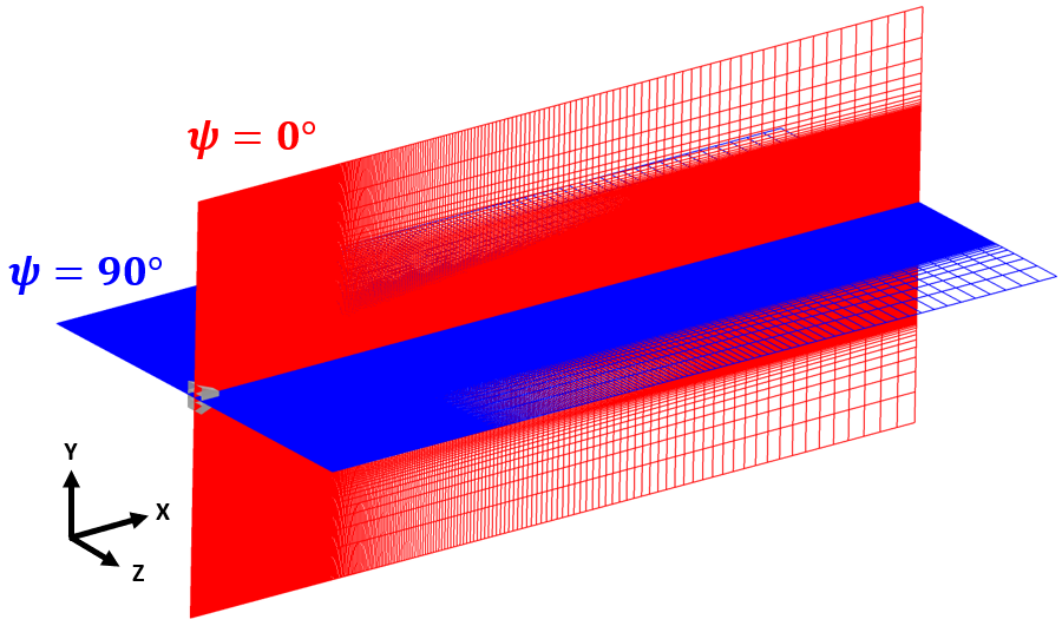

Figure 4.1 Computational domain showing minor plane (red) and major plane (blue).

and P_{ij} is the compressive stress tensor with the constant $p_o\delta_{ij}$ subtracted. Here, δ_{ij} is the Kronecker delta. The far field noise can be decomposed as follows:

$$p'(\vec{x},\ t) = p'_T(\vec{x},\ t) + p'_L(\vec{x},\ t) + p'_Q(\vec{x},\ t) \tag{4.3}$$

Here, $p'_T(\vec{x},\ t)$ is known as the thickness noise, $p'_L(\vec{x},\ t)$ is the loading noise, and $p'_Q(\vec{x},\ t)$ is the quadrupole noise pressure term that includes all sources outside the control surface. The quadrupole noise pressure term is neglected in this methodology. It has been shown by Spalart and Shur [73] that the quadrupole term is more compact in pressure FWH formulations, and less error is introduced when neglecting it. The formulation used by Mendez et al. [74] also neglects the quadrupole term and shows good agreeance for jet far field acoustics. The condition here is that the sampling surface lies outside sources of nonlinearity (i.e., vorticity). For a stationary surface, the formulation in the frequency domain is described as:

$$U_i = \frac{\rho u_i}{\rho_0} \tag{4.4}$$

$$L_i = p'\delta_{ij}n_j + \rho u_i u_n \tag{4.5}$$

$$4\pi\hat{p}'_T(\vec{x},\ \omega) = -i\omega \iint_S e^{\frac{i\omega r}{a_0}} \frac{\rho_0 \hat{U}_n}{r}\ dS \tag{4.6}$$

$$4\pi\hat{p}'_L(\vec{x},\ \omega) = -\frac{i\omega}{a_0} \iint_S e^{\frac{i\omega r}{a_0}} \frac{\hat{L}_r}{r}\ dS\ + \iint_S \frac{\hat{L}_r}{r^2}\ dS \tag{4.7}$$

In the above equations, $\vec{x}$ is the vector of observer locations. The variable, r, denotes the vector between the surface and observer. The subscript, n, denotes the component normal to the FWH surface. Equations 4.4-4.7 is the common form of the FWH equations in the frequency domain and is also given by Lyrintzis [75]. An advantage of using a frequency domain formulation is the avoidance of retarded time, which is present in all time-domain formulations [76]. A rearrangement of the equations gives the formulation presented by Mendez et al. [74], which is ultimately used in the FWH code.

$$F_1 = \frac{p'\hat{n}_j\hat{r}_j + \rho u_j u_n \hat{r}_j}{a_0 r} + \frac{\rho u_n}{r}; \quad F_2 = \frac{p'\hat{n}_j\hat{r}_j + \rho u_j u_n \hat{r}_j}{r^2} \tag{4.8}$$

$$4\pi\hat{p}(x,\omega) = \iint_S i\omega\hat{F}_1(y,\omega)e^{\frac{-i\omega r}{a_0}}\,dS + \iint_S \hat{F}_2(y,\omega)e^{\frac{-i\omega r}{a_0}}\,dS \tag{4.9}$$

The ($\hat{}$) in Eq. 4.9 denotes that the Fast Fourier Transform (FFT) has been taken. For computing FFT, a total of 4200 samples are collected on the FWH surfaces. Each time signal is separated into 5 segments with a 75% overlap. A Hanning window is then applied to each segment, and the individual FFTs are averaged using Welch's method [77]. Similar signal processing techniques have been used by Prasad and Unnikrishnan [44].

The placement of the FWH surfaces is chosen such that it is as close as possible to the noise sources, while remaining outside of nonlinear regions. Nonlinearities arise due to vorticity, thus the surfaces were placed just outside the region of large time-averaged vorticity, which is shown in Fig. 4.2. Additionally for the case of the jet, outflow caps are additionally included to fully enclose the noise sources. This introduces some complexity because noise sources permeate these surfaces. Mendez et al. [74] describe how to treat

these based on the work of Shur et al. [78]. Multiple outflow caps are used and a weighted average is applied to each cap solution. Equation 4.9 becomes:

$$4\pi\hat{p}\left(\vec{x},\omega\right)=\iint_{S}\Psi\left(y\right)\left(i\omega\hat{F}_{1}\left(y,\omega\right)+\hat{F}_{2}\left(y,\omega\right)\right)e^{-\frac{i\omega r}{c_{\infty}}}dS \tag{4.10}$$

The weighting function, $\Psi(y)$, is simply 1 if the surface is not an end cap, and $1/N_{caps}$ if the surface is an end cap. In this work, 4 end caps are used beginning at a streamwise location of $18D_{eq}$ and spaced every $2D_{eq}$. Sound pressure level (SPL) spectra and overall sound pressure levels (OASPL) are then computed using the equations below from Mendez et al. [79].

$$SPL\left(\vec{x},St\right)=10\log_{10}\left[\frac{2\hat{p}\left(\vec{x},\omega\right)\hat{p}^{*}\left(\vec{x},\omega\right)}{St_{min}p_{ref}^{2}}\right] \tag{4.11}$$

$$OASPL\left(\vec{x}\right)=10\log_{10}\left[\sum_{St=St_{min}}^{St_{max}}\frac{2\hat{p}\left(\vec{x},\omega\right)\hat{p}^{*}\left(\vec{x},\omega\right)}{p_{ref}^{2}}\right] \tag{4.12}$$

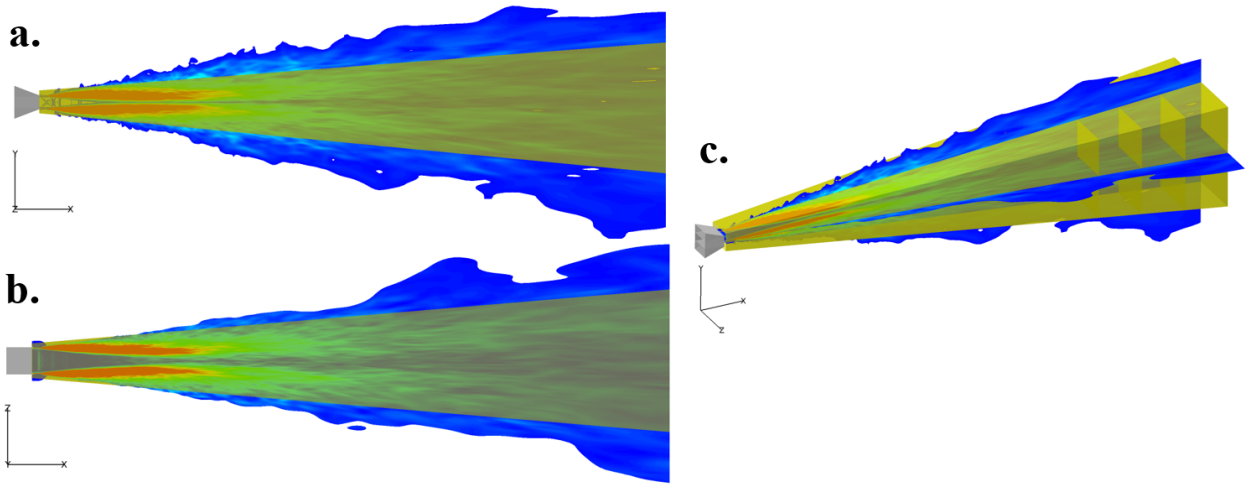

Figure 4.2 Ffowcs Williams-Hawkings surfaces plotted with time-averaged vorticity in a) minor plane, b) major plane, c) isometric view showing end-caps.

The FWH solver is validated using the unexcited baseline case and comparing directly with Mora et al. [33] and Viswanath et al. [63], which consider the same jet in both experiment and computation respectively. They also use the same observer locations, which

are also adopted in this work. For all cases, observers are placed in an arc at a radial location of $40D_{eq}$, measured from the jet exit plane at the centerline. Arcs are taken in both the minor ($\psi = 0°$) and major ($\psi = 90°$) planes. Observer definitions can be visualized in Fig. 4.3. Solver validation is shown later in Sec. 5.1.

A cutoff frequency was computed assuming 12 points per wavelength required to resolve any wave. A previous study by Salehian and Mankbadi [1] used 15 points per wavelength with a second order scheme. Tam and Webb [80] show that high order compact schemes can resolve waves with less than 8 points per wavelength. The present study lies somewhere in between being a 3rd order scheme, thus using 15 points per wavelength. Using the grid spacing where the peak noise sources originate, this gives a maximum resolved Strouhal number of $St_H = 1.92$.

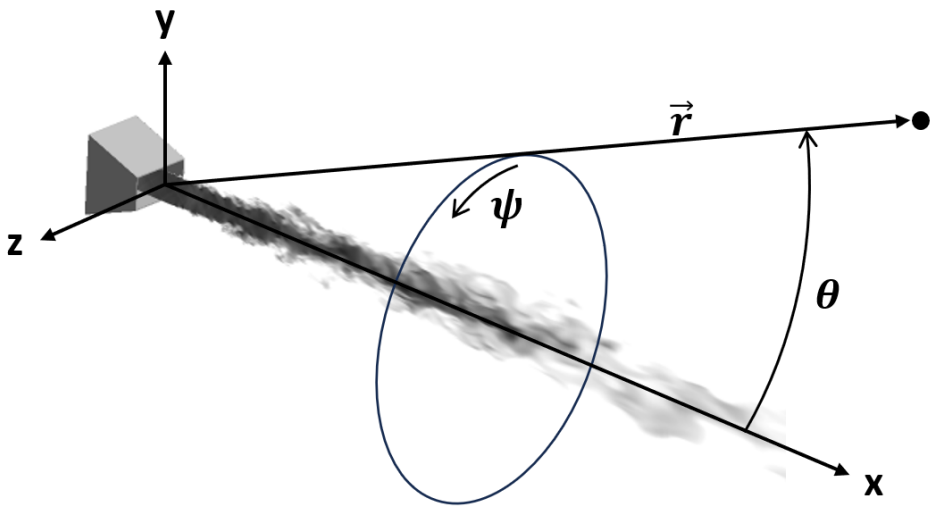

Figure 4.3 Schematic showing coordinate system for observers.

4.2.1 Code Overview

The FWH code was written using the Julia programming language [81]. It is designed to work with Plot3D solution files and using Message Passing Interface (MPI) for parallelization. Multi-patch FWH surfaces can be handled as used in this work.

The code consists of an outer loop that moves across the different FWH surfaces. The grid is read in and grid metrics are computed (i.e. unit normals, differential areas). Solution files

are then read in parallel and stitched together on a master processor. Spatial coordinates are then split using the "PencilArrays" package and local chunks are distributed to each processor.

An inner loop begins, which moves across the different observer locations. Vectors between the surface locations and observers are computed, followed by the F_1 and F_2 source terms given in Eq. 4.8. The Fast Fourier Transform (FFT) is computed for the source terms, which can be performed with specified overlapping in the time domain and various types of windowing functions. The integrand in Eq. 4.10 is computed. The resultant integrand is then multiplied by its respective differential area for all frequencies, which is then summed together for the final integral solution. The code's outer loop then moves on to the next patch comprising the FWH surface and the process repeats.

5 Evaluation of the Unexcited Baseline Case

The results begin with the unexcited, baseline case, which provides a basis for comparison of the excited case and to identify a dominant coherent structure to target for the excitation cases. Detailed analysis of this case is also presented by Salehian et al. [82]. An instantaneous snapshot of Mach number in the minor and major planes are shown in Fig. 5.1.

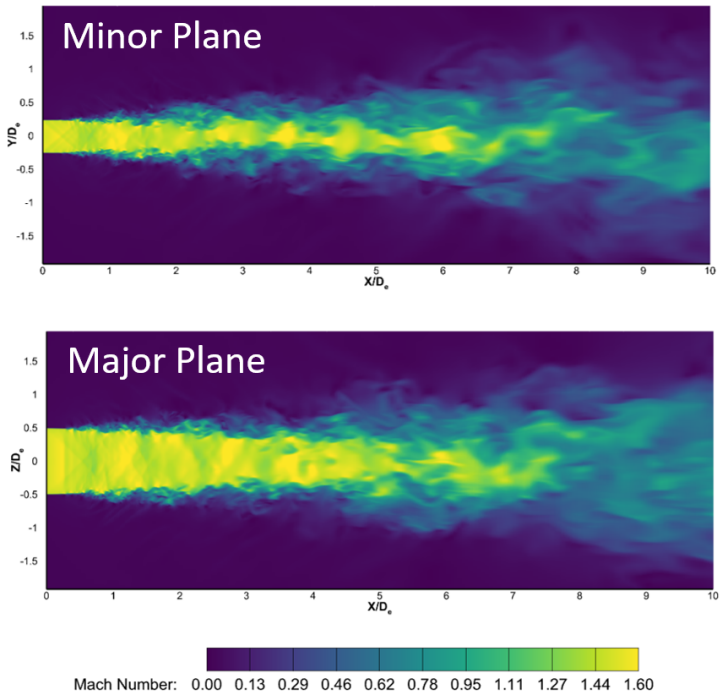

Figure 5.1 Instantaneous Mach number for baseline jet in minor and major planes.

The first task is to determine whether the minor or major plane is of more interest. Pressure spectra at the near nozzle lip in the minor and major planes are shown in Fig. 5.2. The spectra here is computed using Welch's method [77] with 4200 total samples split into 4 segments with 25% overlap. The spectra in the minor plane of the jet shows considerably more fluctuations than the major plane. The major plane shows very few fluctuations. Differences in the pressure fluctuations between planes is not entirely unexpected because the expansion in the nozzle occurs in the minor plane, whereas the nozzle contour in the major plane is flat. The minor plane spectrum also shows a distinct peak at $St_H = 0.15$, which is consistent with the most amplified Strouhal number from the ROM (see Chapter

2).

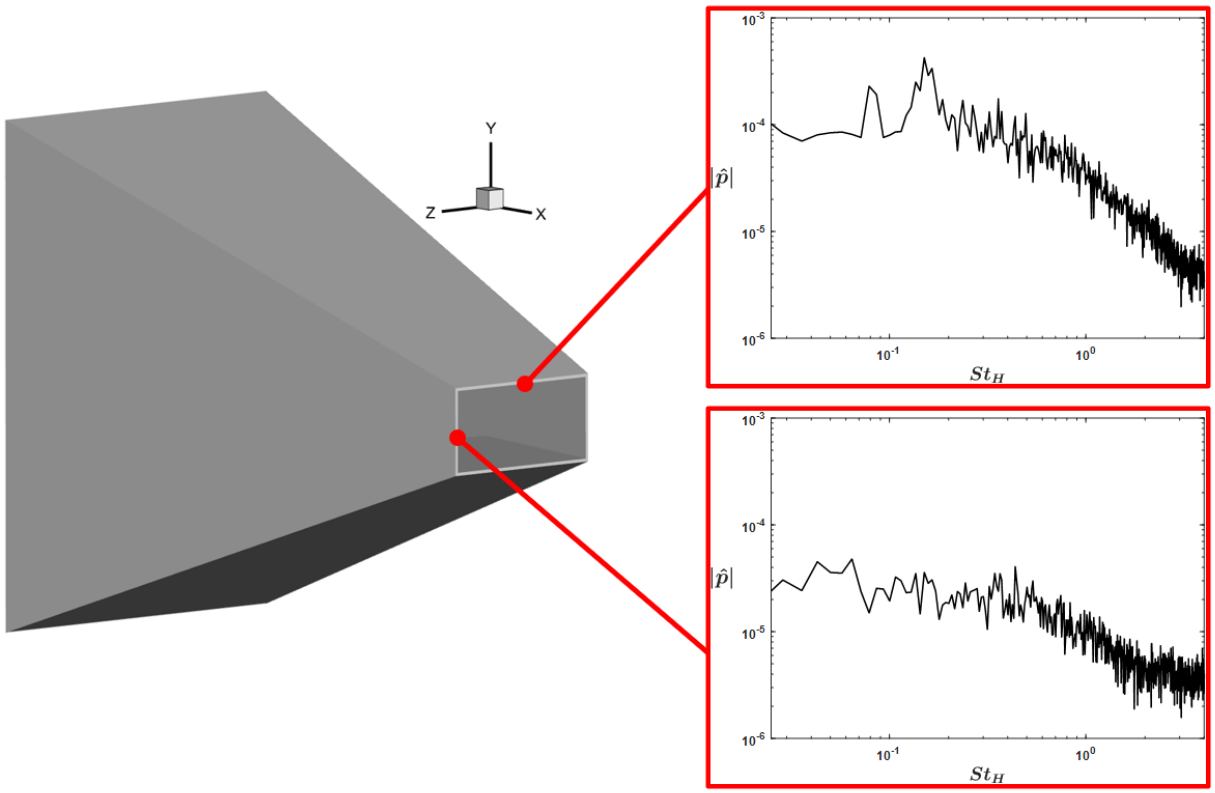

Figure 5.2 Near nozzle pressure spectra in minor and major plane.

Figure 5.2 also gives a Strouhal number range to narrow focus on. Figure 5.3 shows contours of the pressure magnitude for a range of Strouhal numbers between 0.075 and 0.30. Strouhal number 0.15 is shown to significantly amplify downstream and spread into the far field. This kind of behavior is not observed for other Strouhal numbers.

5.1 Baseline Far Field Analysis

Far field overall sound pressure levels for the baseline case given in Fig. 5.4 show excellent agreement with the previously published results [33, 63]. Peak values in the directivity differ by less than 1dB in both planes of interest. The spectra shown in Fig. 5.5 also exhibits close agreement with experiment [33]. The peak noise in the present study occurs at a polar angle of approximately 50° in both minor and major planes.

The spectra at the peak angle in the minor and major planes are shown in Fig. 5.6.

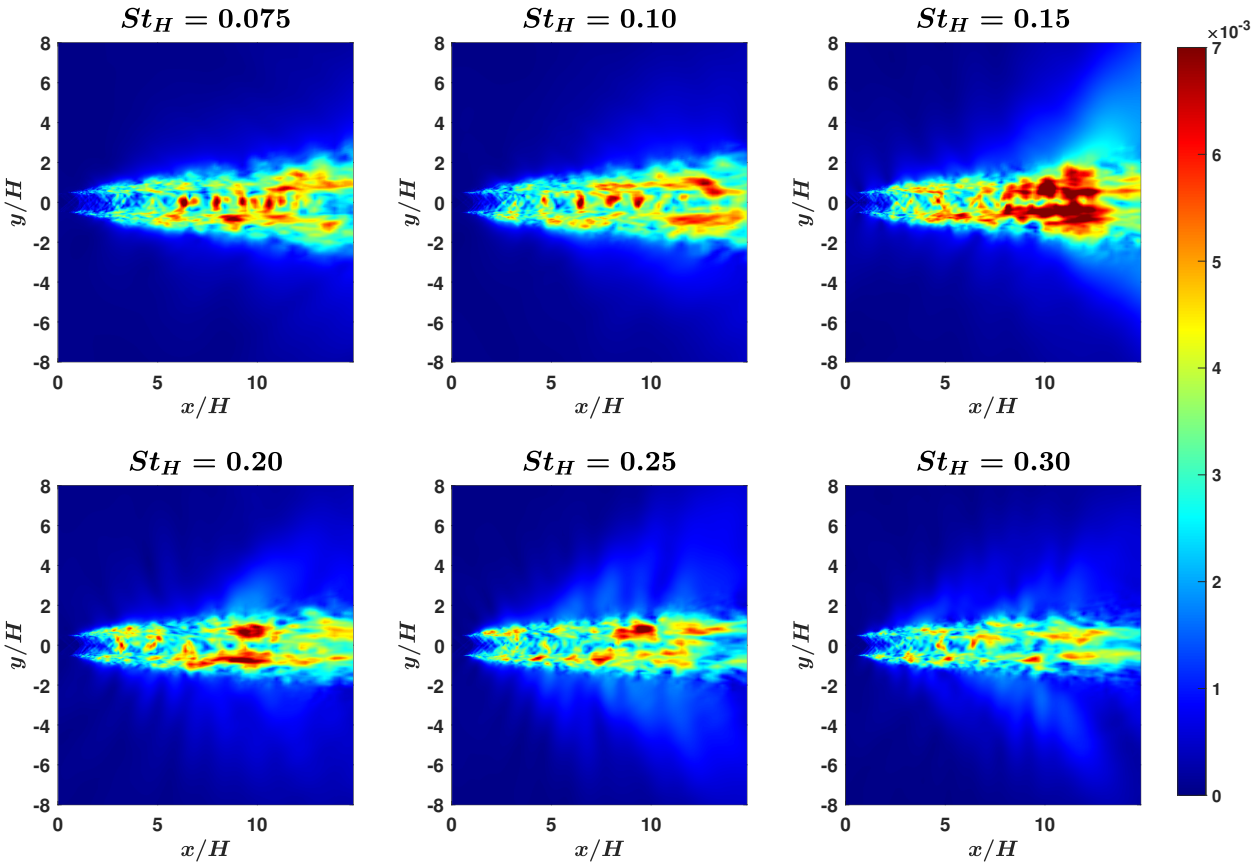

Figure 5.3 Pressure magnitudes at various Strouhal numbers for baseline case.

For both planes, there is a distinct peak for $St_H = 0.25$, with a secondary peak around Strouhal number 0.13. So even though Strouhal number 0.15 is the most amplified in the near field, it is not the dominant noise source at the peak directivity angle. To visualize where different frequencies appear in the far field, Fig. 5.7 shows a heat map of SPL against Strouhal number for directivity angles near the peak. It is shown here that Strouhal number 0.25 occupies a confined range of directivity angles around the peak between $\theta = 47°$ and $\theta = 52°$. It is also shown that Strouhal number 0.15 has a strong presence from 30° to 50°. For lower polar angles between 32° and 46°, the Strouhal number 0.15 is dominant, which is consistent with the near field coherent structures from Fig. 5.3. Another observable trend is that as the polar angle increases, the peak Strouhal number also increases.

There are several other works that have covered the same jet used here and there are some variations in the peak directivity and dominant frequencies. Most of these studies report

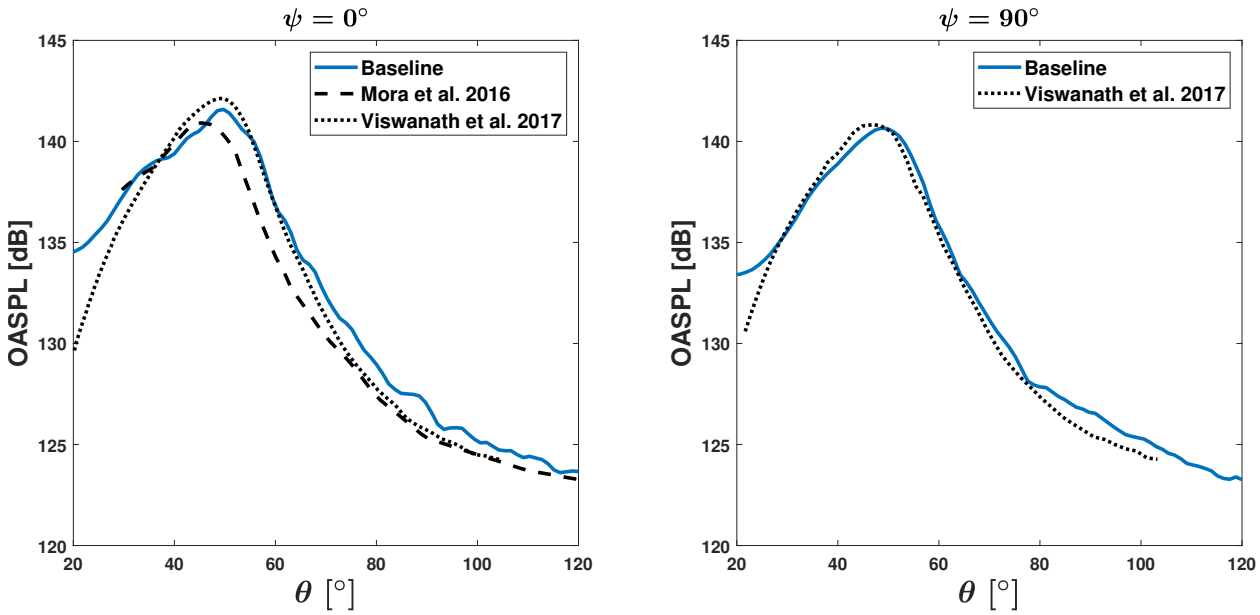

Figure 5.4 Directivity comparison for baseline case in the minor (left) and major (right) planes.

Strouhal number based on the equivalent nozzle diameter, $St_D = fD_{eq}/U_j$, whereas this work uses the height, $St_H = fH/U_j$. For consistency, results from others have been converted to use the St_H convention. Experiments by Mora et al. [33] found a peak directivity between 28° and 44° in the minor plane with peak Strouhal numbers ranging from $St_H = 0.06 - 0.13$. Their peak directivity is at a slightly lower polar angle than the present study, but the peak frequency at those lower angles is comparable as is shown in Fig. 5.5. This study compares very well with the results of Viswanath et al. [63], but with a slightly higher peak directivity angle. Their peak frequency was similar to Mora et al. [33] at $St_H = 0.13$. This study finds the same peak directivity of Crawley et al. [30] at a polar angle of $\theta = 50°$. The baseline case by Mankbadi and Salehian [34] found a lower peak frequency at $St_H = 0.06$. Gojon et al. [8] considered the same jet at a slightly overexpanded operating condition and found $St_H = 0.10$ as the dominant noise. They also showed that the peak shock associated noise corresponded with $St_H = 0.27$. Prasad and Unnikrishnan [44] considered the same jet, but issued from a constant area duct, removing the shocks, and found the peak noise between Strouhal number 0.076 and 0.152. This work ultimately finds a similar peak directivity to

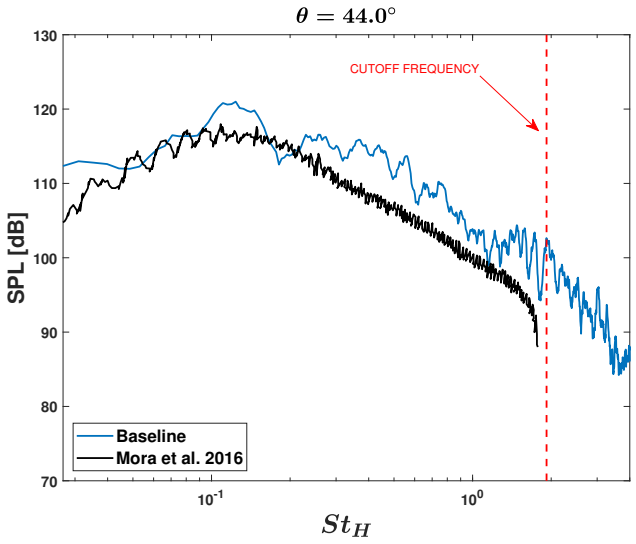

Figure 5.5 Spectra comparison in minor plane for baseline case.

the previous works and peak Strouhal numbers in the same range. An earlier study using near field FFT and SPOD analysis also highlighted the significance of Strouhal number 0.15 and correlated it to the primary radiation angle in the far field [82].

5.2 Conclusions from Baseline Case

Figure 5.3 shows Strouhal number 0.15 to be the most amplified coherent structure in the near field, which shows up as a secondary spectrum peak at the peak emission angle and as the peak frequency for emission angles slightly less than the peak one. The theory proposed by Malczewski and Mankbadi [56] and in Chapters 2-3 also demonstrated the role of natural amplification to initiate fundamental-harmonic interactions, and it is evident that Strouhal number 0.15 is more amplified. Even though 0.25 is the peak Strouhal number at the peak emissivity angle, Strouhal number 0.15 still plays a major role and is more suitable to target with excitation. Thus, Strouhal number 0.15 is taken as the fundamental that should be reduced by interactions with the harmonic, Strouhal number 0.30, which will be added via excitation. Based on the results shown in Figs. 5.6 and 5.7, reduction of Strouhal number 0.15, should generate noise reduction for polar angles between 30° and 52°.

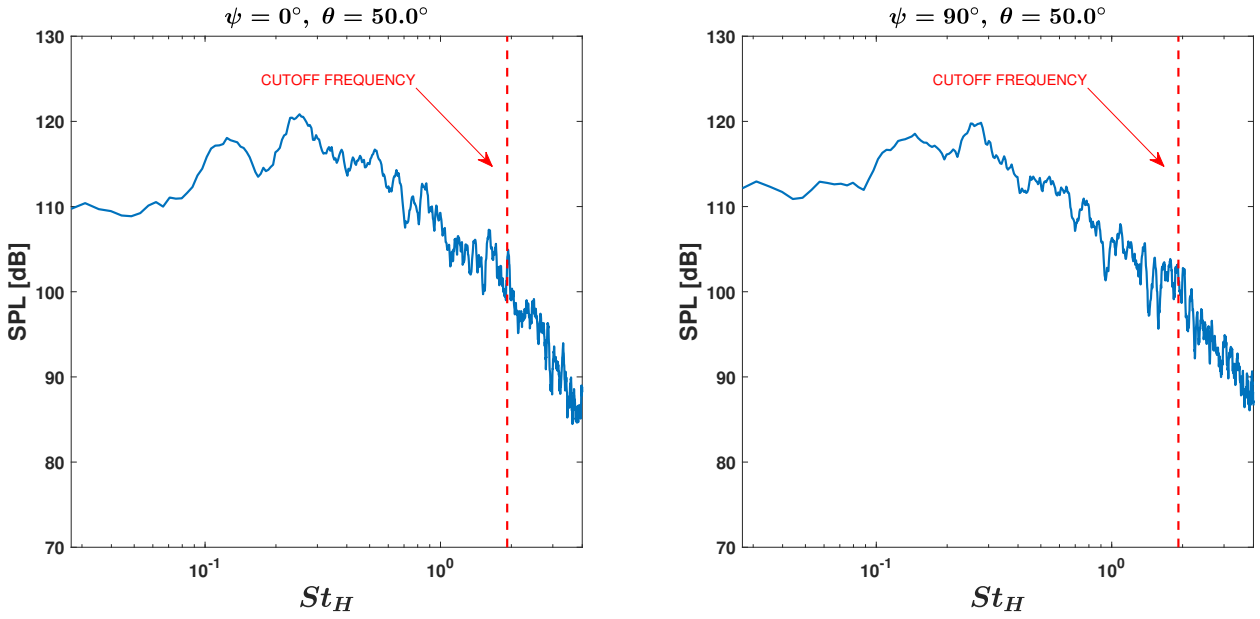

Figure 5.6 Spectra at peak polar angle for baseline case for minor plane (left) and major plane (right).

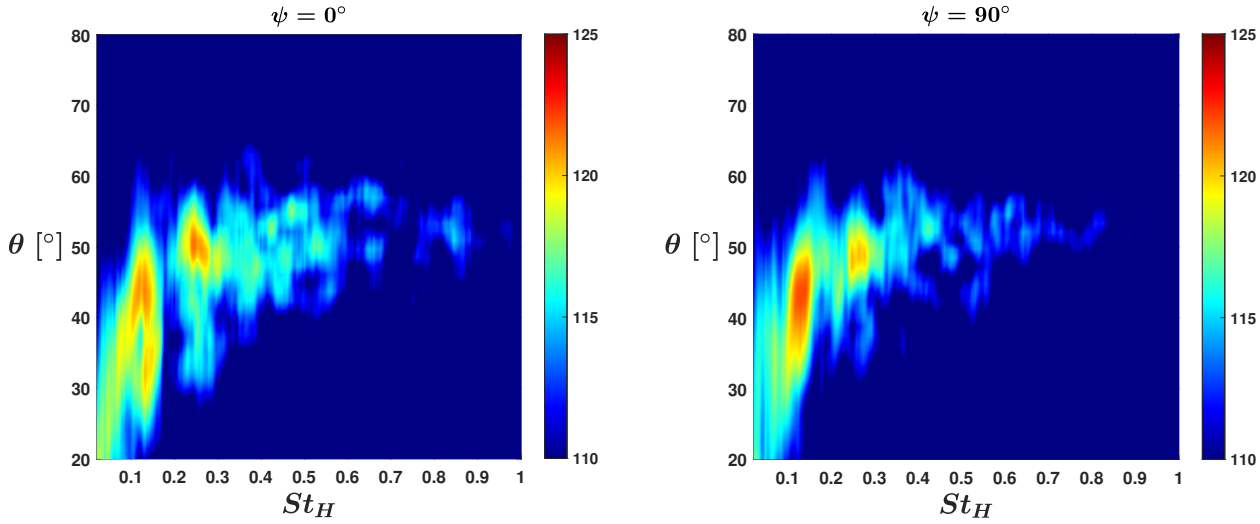

Figure 5.7 Contour of SPL for baseline case in minor plane (left) and major plane (right).

6 Bi-Modal Excitation of the Jet

Excitation is imposed using actuation strips along the upper and lower nozzle lips near the exit, which are shown in Fig. 6.1. The actuation strips span the entire width of the nozzle. This is different from other works with excitation, which have smaller actuators placed along the width, giving a z-periodicity in the major plane [42, 44]. This work is putting into practice the ROM developed by Malczewski and Mankbadi [56], which did not include z-periodicity in the disturbance shape functions, thus the actuators span the entire nozzle width for consistency.

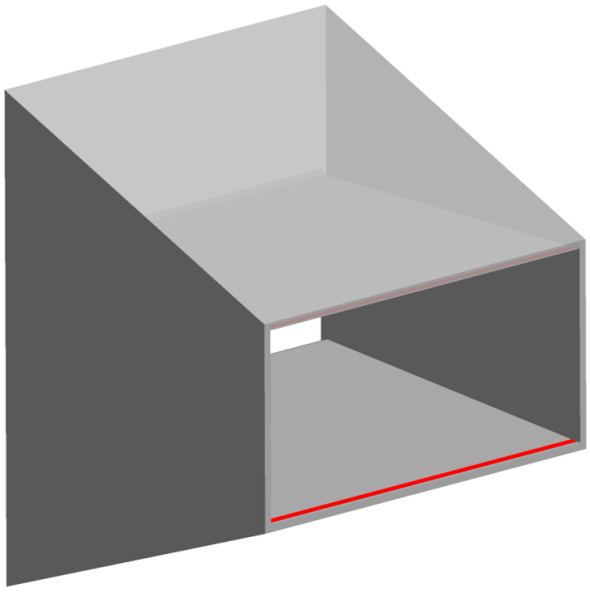

Figure 6.1 Nozzle showing actuation strips in red.

The actuators function by imposing a small periodic pressure fluctuation. Two types of excitations are considered: single-mode excitation, and bi-modal excitation, which take the form of Eqs. 6.1 and 6.2 respectively and are depicted graphically in Fig. 6.2. For all cases, the upper and lower actuators work in-phase with each other. For the single-mode case, the jet is excited with twice the frequency of the most amplified mode in the near field. As was shown in Chapter 5, $St_H = 0.15$ is the most amplified coherent structure in the near field, which will be referred to as the fundamental, f. From the ROM [56], interactions with $2f$ should reduce the fundamental, so the single-mode case is excited with $St_H = 0.30$.

The amplitude of the single-mode forcing is chosen such that it on the order of $St_H = 0.15$ near the nozzle exit, which works out to 0.4% of the mean pressure in that region. Even though the single-mode case is only forcing a single frequency, it can still be thought of as bi-modal excitation because Strouhal number 0.15 is naturally excited. For the bi-modal cases, excitation is prescribed with two frequencies, $St_H = 0.15$ and 0.30. This is done to control the phase lag, β_0, between the two frequencies, which is shown to have an effect by Malczewski and Mankbadi [56]. Here, the forcing amplitudes here have been increased to 1% of the time-averaged pressure for better control over the initial phase lag. In either excitation case, the amplitude is very small, on the order of acoustic fluctuations and the actuators used are representative of a speaker.

$$p_{act} = \bar{p}\left(1 + A\sin\left(\omega_{2f}t\right)\right) \tag{6.1}$$

$$p_{act} = \bar{p}\left(1 + A\sin\left(\omega_{f}t\right) + A\sin\left(\omega_{2f}t + \beta_0\right)\right) \tag{6.2}$$

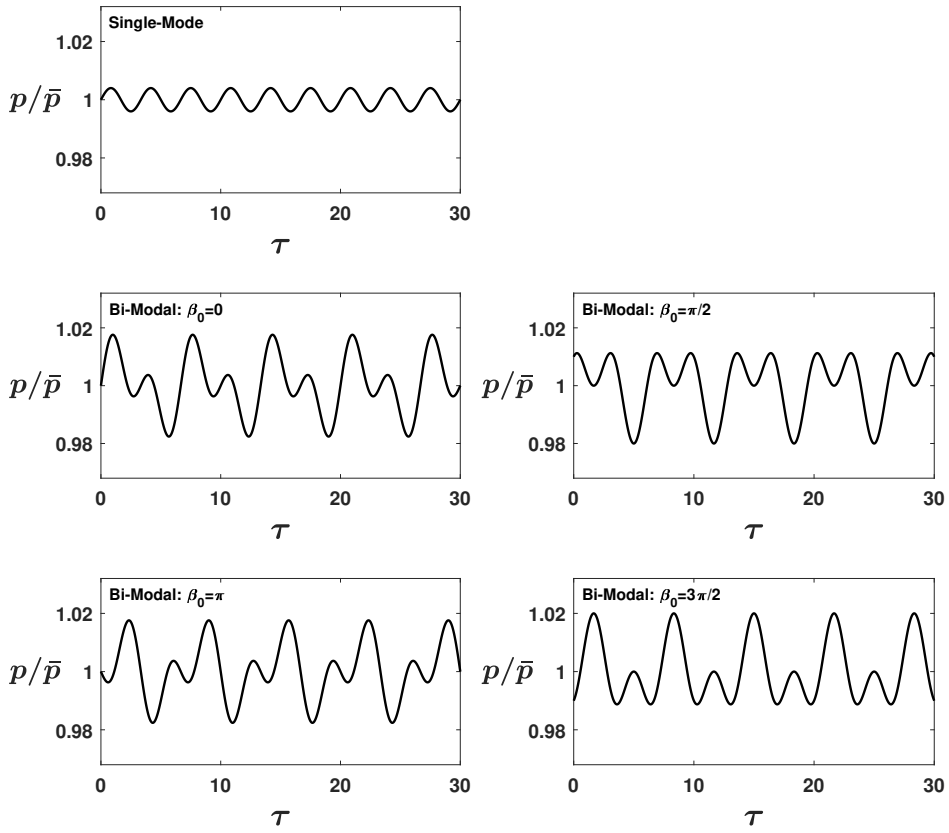

Figure 6.2 Actuation signals for single-mode and bi-modal cases.

6.1 Single-Mode Excitation

The first case considered is that of a single forcing mode at $St_H = 0.30$, which takes the form given in Eq. 6.1. In this case, the phase between Strouhal numbers 0.15 and 0.30 is not controlled. Malczewski and Mankbadi (2023) showed that on average, the addition of the harmonic should reduce the fundamental since it is not very amplified naturally. It is recalled that the amplitude of the forced pressure disturbance is small, on the order of 0.4% of the time-averaged pressure at the nozzle exit.

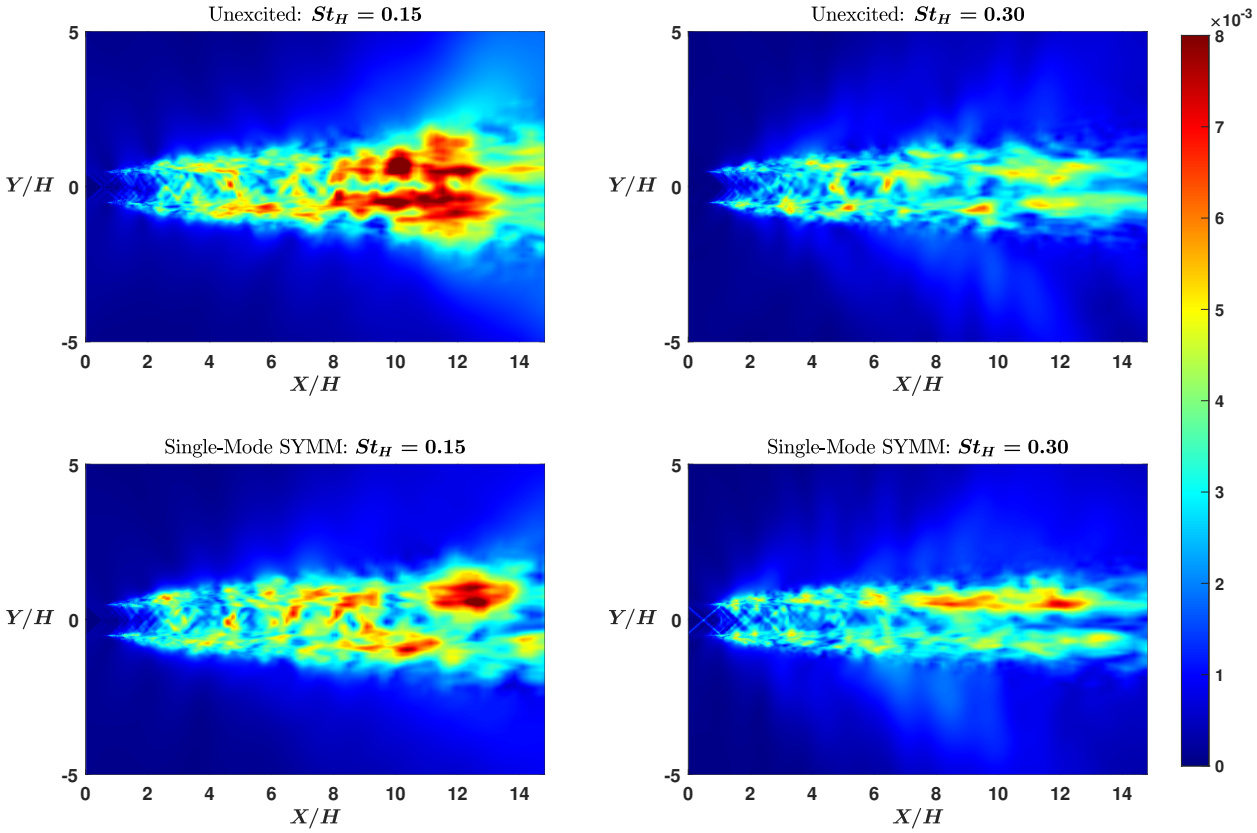

Figure 6.3 Near field minor plane contours of $|\hat{p}|$ for Strouhal numbers 0.15 and 0.30; compared are the baseline case and single-mode excited case.

Figure 6.3 shows a comparison of pressure contours for Strouhal numbers 0.15 and 0.30 between the excited and baseline case. Qualitatively, there is considerable reduction of Strouhal number 0.15. The forced Strouhal number, 0.30, does not considerably amplify downstream for the excited case, so actuation tones should be absent in the far field spectra. The symmetric structure of the excitation is also clearly visible up to $X/H = 4$. To better quantify changes in the near field coherent structure, the contours in Fig. 6.3 were integrated along the y-direction using Eq. 10.

$$I\left(x, St_H\right) = \int_{-\infty}^{\infty} \left|\hat{p}\left(x, y, St_H\right)\right| dy \tag{6.3}$$

This integration is shown in Fig. 6.4. The reduction of Strouhal number 0.15 is again very apparent at streamwise locations of $X/H > 10$. Strouhal number 0.30 sees some

amplification over a broad range. The peak is only slightly larger than in the baseline case and the peak occurs sooner, slightly before $X/H = 10$.

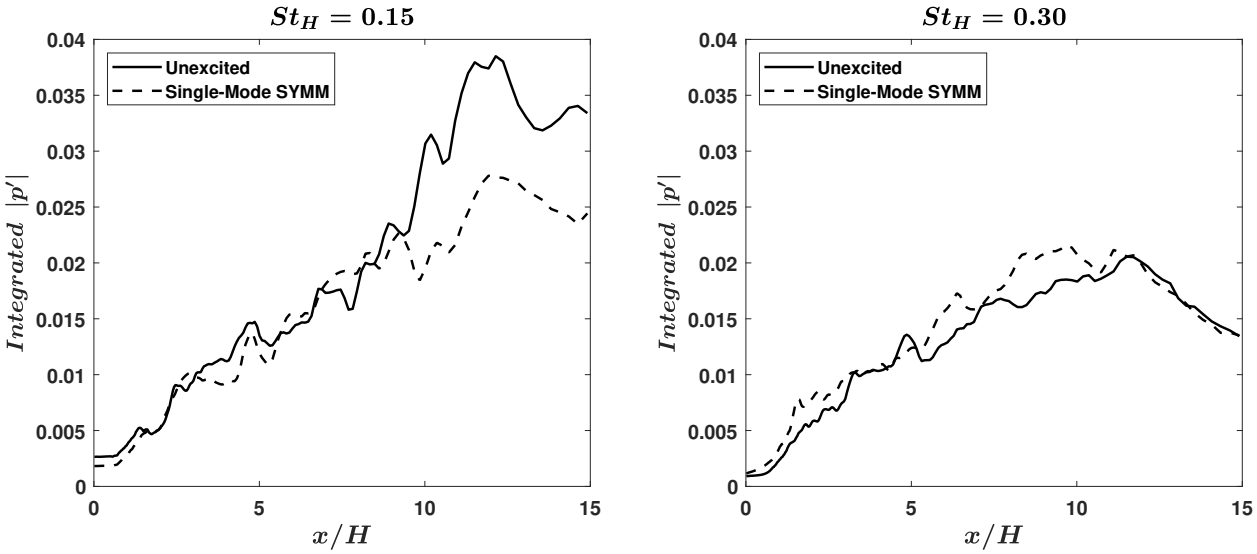

Figure 6.4 Integrated pressure comparing baseline and single-mode excited cases; Strouhal numbers 0.15 (left) and 0.30 (right) are displayed.

Far field noise directivity is shown in Fig. 6.5. In the minor plane, there is a slight increase in the peak-to-peak noise, about 0.3dB. However, in the major plane, there is a peak-to-peak noise reduction of 1dB. In both planes, the peak emissivity angle remains 50°. The differences in OASPL across polar angles are plotted in Fig. 6.6 where negative values indicate reduction. In the minor plane, there is up to a 1dB decrease in the noise for low polar angles between 21° and 39°. The major plane exhibits a noise reduction across almost the entire range of polar angles. Notably it sees a reduction of approximately 1dB for all angles between 30° and 62°. In Chapter 5, it was shown that Strouhal number 0.15 had a strong presence for polar angles between 30° and 52° either as the primary or secondary peak. The excited case shows a reduction in the strength of this Strouhal number and is showing reduction at the polar angles where Strouhal number 0.15 was dominant.

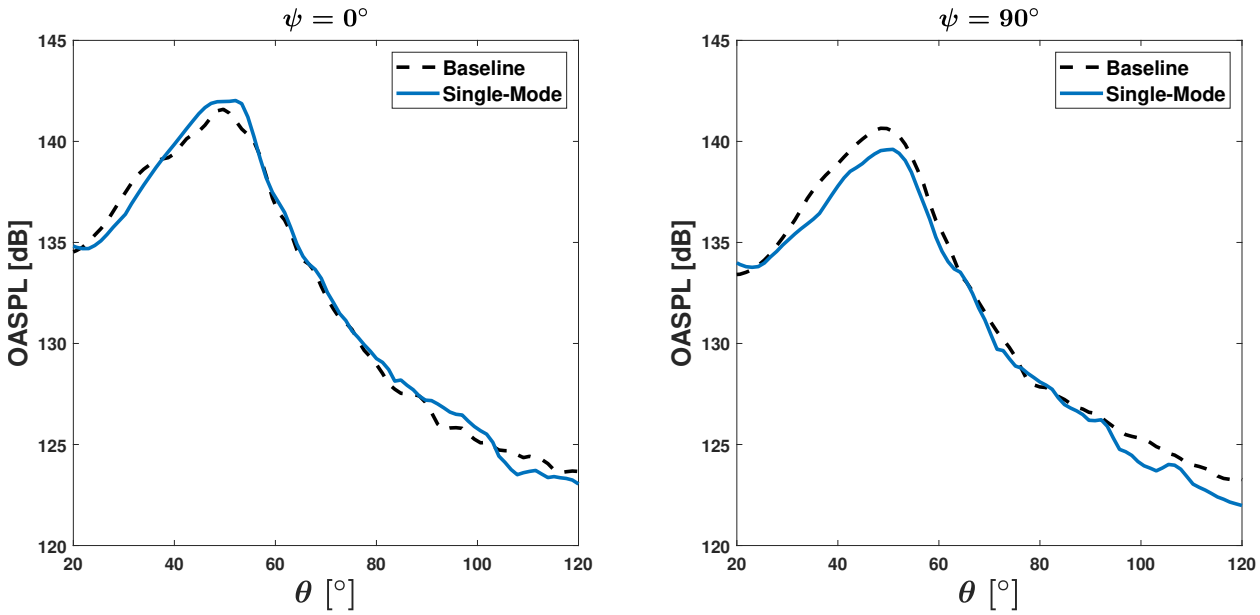

Figure 6.5 Minor (left) and major (right) plane OASPL comparison with single-mode excitation.

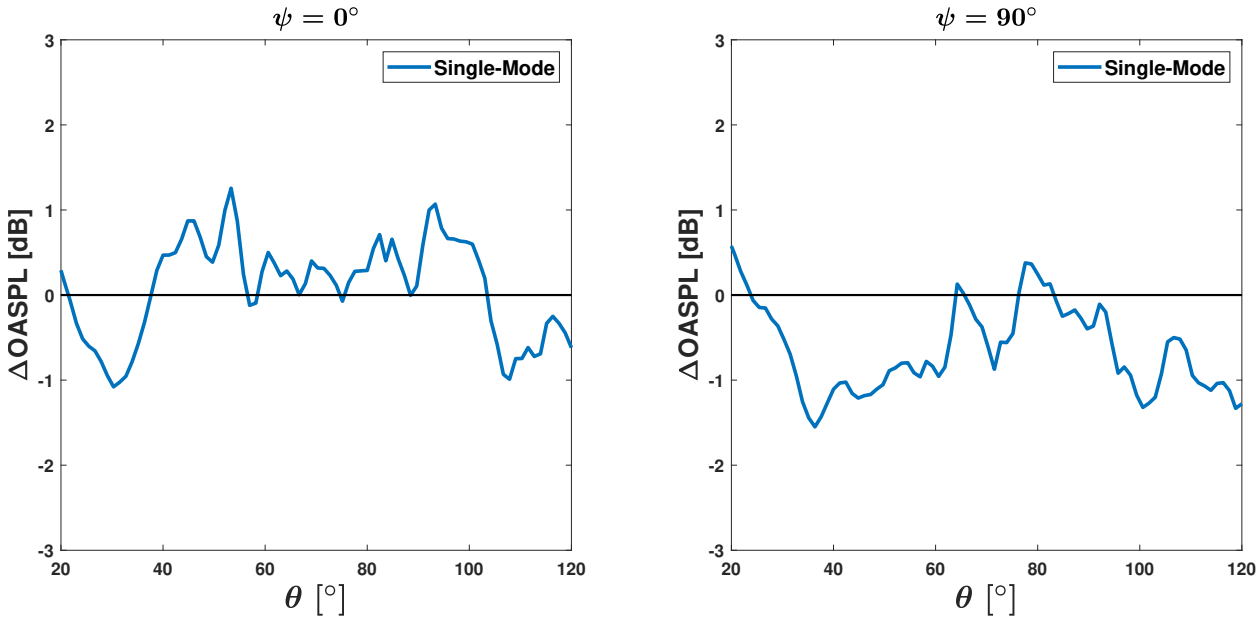

Figure 6.6 Minor (left) and major (right) plane $\Delta OASPL$ for single-mode excitation; negative values indicate noise reduction.

Spectra at the peak emissivity angle are shown in Fig. 6.7. In the minor plane, there is an increase in the noise between Strouhal numbers 0.15 and 0.20, which is where the rise in OASPL comes from. The major plane sees a drastic decrease in noise around the peak of

Strouhal number 0.25, reducing OASPL by up to 1dB. It is noted that at the peak emissivity angle, Strouhal number 0.15 was not the dominant peak. An additional spectra comparison is shown for $\theta = 35°$ in Fig. 6.8 where Strouhal number 0.15 was the dominant frequency in the unexcited case and there was almost a 1dB overall noise reduction. In the minor plane, there is a reduction of Strouhal number 0.15, which led to a reduction of the OASPL. This aligns with the theory from Chapters 2 and 3 [56], whereby dominant frequencies can be reduced by their harmonics.

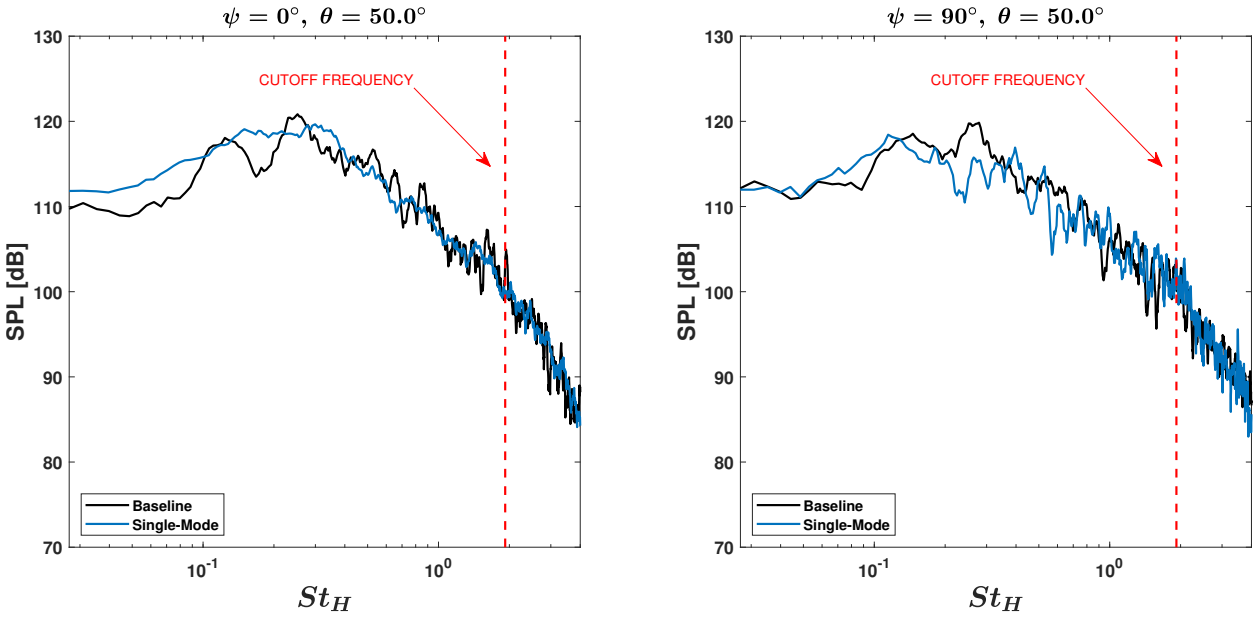

Figure 6.7 Comparison of spectra at peak emissivity angle for single-mode excitation.

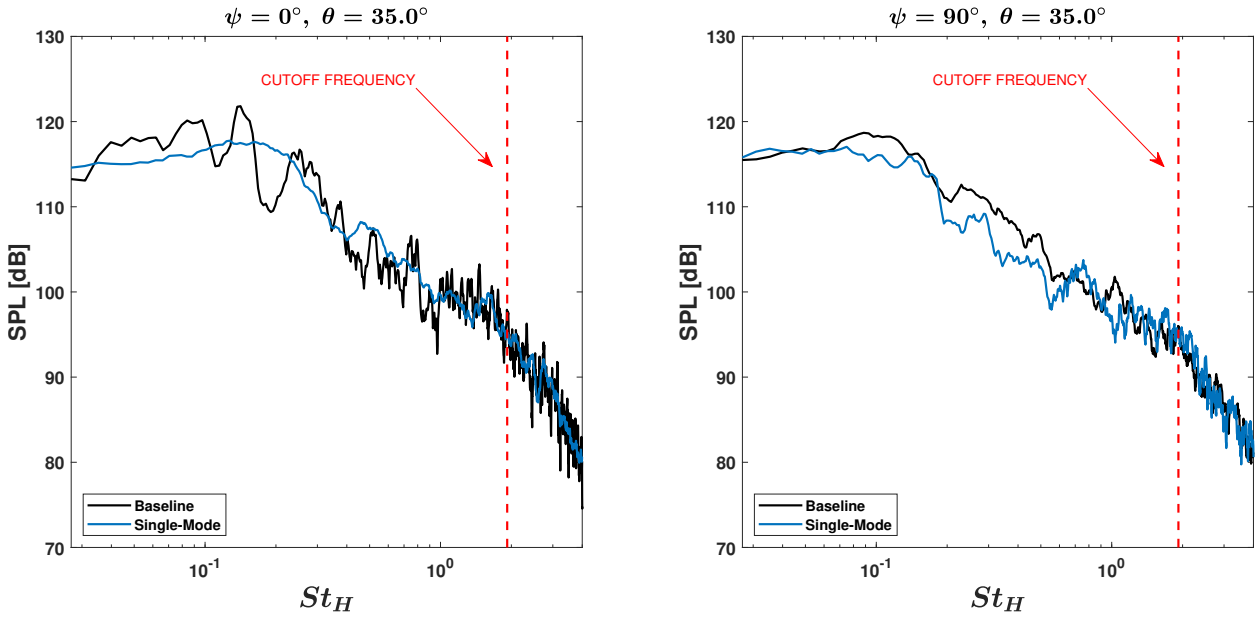

Figure 6.8 Comparison of spectra at $\theta = 35°$ for single-mode excitation.

Spectral proper orthogonal decomposition (SPOD) is used to separate the spectra into energy containing modes [83]. The real component of the first and second modes are shown in Figs. 6.9 and 6.10 respectively. The figures show that the excitation had very little effect on the first mode. However, significant differences are seen in the second mode. Here, the turbulent structures Strouhal number 0.15 are significantly broken up. In the baseline case, they formed into coherent structures at $X/H = 7$, but in the excited case, this is delayed to $X/H = 12$. It is not surprising that the excitation affects higher order modes since it is prescribed at a low forcing amplitude.

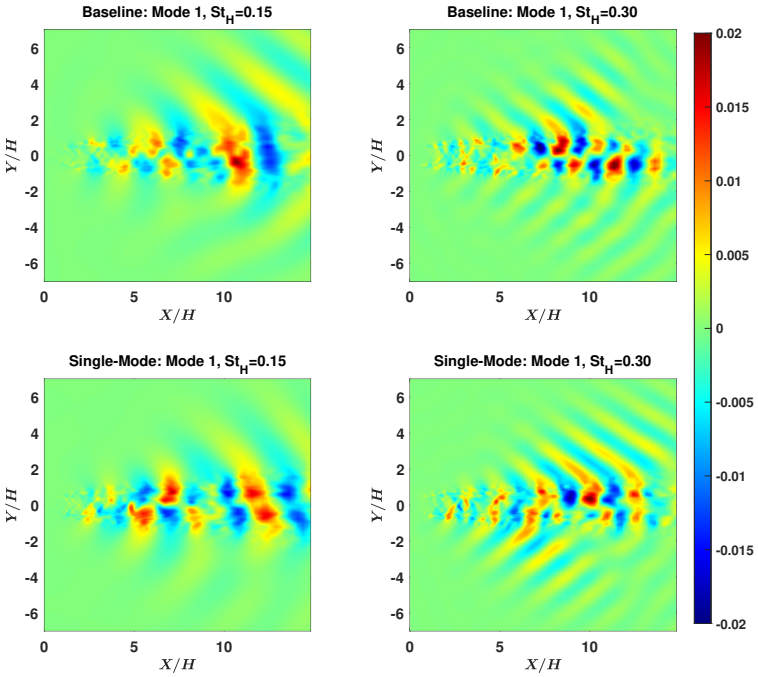

Figure 6.9 First mode SPOD contours comparing baseline and single-mode excited case; shown are Strouhal numbers 0.15 and 0.30.

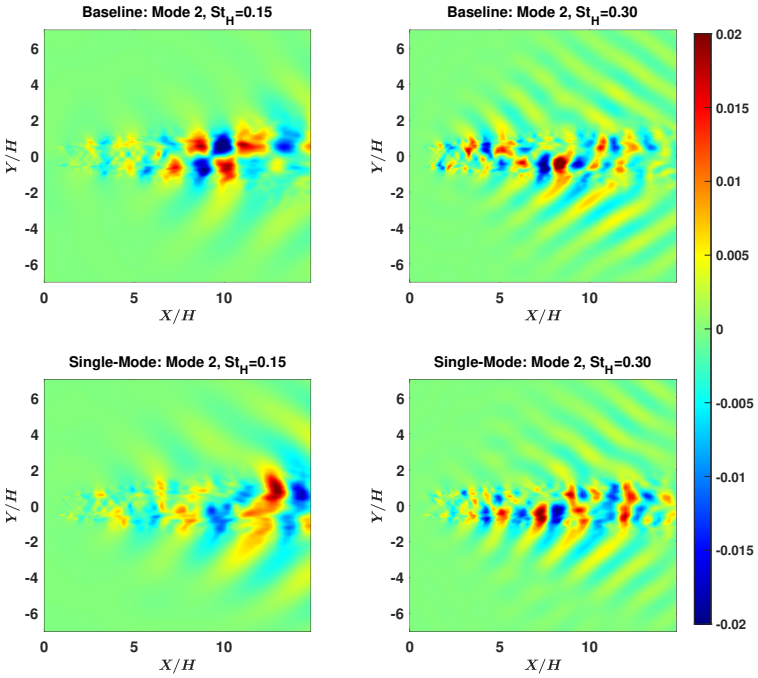

Figure 6.10 Second mode SPOD contours comparing baseline and single-mode excited case; shown are Strouhal numbers 0.15 and 0.30.

6.2 Bi-Modal Excitation

The cases of bi-modal excitation are now considered. Here, the jet is excited with two frequencies, Strouhal numbers 0.15 and 0.30, in accordance with Eq. 6.2. This is done to exert control over the phase lag between the two frequencies. Four cases are run with different phase lags, 0, $\pi/2$, π, and $3\pi/2$. Again, there is no phase difference between the upper and lower actuation strips. The forcing amplitude here has been increased to a 1% fluctuation of the mean pressure, which is imposed for both frequencies.

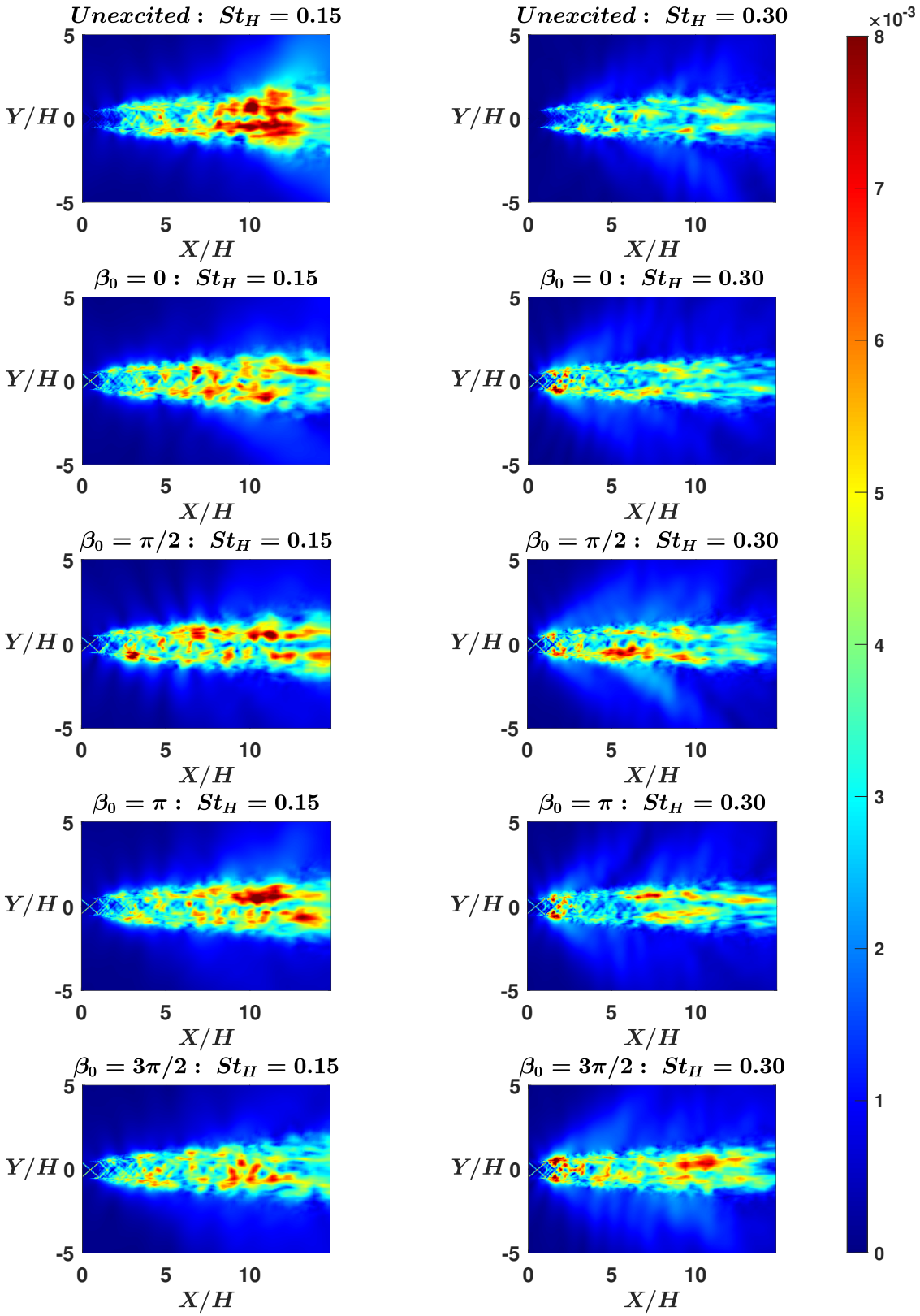

Figure 6.11 Near field minor plane contours of $|\hat{p}|$ for Strouhal numbers 0.15 and 0.30; compared are the baseline case and all bi-modal excited cases with different phase lags.

Figure 6.11 shows the near field pressure contours for the bi-modal cases. Qualitatively, each of the bi-modal cases appear to have reduced Strouhal number 0.15. However, the extent of reduction is significantly different depending on the initial phase lag. Strouhal number 0.30 shows a clear amplification for all excited cases, with a sharp initial peak occurring at $X/H = 1.5$. This is quantified in Fig. 6.12 showing the integrated pressures using Eq. 6.3. Interestingly, all cases show a reduction of Strouhal number 0.15 for $X/H > 10$. There are varying levels of reduction with phase lags of $\beta_0 = \pi/2$ and $\beta_0 = 3\pi/2$ showing the most reduction. Incidentally, these two cases also show the most amplification of Strouhal number 0.30. This further supports the theory that the noise reduction mechanism is a transfer of energy from the dominant noise source to its harmonic.

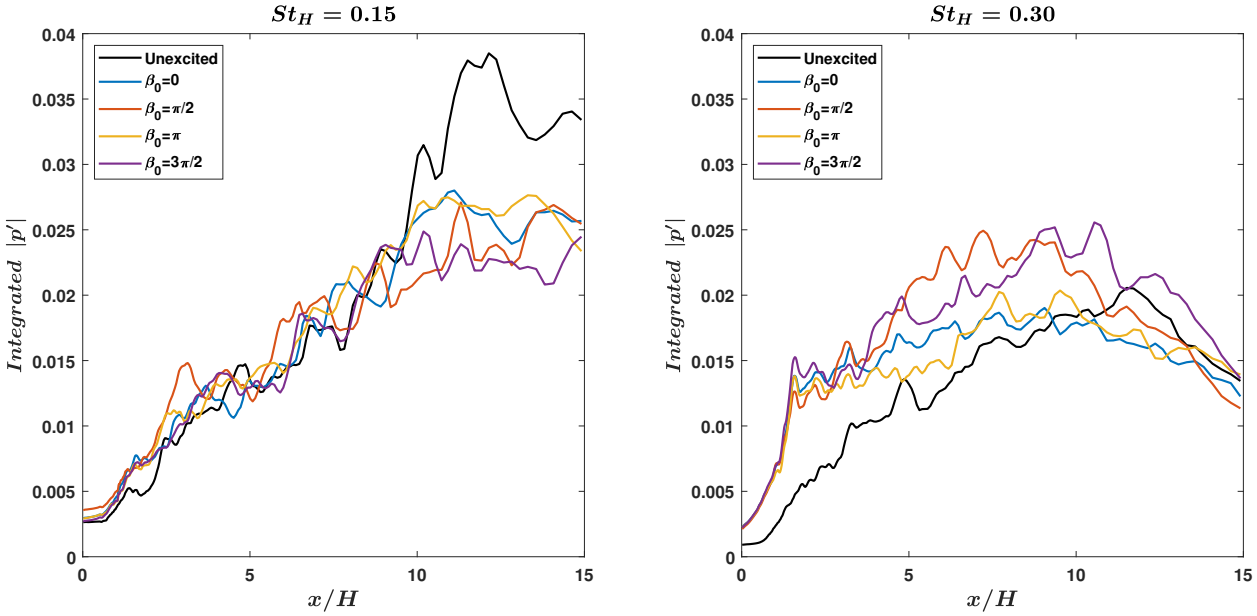

Figure 6.12 Integrated pressure comparing baseline and bi-modal excited cases; Strouhal numbers 0.15 (left) and 0.30 (right) are displayed.

Figures showing OASPL and $\Delta OASPL$ for the bi-modal cases are shown in Fig. 6.13 and 6.14 respectively. Like the case of single-mode excitation, peak noise reduction occurred primarily in the major plane of the jet for all bi-modal excitation cases. In the minor plane, phase lags of $\beta_0 = \pi$ and $\beta_0 = 3\pi/2$ increased the peak noise with $\beta_0 = 3\pi/2$ increasing the peak noise by around 1dB. However, these two phase lags see some noise reduction at

low polar angles between 25° and 35°. It was shown in Fig. 6.11 and 6.12 that $\beta_0 = 3\pi/2$ reduced Strouhal number 0.15 the most in the near field. This same phase lag generated the most reduction for directivity angles with Strouhal number 0.15 as the dominant frequency. This supports the claim that reducing the near field structures can reduce the far field noise. The other two phase lags, $\beta_0 = 0$ and $\beta_0 = \pi/2$, had little to no impact on the peak noise in the minor plane. Overall, the case of $\beta_0 = 0$ had the best noise reduction performance with minimal amplification in the minor plane and a reduction up to 1.8dB in the major plane for a wide range of emissivity angles. Ultimately for all cases, noise reduction is greatest in the major plane between polar angles of $\theta = 20° - 60°$. Figure 6.15 is additionally shown to more clearly show the noise reduction in this region.

Figures 6.16 and 6.17 show the peak emission far field spectra in the minor and major planes, respectively. In the minor plane, each case still sees an amplification around Strouhal number 0.15, which is likely a result of the actuation. However, there are stark contrasts between the cases around Strouhal number 0.30. Particularly for the case of $\beta_0 = 0$, there is a large reduction between Strouhal numbers 0.20 and 0.35, however, the amplification around Strouhal number 0.15 prevents the overall noise from being reduced. It is recalled from the near field analysis that this phase lag had some of the smallest amplification of Strouhal number 0.30. The major plane shows a similar trend where all cases reduced the noise around Strouhal number 0.25, but to varying degrees with $\beta_0 = 0$ performing the best.

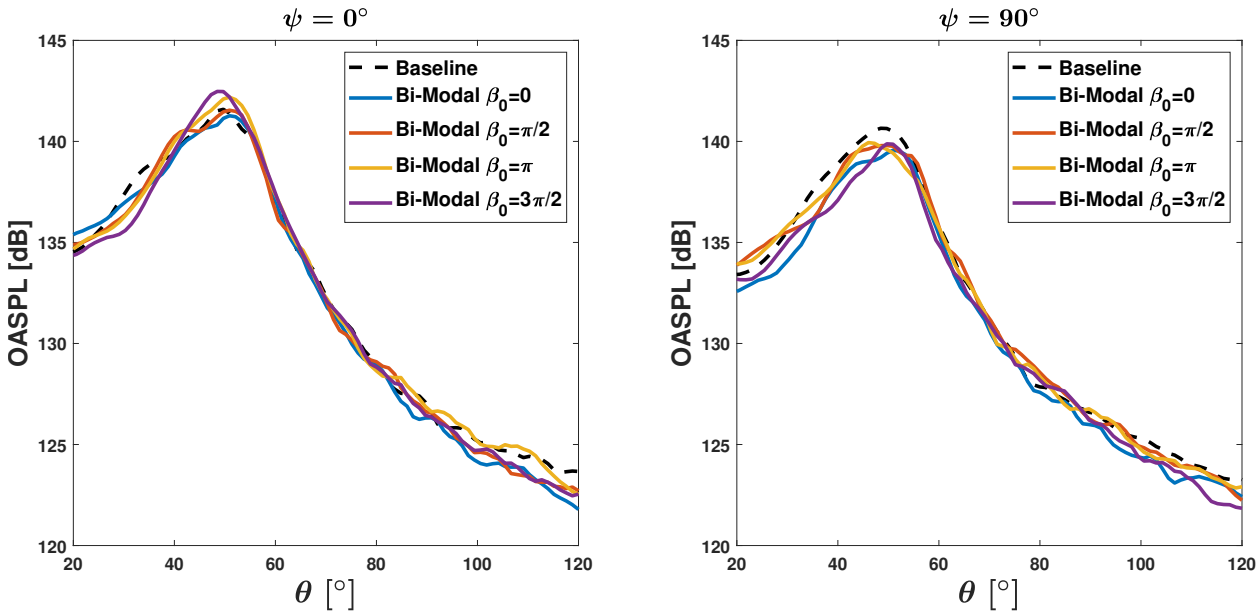

Figure 6.13 Minor (left) and major (right) plane OASPL comparison for bi-modal excitation cases.

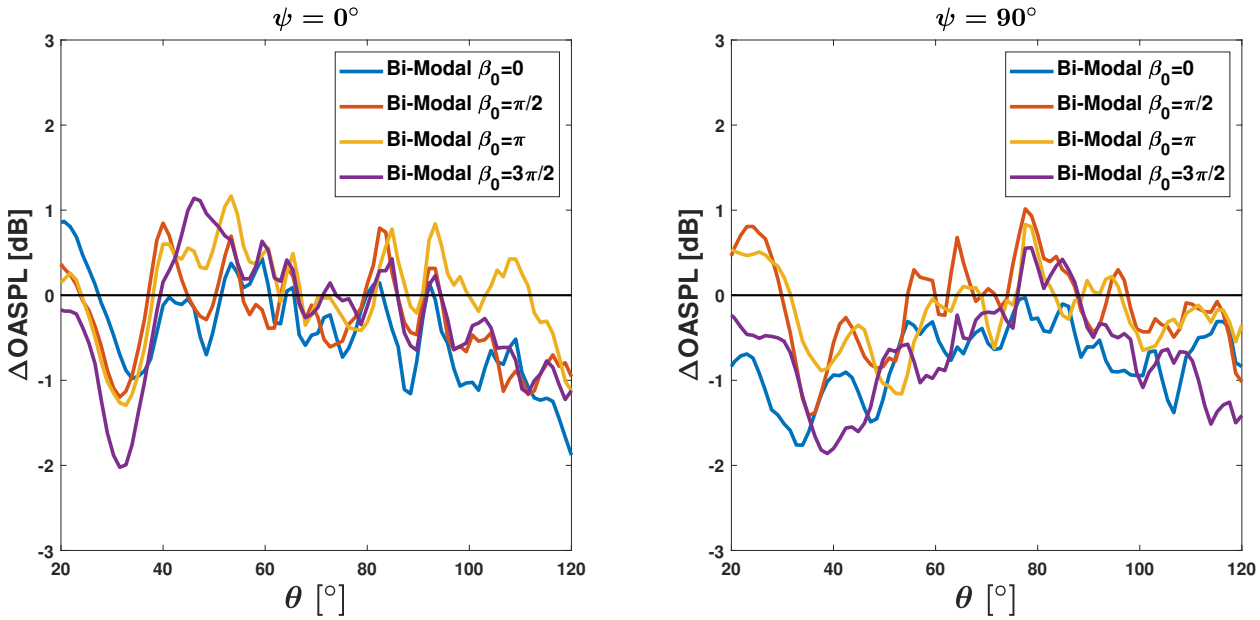

Figure 6.14 Minor (left) and major (right) plane $\Delta OASPL$ for bi-modal excitation cases; negative values indicate noise reduction.

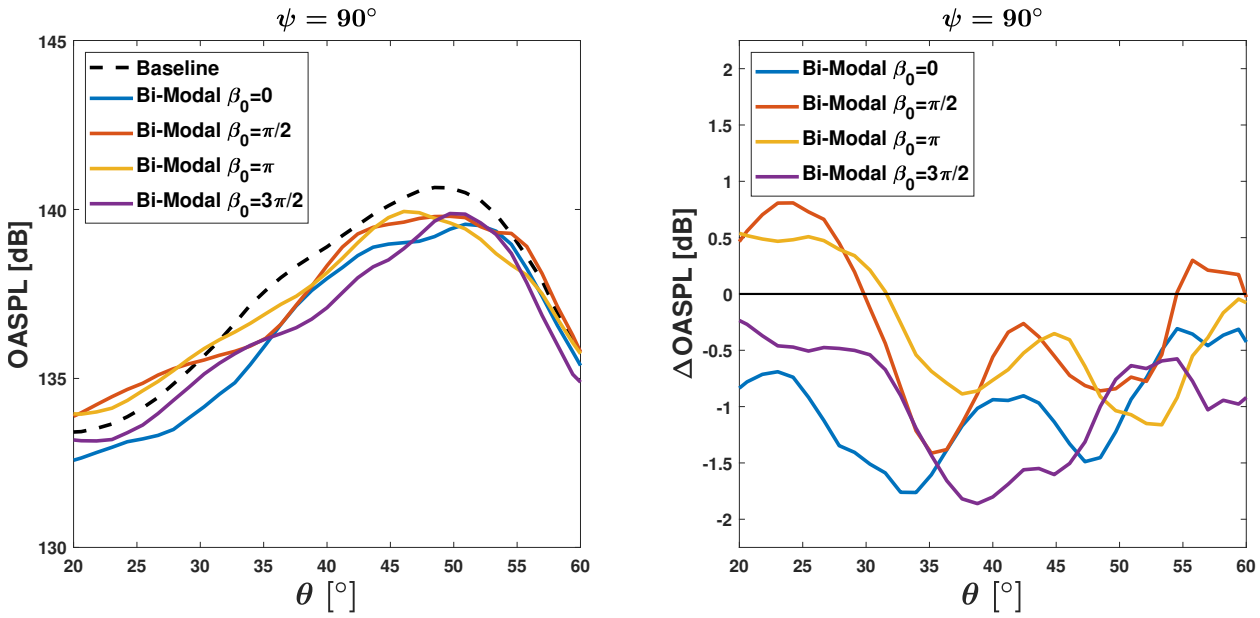

Figure 6.15 Zoomed $OASPL$ (left) and $\Delta OASPL$ (right) for major plane comparing bi-modal excited cases.

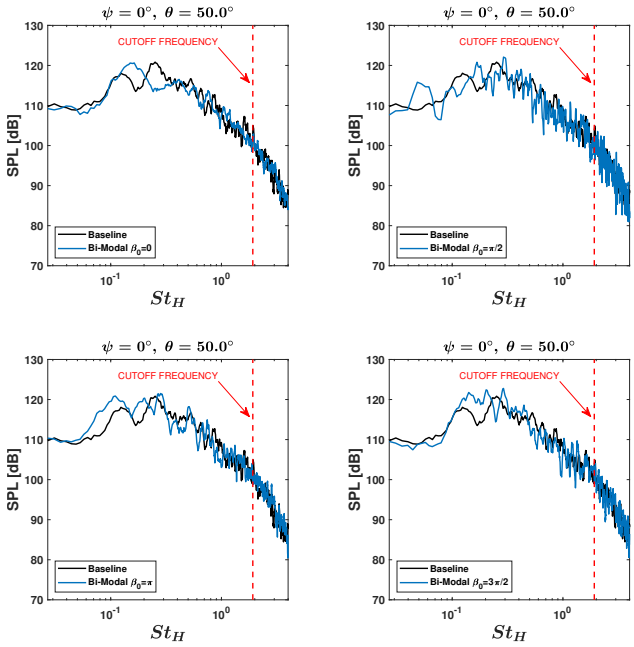

Figure 6.16 Far field spectra at peak emissivity angle in minor plane comparing bi-modal excited cases to baseline case.

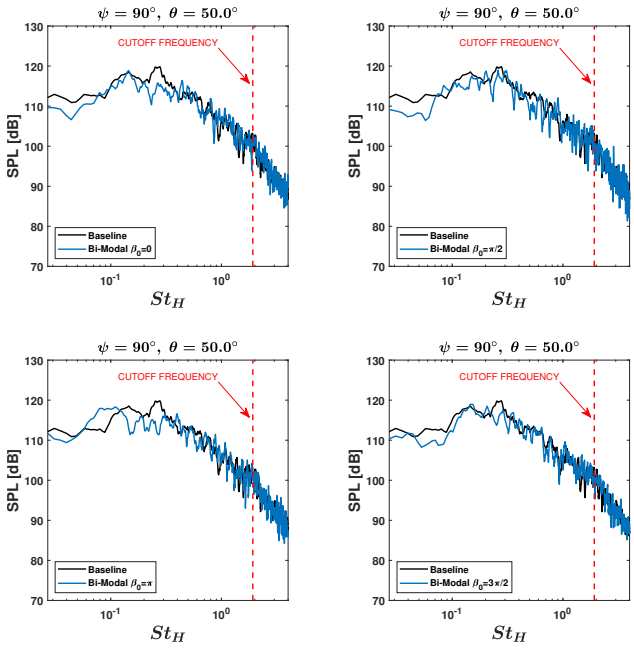

Figure 6.17 Far field spectra at peak emissivity angle in major plane comparing bi-modal excited cases to baseline case.

It was noted earlier that Strouhal number 0.15 is dominant at lower emission angles, where Fig. 6.14 shows reduction for all bi-modal cases in both planes. Looking at the spectra for $\theta = 35°$ in Figs. 6.18 and 6.19, there is a clear reduction of Strouhal number 0.15 for all cases, which results in an OASPL reduction for that emission angle. Again, there are varying levels of effectiveness with $\beta_0 = 0$ giving the most reduction of Strouhal number 0.15. The phase lag, $\beta_0 = 3\pi/2$, still exhibits an overall reduction, but there remains a prominent peak at Strouhal number 0.15.

The results for the bi-modal cases are a mix of the expected and unexpected. It has long been observed that the phase lag affects the interaction between noise sources [35, 51]. It was predicted by the ROM in Chapter 3 [56] that some phase lags would decrease the noise, while others would amplify it. This is seen when looking at both the minor and major plane noise. The phase lags of 0 and $\pi/2$ have the negligible changes on the peak noise in the minor plane and have the greatest reduction of the peak in the major plane. The other two phase lags, π and $3\pi/2$, amplify the peak noise in the minor plane and have the least peak reduction in the major plane.

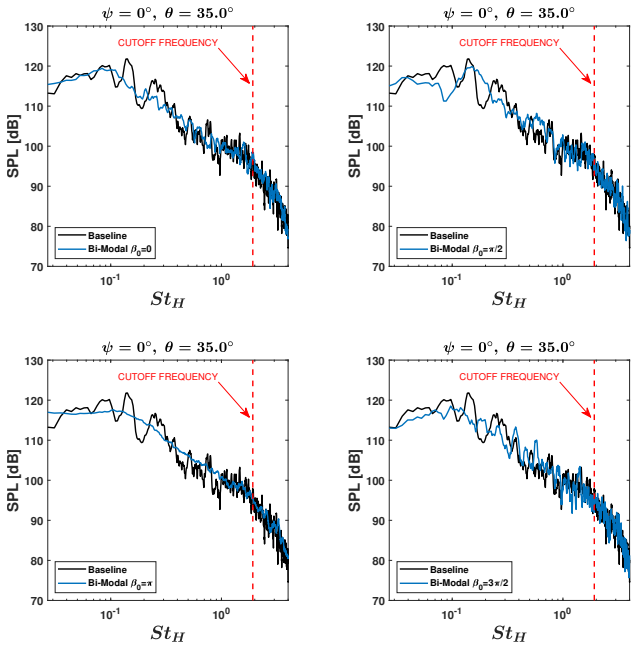

Figure 6.18 Far field spectra at peak emissivity angle in minor plane comparing bi-modal excited cases to baseline case.

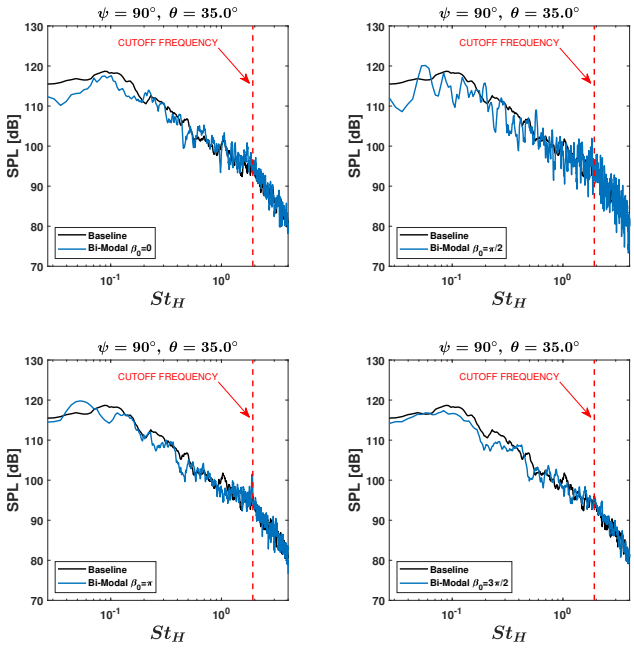

Figure 6.19 Far field spectra at peak emissivity angle in major plane comparing bi-modal excited cases to baseline case.

SPOD analysis is once again performed. Contours of the first and second mode are shown in Figs. 6.20 and 6.21 respectively. With the forcing amplitude being increased for

the bi-modal cases, the effects are more pronounced than for the single-mode cases. The actuation at Strouhal number 0.30 shows in the first mode for all bi-modal cases with the distinct symmetric structures. The streamwise amplification of 0.30 changes with the initial phase lag. The phase lag of $\beta_0 = 0$ has Strouhal number 0.30 peaking at $X/H = 10$ and $\beta_0 = \pi/2$ causes the peak to be at $X/H = 7$. The phase lag of $\beta_0 = \pi$, delays the peak to $X/H = 9$, and $\beta_0 = 3\pi/2$ doesn't show a distinct peak, but rather a broad amplification along the streamwise direction. Previous analysis by Salehian et al. [82] show the peak noise sources originate from $X/H = 7$ for the same jet at Strouhal number 0.15. Focusing on Strouhal number 0.15 in Fig. 6.20, it is observed that the coherent structures are weaker for the bi-modal cases of $\beta_0 = 0$ and $\beta_0 = 3\pi/2$, which also saw the most noise reduction at the lower emission angles where Strouhal number 0.15 is dominant.

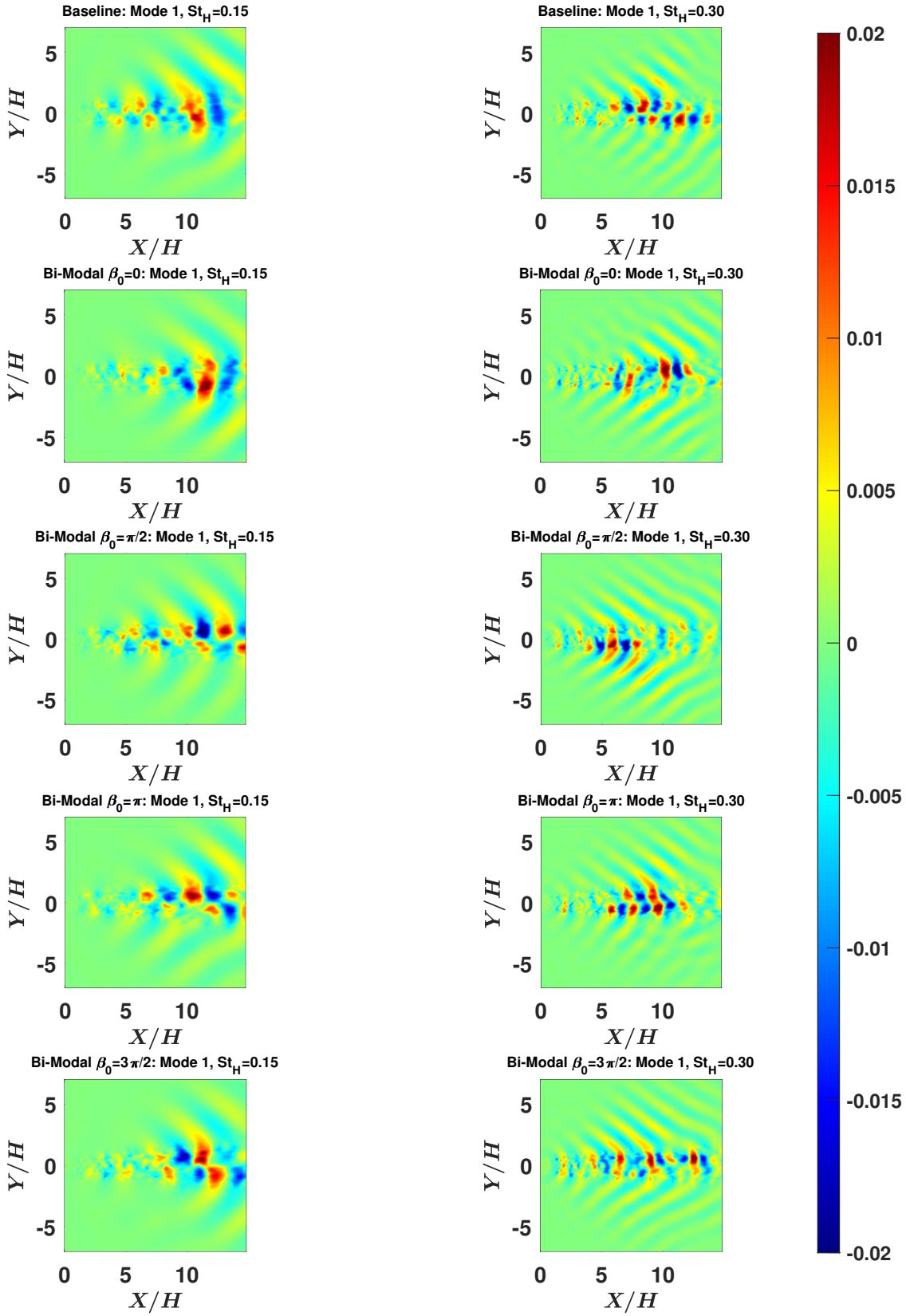

Figure 6.20 First mode SPOD contours comparing baseline and bi-modal excited cases; shown are Strouhal numbers 0.15 and 0.30.

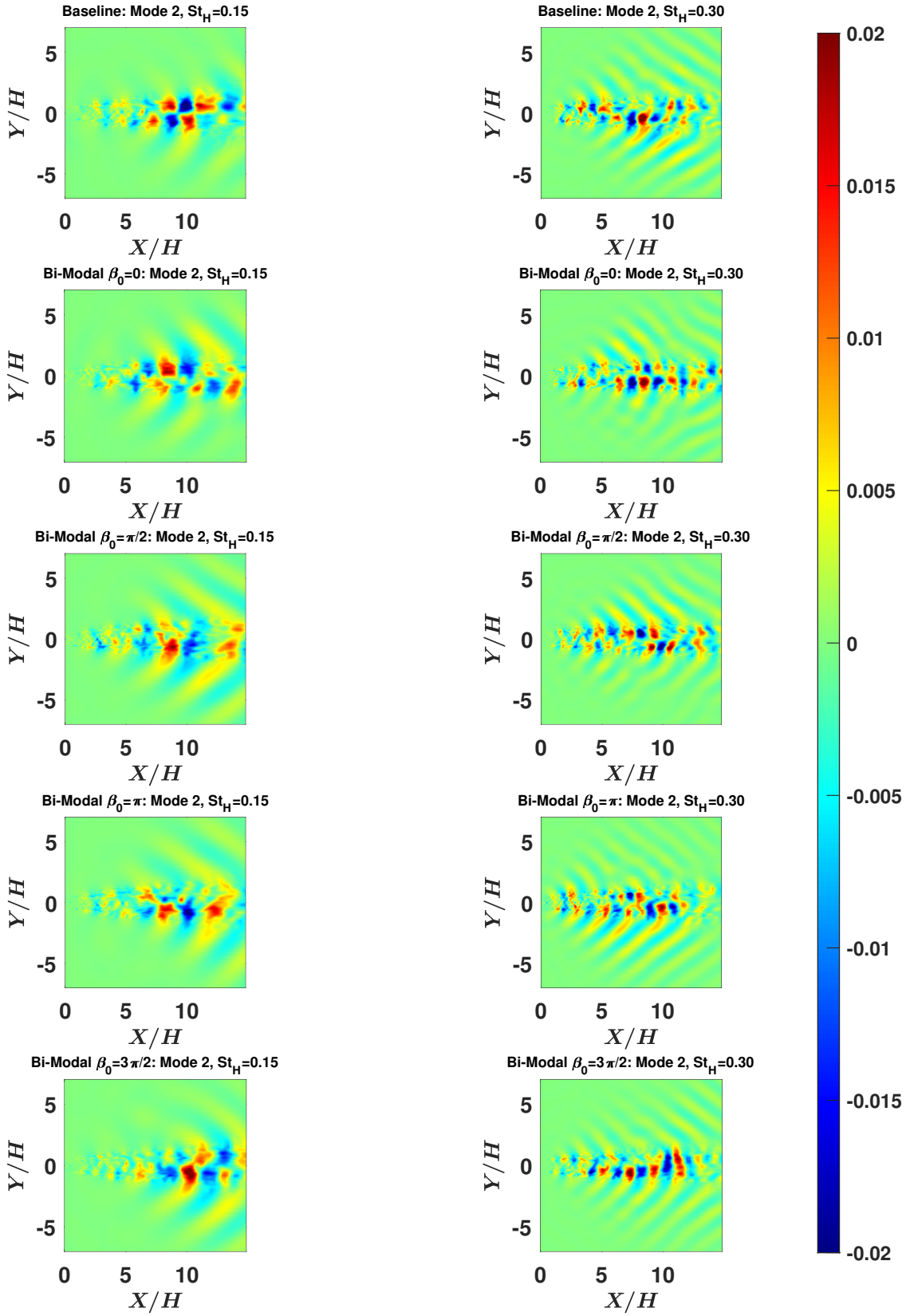

Figure 6.21 Second mode SPOD contours comparing baseline and bi-modal excited cases; shown are Strouhal numbers 0.15 and 0.30.

6.3 Conclusions from Bi-Modal Excitation

This work began by considering the large eddy simulation of an unexcited rectangular jet as a basis for analysis of bi-modal excitation to reduce the dominant frequency noise. Near field analysis revealed Strouhal number 0.15 as the most amplified. This Strouhal number appeared in the far field noise as the dominant peak for low emission angles between 32° and 46°. This mode also appeared as a secondary peak in the far field at the peak emission angle of 50°. Thus, Strouhal number 0.15 was taken as the fundamental that needed reduced. The ROM from Chapters 2 and 3 [56] predicted that fundamental-harmonic interactions can reduce the dominant coherent structure, which meant the addition of Strouhal number 0.30. This was introduced by exciting the jet with a small pressure fluctuation. The noise reduction mechanism is that Strouhal number 0.15 can be reduced by the amplification of Strouhal number 0.30. A case of single-mode excitation was first considered where only Strouhal number 0.30 was excited. A second set of cases was considered with bi-modal excitation, where both Strouhal numbers 0.15 and 0.30 were forced with different phase lags with respect to one another.

Both sets of excitation cases provide strong support for the theory presented in Chapters 2 and 3 [56]. Near field analysis showed that the fundamental, Strouhal number 0.15, could be reduced with the addition of the harmonic, 0.30. The underlying mechanism is that energy is transferred between the modes, which was shown by amplification of 0.30 as 0.15 was reduced. The initial phase lag between the two modes was shown to have an effect in the bi-modal cases, and greater reduction of Strouhal number 0.15 could be achieved depending on the phase lag. In the bi-modal cases, it is shown that the more amplified Strouhal number 0.30 gets, the greater 0.15 gets reduced, further supporting the theory energy exchange between the two modes. Both excitation methods were ultimately able to reduce the far field noise in the major plane of the jet by around 1dB, with bi-modal excitation giving the greatest reduction for an initial phase lag of $\beta_0 = 0$. In the minor plane, the peak noise was not significantly reduced and was even amplified with bi-modal excitation for $\beta_0 = 3\pi/2$. At

lower emission angles in the minor plane where Strouhal number 0.15 was dominant, there was reduction for all cases. Investigation of those spectra showed a reduction at Strouhal number 0.15. It is ultimately concluded that the noise-causing coherent structures can be targeted and reduced by exciting with harmonics. The reduction of the targeted structure can reduce the far field noise. Forcing interaction between the fundamental and harmonic with bi-modal excitation can be more effective than single-mode, given a favorable phase lag between the two.

7 Noise Reduction via Feed-Forward Control

As mentioned in Sec. 1.4, the use of controls that use real time sensor measurements for jet noise reduction are very limited. A first principles approach is taken to reduce the noise. It is well established that the large-scale turbulent structures (LSS) in the jet are the dominant noise sources and the LSS can be characterized as waves of various frequencies and spanwise wave numbers [45, 52]. The controller in this work is designed to utilize pure cancellation via out of phase waves to reduce the noise. Noise production is ultimately a nonlinear process, but there exists a region in the initial shear layer in the jet where large-scale structures behave linearly [84]. Along the upper and lower nozzle lips, sensor-actuator pairs are placed across the span of the jet with the sensors upstream of the actuators. Sensor-actuator pairs can be visualized in Fig. 7.1. There are 4 sets of sensor-actuator pairs on both the upper and lower nozzle surfaces, giving 8 pairs in total. At every iteration in the code, the sensors read the boundary layer pressure perturbation (i.e. $p' = p - \bar{p}$). Each set operates independently to account for spanwise variation in the sensed disturbance. The actuator then responds with:

$$p_{act} = \bar{p} - K_p \times p' \tag{7.1}$$

Above, K_p is a proportional gain, which is a tuning parameter investigated in Sec. 7.1. The meaning of Eq. 7.1 is that the actuators respond with the exact same signal as is being read by the sensor. The negative sign on K_p makes the actuator signal 180° out of phase from the sensor signal and then K_p scales the actuator response. In this work, proportional gains are limited to 0.5, 1.0, and 1.5. Ideally, the $K_p = 1.0$ case should perfectly cancel the turbulent fluctuations exiting the nozzle and achieve the greatest noise reduction. It is expected that the $K_p = 0.5$ case will cancel half of the disturbance. The $K_p = 1.5$ case is overcompensating for the sensed disturbance by a factor of 50%, thus it should fully cancel the disturbance plus introducing a fluctuation at half the amplitude of the sensed disturbance, but 180° out of phase. It is ultimately expected that this case will perform similarly to the $K_p = 0.5$ case.

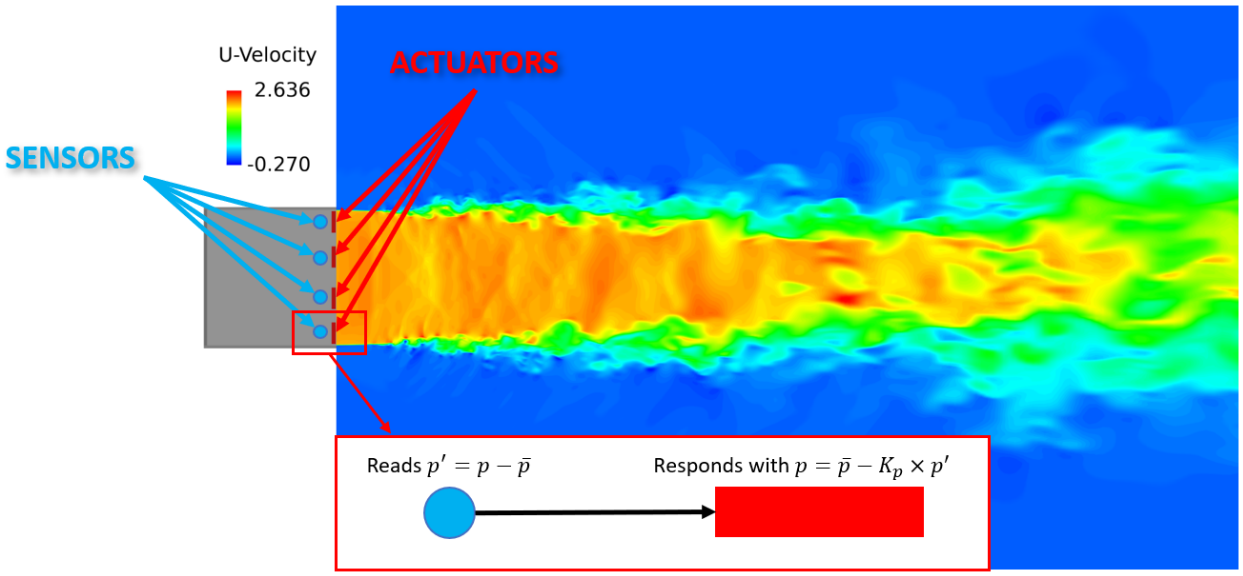

Figure 7.1 Schematic of feed-forward controller.

Since the sensors are located upstream of the actuators and the bulk flow is supersonic, the sensors should not feel the effects of the actuators. The outflow region downstream of the nozzle is considered as the system that is being controlled. The disturbances that amplify in the shear layers of the jet begin as boundary layer disturbances inside of the nozzle. This downstream amplification is spatial and temporal and is very difficult to make a dynamics model for. In the case of this controller, the downstream system response is not accounted for in the actuation prescription, so it is inappropriate to classify this controller as closed-loop. Rather, this controller is using a sensed disturbance that affects the system and then using the input from the actuation to negate some of their impact on the system. Thus, it would be more appropriate to classify this controller as feed-forward.

A rule of thumb for wave cancellation to be effective, the sensor-actuator pairs should be spaced within a quarter wavelength of one another. It was established in Chapter 5 [82] that Strouhal number 0.15 was the dominant fluctuating component at the nozzle exit. Using the local speed of sound at the nozzle exit, this gives a maximum sensor-actuator spacing of approximately $1H$ for cancelling up to Strouhal number 0.15. However, it was later shown that Strouhal number 0.25 peaks in the far field at the peak directivity angle [85].

The implemented spacing in this work is $0.11H$, which gives a maximum cancelled Strouhal number of 1.45 using the quarter wavelength criteria. It should be noted that effectively all frequencies are being excited with this controller configuration, but it should not be expected that the controller has the same impact on all frequencies.

7.1 Results with Positive Gain

Results are now presented. Considered first are the cases with positive gain values of 0.5, 1.0, and 1.5. Per Eq. 7.1, these should create cancelling waves that lead to a noise reduction. Included additionally are the results from single-mode excitation from Sec. 6.1 [85]. This additional comparison case is more aligned with the previous literature on excitation where excitation is prescribed at a single time-period mode. This is to show if the feed-forward controller can improve on more traditional excitation approaches. In this previously published case, the jet was excited at Strouhal number 0.30 using pressure at an amplitude of $0.004\bar{p}$, which was the fluctuation amplitude of Strouhal number 0.15 from the baseline case. Strouhal number here is defined using the jet height and exit velocity (i.e. $St_H = fH/U_j$). Actuators for this case were located on the upper and lower nozzle surfaces across the entire jet width. Both upper and lower actuators operated in-phase with each other. For the feed-forward cases, the proportional gain constant ranges from 0.5 to 1.5, which puts the feed-forward excitation amplitude about an order of magnitude smaller the single-mode case. The excitation amplitude used for the single-mode case is already small compared to that of other publications [25, 38, 44]. An example of the actuation signal for $K_p = 1.0$ is shown in Fig. 7.2 with comparison to the single-mode actuation. Exhibited is that the feed-forward signal is significantly more complex, being composed of several frequencies. Another difference is that while the phase of the single-mode case is clearly fixed, the phase of the different frequencies in the feed-forward cases can be variable with time in accordance with what is sensed.

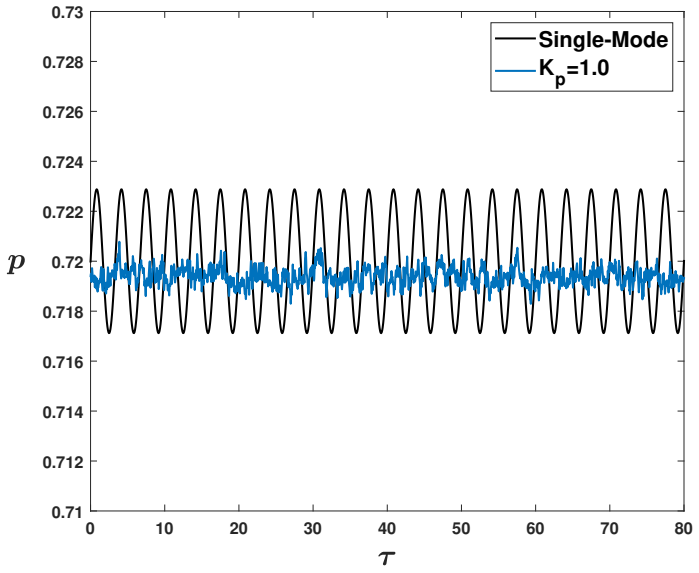

Figure 7.2 Time signal of single-mode and feed-forward excitation.

7.1.1 Near Field Analysis

The feed-forward controller is exciting the jet at all frequencies, hence the results will begin by discussing turbulent statistics before delving into frequency-based analysis. Figure 7.3 displays near field contours of p'_{RMS}. This figure clearly shows the strong fluctuations in the initial region of the upper and lower shear layers. Some interesting flow features are shown here. In the baseline case, there is a weak fluctuation before the first shock cell at $X/H = 1.2$. The case of feed-forward control with $K_p = 0.5$ maintained this fluctuation, however the higher gain cases and the single-mode case removed this fluctuation. Qualitatively, it appears that the initial p'_{RMS} is reduced for all feed-forward cases and increased for the single-mode case.

Figure 7.4 shows the difference in p'_{RMS} for all excited cases with negative values indicating reduction. Immediately it is evident that feed-forward cases are having a different near field impact compared to the single-mode case. In the initial shear layer leaving the nozzle, all feed-forward cases reduce the magnitude of the pressure fluctuations, whereas the single-mode case actually increases them. Another distinct effect of the feed-forward control is the symmetry of the $\Delta p'_{RMS}$ near the jet exit. The naturally present disturbances are composed of various azimuthal modes that are not all symmetric [27]. For the single-mode

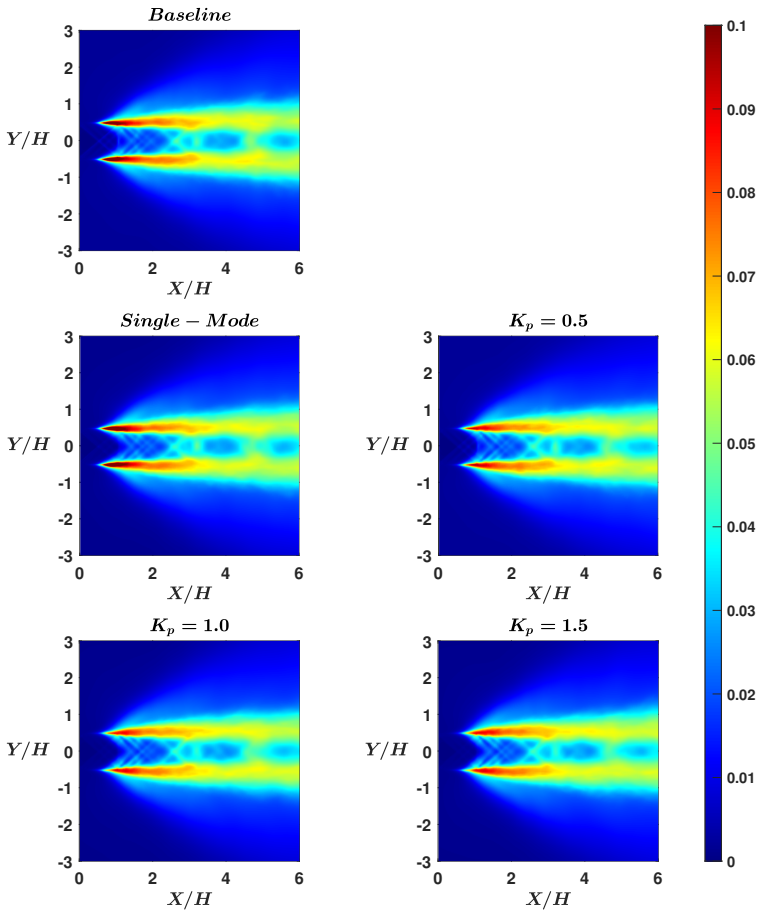

Figure 7.3 Contours of p'_{RMS} comparing baseline, single-mode, and feed-forward cases.

comparison case, both upper and lower actuators operated in-phase, so if the natural disturbances are asymmetric, then the superposition of those waves near the nozzle exit should be asymmetric, leading to asymmetry in the $\Delta p'_{RMS}$. Contrast this with the feed-forward controller that has all actuators operating independently of one another. Despite the phase of the naturally present disturbance, the same level of superimposed pressure fluctuations are present in the upper and lower shear layers.

The greatest reduction in the initial shear layer fluctuation is achieved by the $K_p = 1.5$ case with a maximum of 68% reduction. Not far behind is the $K_p = 1.0$ case with a maximum reduction of 61%. Ideally, the $K_p = 1.0$ case should cancel all fluctuations, but this is clearly not the case. Even though the fluctuations are reduced in the near nozzle shear layer, it doesn't necessarily create an overall reduction downstream as is shown in Fig. 7.4.

It is shown that downstream, the $K_p = 1.0$ case qualitatively shows the greatest near field reduction. Clearly, there are other mechanisms involved downstream aside from cancelling waves. Since this controller is trying to utilize cancelling waves at the nozzle exit, there likely exists a maximum reduction that can be attained using this approach with a proportional gain value in the vicinity of 1.0.

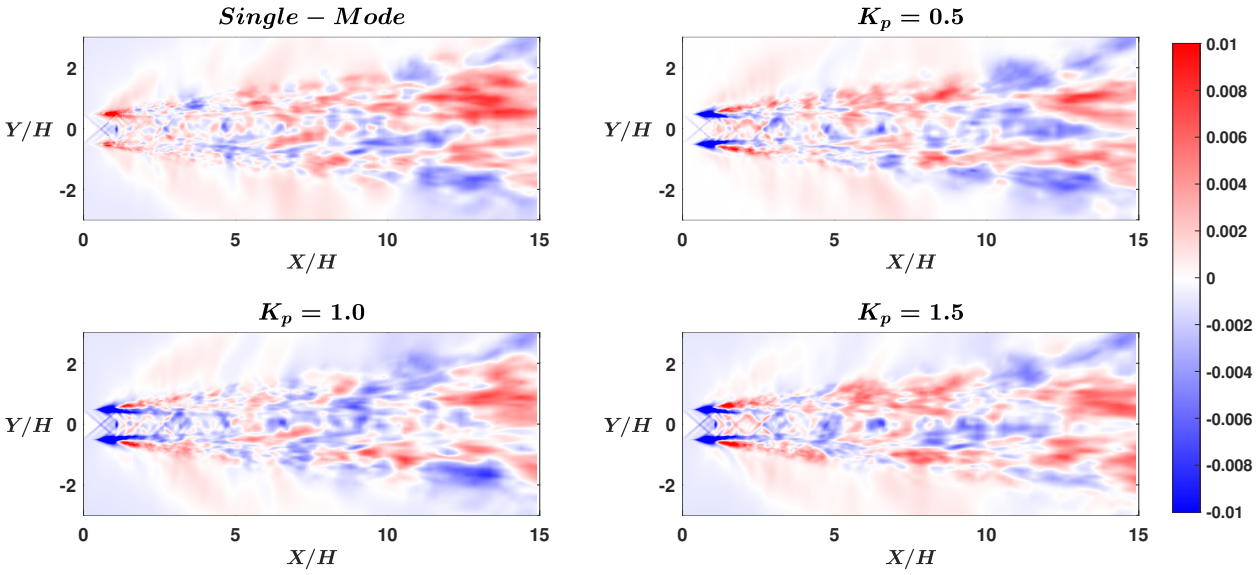

Figure 7.4 Contours of $\Delta p'_{RMS}$ comparing single-mode, and feed-forward cases; negative values indicate reduction.

Near field spectra in the initial shear layer are shown in Fig. 7.5. Shown is a reduction in the peak Strouhal number of 0.15, which was shown to be the dominant noise component at low emissivity angles [85]. The greatest reduction again is shown by $K_p = 1.0$. At the streamwise location of $X/H = 0.4$, some high frequency components emerge above Strouhal number 1.0, which is also reduced by the feed-forward controller. This reduction is not exhibited by the single-mode case. Further downstream, the spectra becomes very noisy and it is difficult to distinguish differences in the spectra. To rectify this, an integrated pressure is used. Contours of the minor plane are first FFT'd and the resultant pressure magnitudes are integrated in the y-direction for each Strouhal number. This was done earlier in Secs. 6.1-6.2 and expressed in Eq. 6.3.

The integrated pressures are plotted in Fig. 7.6 for Strouhal numbers ranging from 0.10

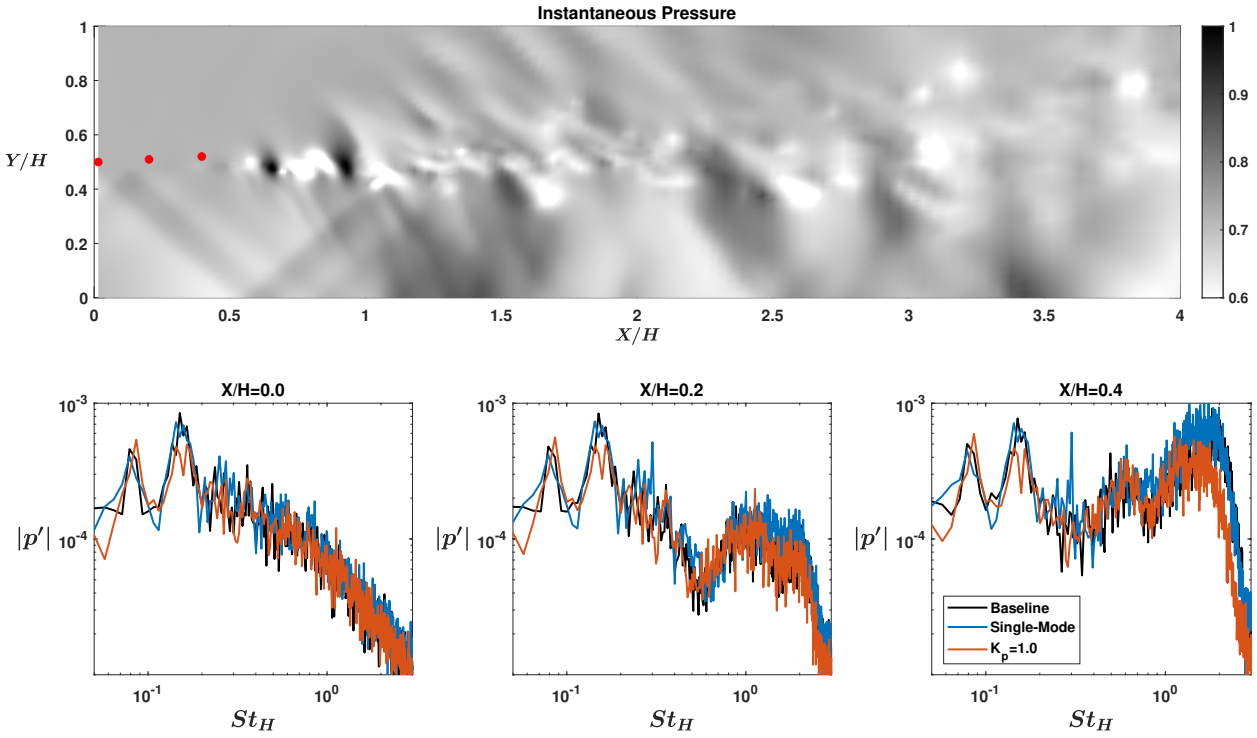

Figure 7.5 Instantaneous pressure showing probe locations (top); spectra at probes (bottom).

to 0.35, which is the range of interest for the peak radiated noise. It is clear that for some Strouhal numbers, the integration is reduced with the excitation and for others it is reduced. The peak near field frequency, Strouhal number 0.15 is reduced for all cases. The cases of $K_p = 0.5$ and $K_p = 1.5$ performed similarly for this Strouhal number, but did not decrease it more than the single-mode case. However, the $K_p = 1.0$ case did achieve some greater near field reduction. It was noted by Malczewski et al. [85] that Strouhal number 0.25 is the peak frequency at the peak directivity angle. This frequency is reduced for all cases with $K_p = 0.5$ yielding the greatest reduction. The case with $K_p = 1.0$ also reduces this Strouhal number, most notably at $X/H = 10$. For Strouhal number 0.30, all feed-forward cases reduced the peak. The single-mode case increased that frequency, but that is not surprising since that was the excitation frequency. In general, all feed-forward cases are shown to reduce the near field fluctuations in the Strouhal number range of interest. The case of $K_p = 1.0$ has the most consistent performance and reduces the near field signature more than the single-mode

case for all Strouhal numbers.

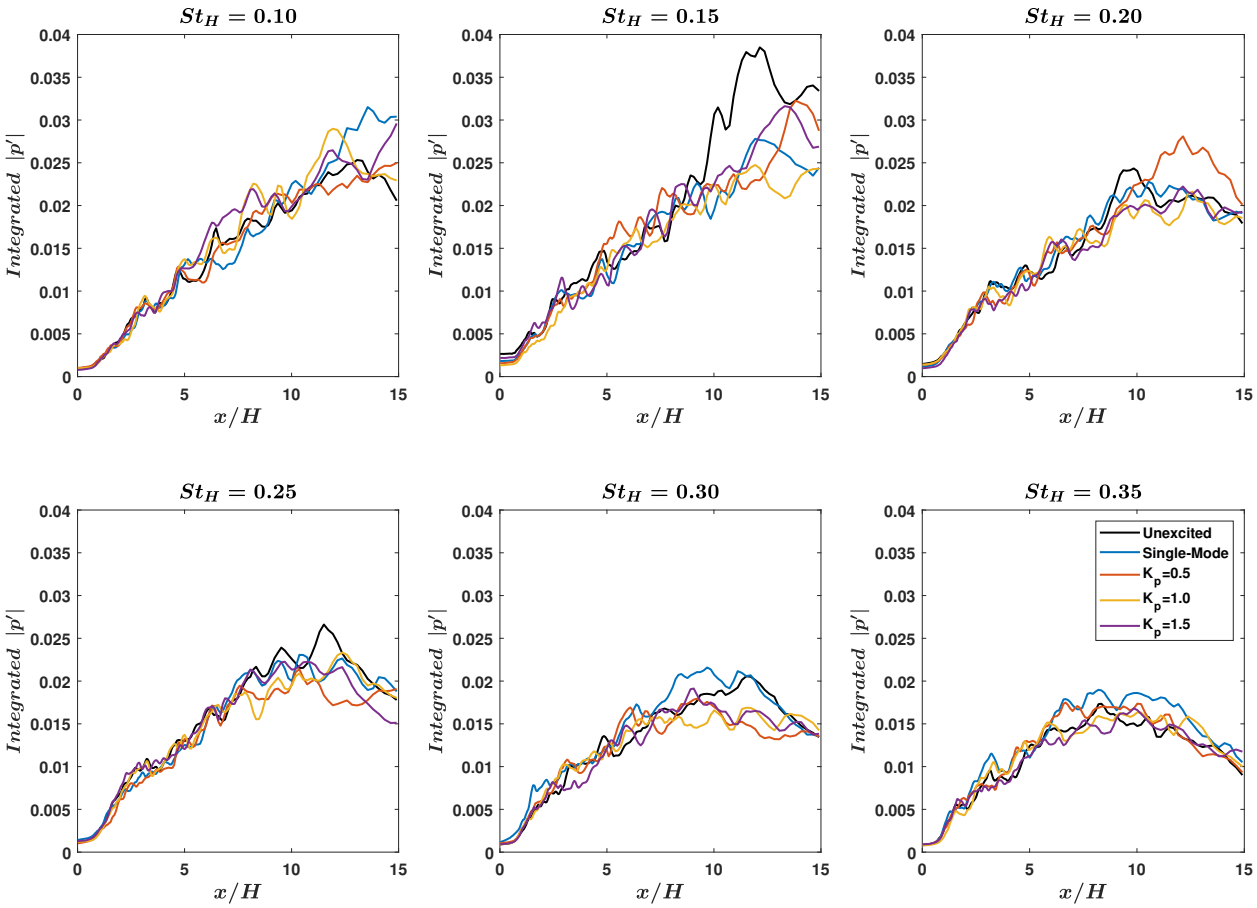

Figure 7.6 Contours of integrated pressure at various Strouhal numbers.

7.1.2 Far Field Analysis

Far field analysis begins by looking at overall sound pressure level (OASPL). This is shown in Fig. 7.7 along with the $\Delta OASPL$. In the minor plane, the peak noise is reduced for the feed-forward cases of $K_p = 0.5$ and $K_p = 1.0$ by about 0.5dB. The case with $K_p = 1.5$ did not reduce the peak noise. Looking at $\Delta OASPL$, the feed forward case of $K_p = 1.0$ reduces the noise by up to 2dB for a range of directivity angles between $\theta = 20° - 50°$. Comparing to the single-mode case, the case of $K_p = 1.0$ is a significant improvement in minor plane noise reduction. It is noted that the other feed-forward cases performed similarly to the single-mode case in the minor plane. While these cases still see some noise reduction, it is less than that of $K_p = 1.0$.

In the major plane, it is not expected that the feed-forward cases would perform much differently from the single-mode case because actuators are not placed on the side-nozzle surfaces. The OASPL results confirm this. For all cases, there is a around a 1dB of peak-to-peak noise reduction. The $\Delta OASPL$ plot tells a similar story for all excited cases; that is, there is a general noise reduction of around 1dB for all directivity angles around the peak. The general trend of $\Delta OASPL$ is the same for all excited cases. However, the case of $K_p = 1.5$ did not reduce the peak-to-peak noise as much and under performs the single-mode case.

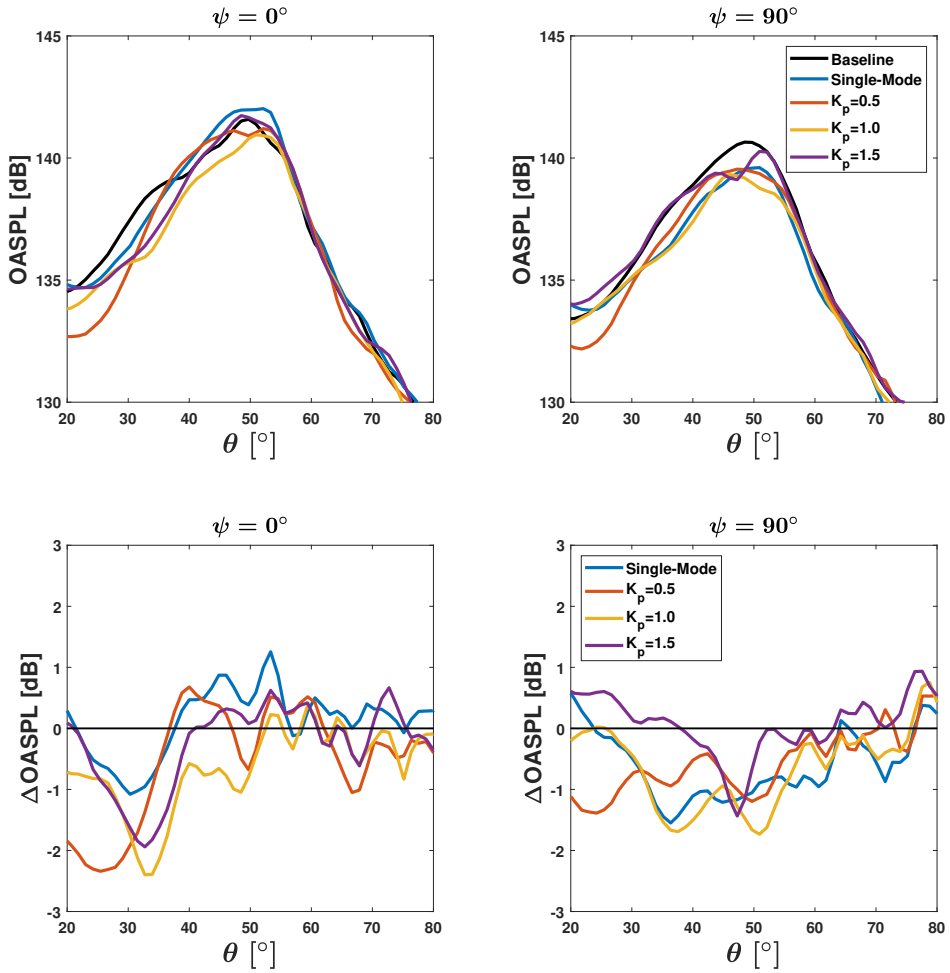

Figure 7.7 $OASPL$ (top) and $\Delta OASPL$ (bottom) for all cases in the minor plane (left) and major plane (right).

Figure 7.8 shows the minor plane spectra at the peak directivity angle of $\theta = 50°$ from

the baseline case. It is recalled from Fig. 7.8 that only the cases of $K_p = 0.5$ and $K_p = 1.0$ resulted in an OASPL reduction at this directivity angle. The case of $K_p = 0.5$ generated some reduction at around the peak of Strouhal number 0.25, but also increased the SPL slightly at Strouhal number 0.15. The case of $K_p = 1.0$ is the most interesting because the spectra follows the baseline case closely, but is slightly shifted downward for both peaks at Strouhal numbers 0.15 and 0.25. The final feed-forward case of $K_p = 1.5$ did not significantly reduce any part of the spectra. With he exception of $K_p = 1.5$, the feed-forward cases reduced parts of the spectra. In contrast, the single-mode excitation case was not able to notably reduce the SPL at any Strouhal numbers for this directivity angle, though it should be noted that the single-mode case was attempting to target specific Strouhal numbers, which it was able to successfully reduce at lower directivity angles [85, 86].

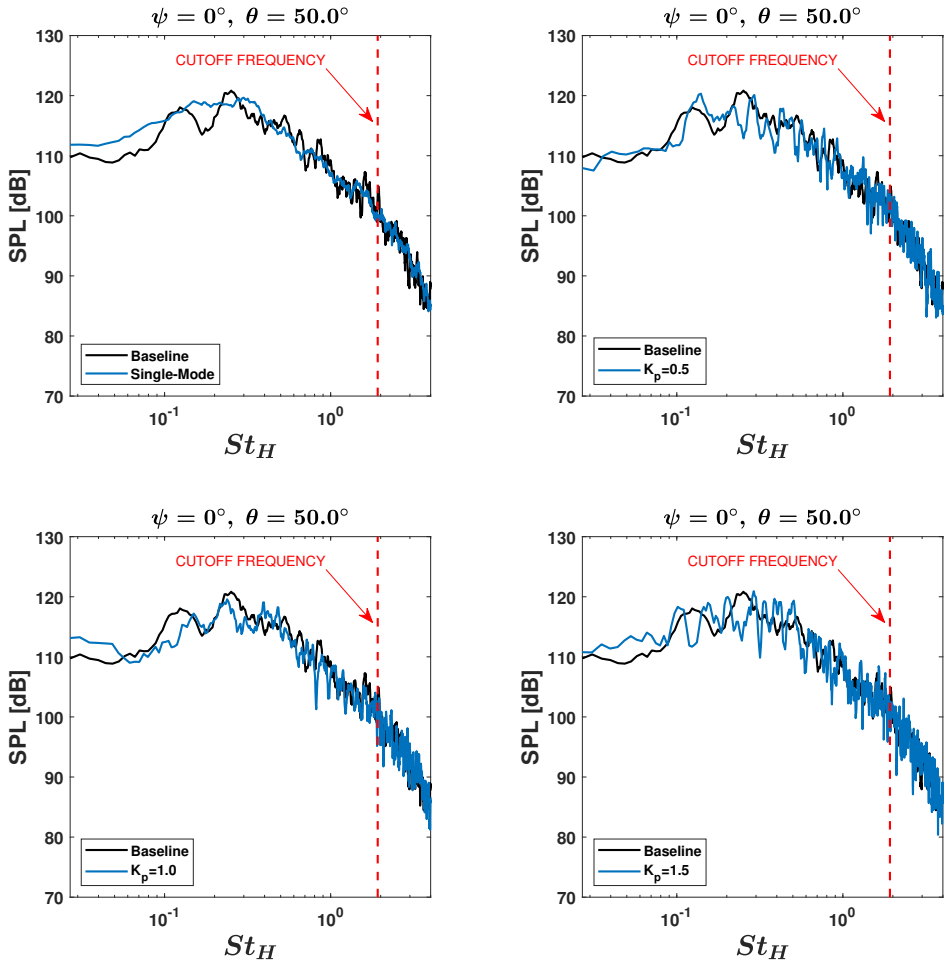

Figure 7.8 SPL spectra in the minor plane at the peak directivity angle for all cases.

Spectra for the major plane at the peak directivity angle are shown in Fig. 7.9. All cases here exhibit some SPL reduction at Strouhal number 0.25, and all cases reduced the peak noise here up to 1dB. The case of $K_p = 1.0$ has the most significant spectra reduction between Strouhal numbers 0.10 and 0.40, which is not attained with any other cases. At this directivity angle, both $K_p = 0.5$ and $K_p = 1.5$ had similar performance. Both show some reduction around Strouhal number 0.25, but it is not as significant as the single-mode or $K_p = 1.0$ case.

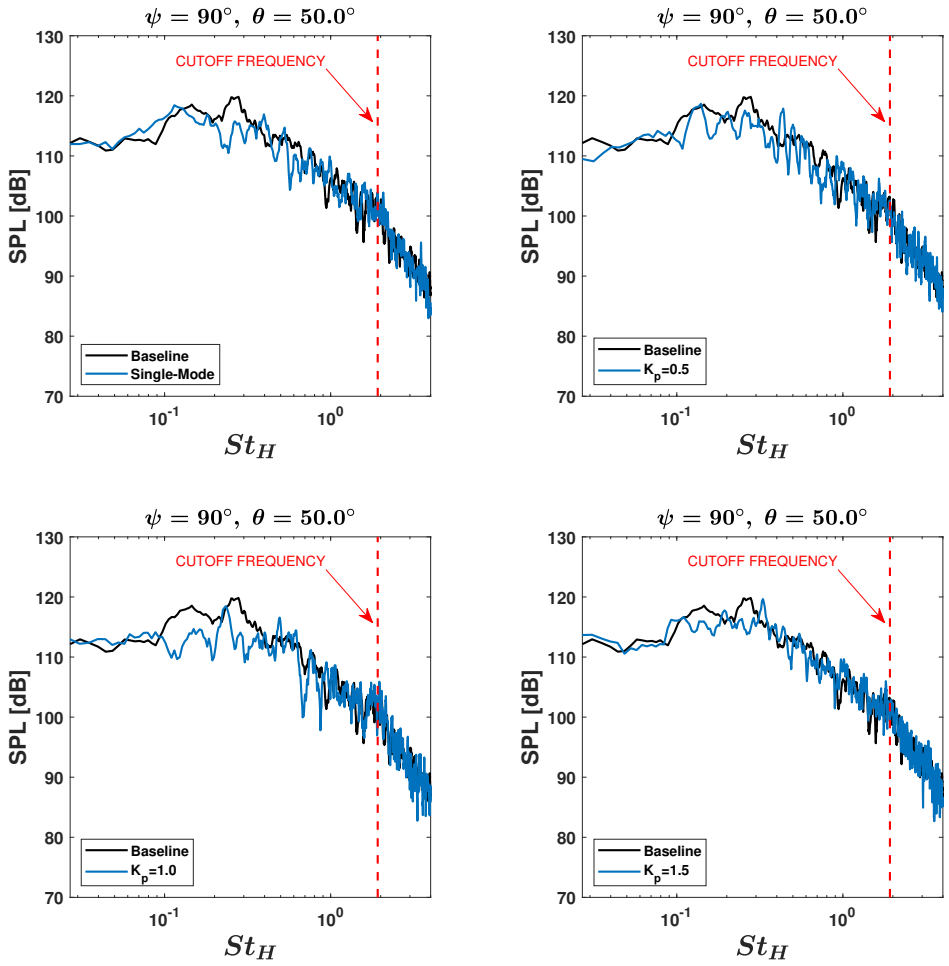

Figure 7.9 SPL spectra in the major plane at the peak directivity angle for all cases.

7.1.3 SPOD Analysis

Spectral Proper Orthogonal Decomposition (SPOD) is once again used to better visualize wave packets in the jet [83]. This can give further insight as to how the controller impacts

various spatial modes and how it differs from the single-mode excitation. As was shown in Sec. 5.1, Strouhal numbers 0.15 and 0.25 are the dominant noise components for which focus will be narrowed around.

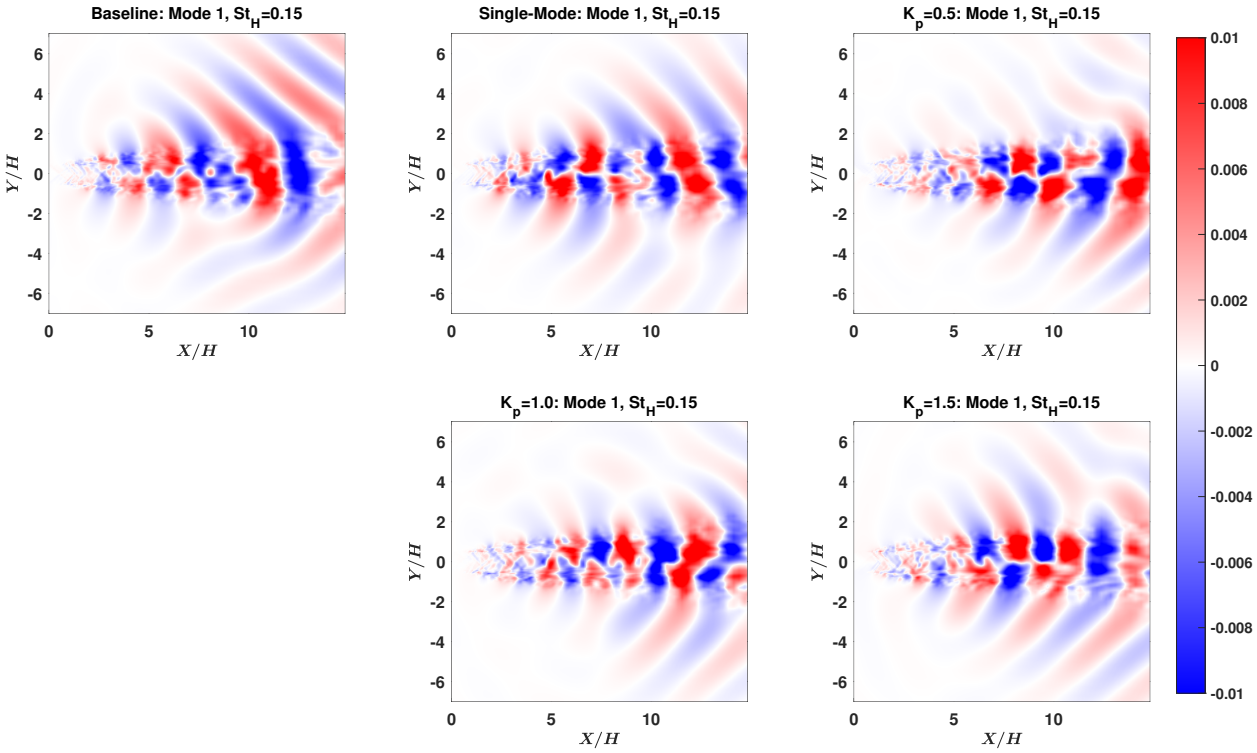

Figure 7.10 First mode SPOD shapes at Strouhal number 0.15 for positive gain cases.

The first and second SPOD modes for Strouhal number 0.15 are displayed in Figs. 7.10 and 7.11, respectively. It was noted by Malczewski et al. [86] that the single-mode excitation impacted the second SPOD mode more than the first. Figure 7.10 shows that the feed-forward controller has significant impact on first mode, especially for gains of 0.5 and 1.0. This is despite the fact that the actuation for the feed-forward controller has significantly lower input energy compared to the single-mode case. For these two cases, the radiating waves are significantly reduced. Visually, it is shown that the coherence in the turbulent structures are more broken down in the initial region up to $X/H = 5$. Further downstream, the structures develop a similar shape to the baseline jet, but with reduced radiating waves. In the second mode, the feed-forward cases have less impact and even exhibit some amplification of the radiating waves. But since the second mode is an order of magnitude smaller

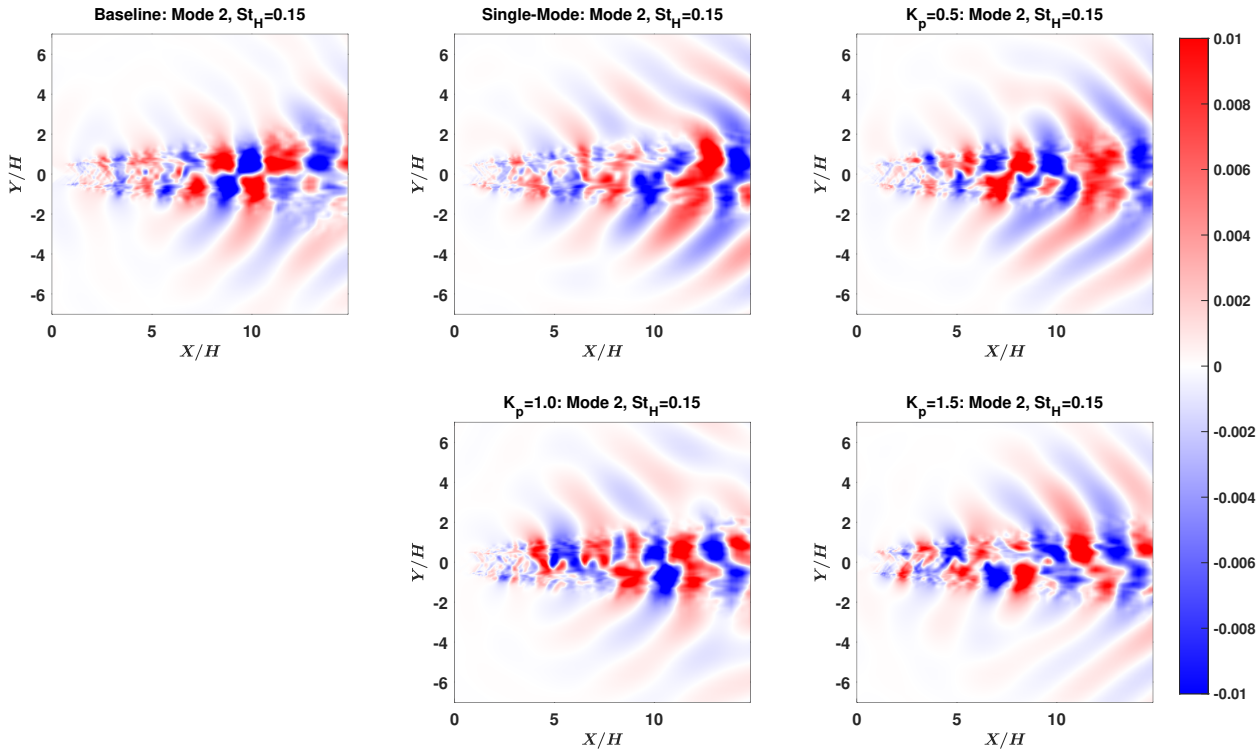

Figure 7.11 Second mode SPOD shapes at Strouhal number 0.15 for positive gain cases.

than the first mode, this doesn't create an increase in the noise since the first mode was significantly reduced.

Strouhal number 0.25 was shown as the dominant frequency at the peak directivity angle in both planes. The first and second SPOD modes are displayed in Figs. 7.12 and 7.13, respectively. Again in the first mode, there is a reduction of the radiating waves for gains of 0.5 and 1.0. For these two cases, the wave packets maintain a similar symmetric shape from the baseline case, but reduced. For the gain value of 1.5, the first mode does not appear as reduced and the wave packets take on an asymmetric structure. The location of the radiating waves is also significantly impacted for this gain value; the strong waves begin radiating around $X/H = 5$ and stop radiating around $X/H = 13$. Compare this to the baseline case where the strong waves begin radiating at $X/H = 8$. Comparing again to the single-mode case, the feed-forward controller has a greater impact on this first mode. Moving to the second mode, the feed-forward controller does not have much impact on the radiating waves, but does significantly impact the wave packet structure. For the case of $K_p = 0.5$,

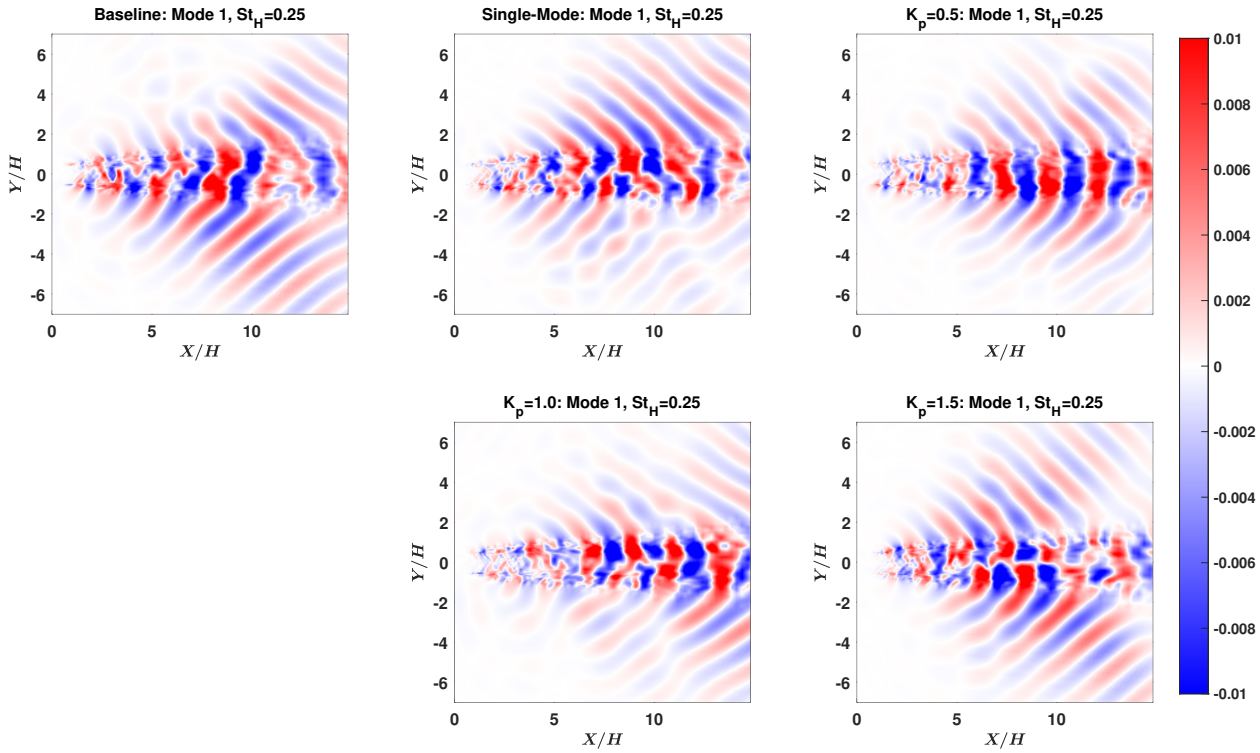

Figure 7.12 First mode SPOD shapes at Strouhal number 0.25 for positive gain cases.

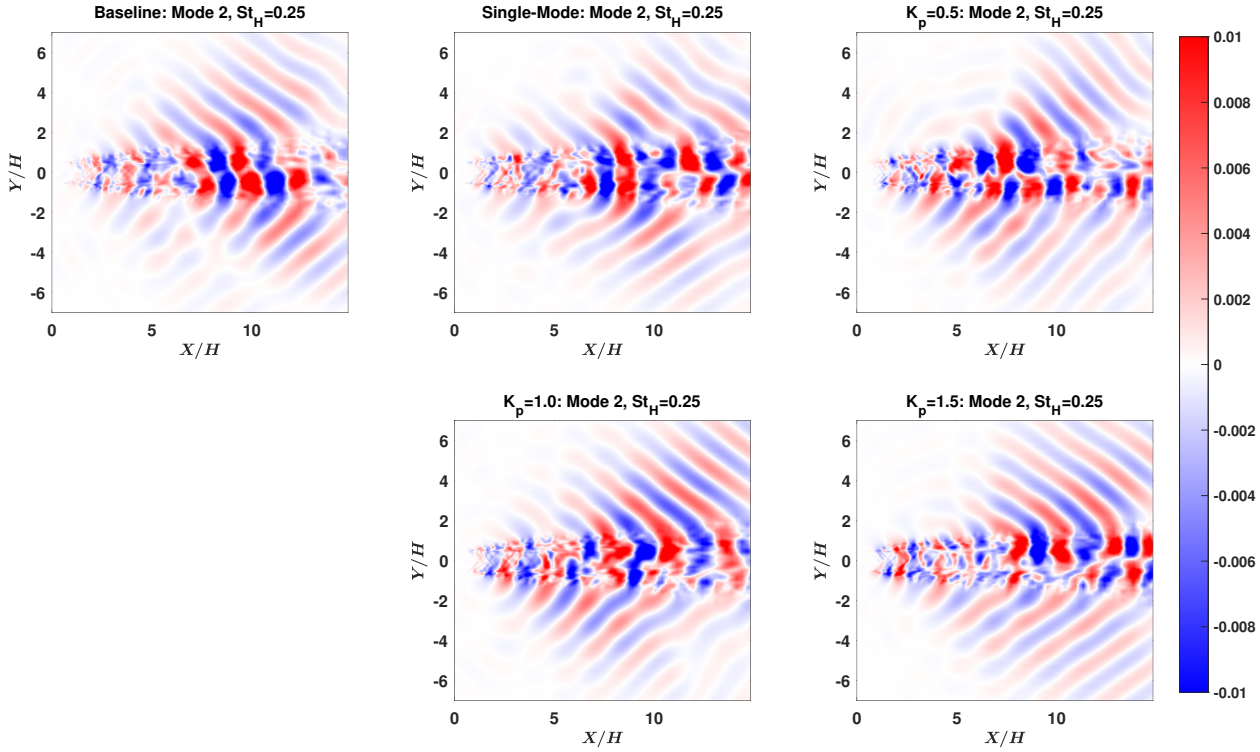

Figure 7.13 Second mode SPOD shapes at Strouhal number 0.25 for positive gain cases.

the wave packets take on an asymmetric structure compared to the symmetric structure in the baseline case. For $K_p = 1.0$, the wave packets keep a symmetric shape, but are more disrupted around $X/H = 8$ compared to baseline. The case of $K_p = 1.5$ is interesting in that the wave packets don't develop a coherent shape until $X/H = 10$.

7.2 Effect of Negative Gain

Cases are now considered where the proportional gain value is negative. Per Eq. 7.1, this should excite the jet in-phase with the naturally present disturbance, creating additive waves. It is not expected that this should reduce the noise, but to demonstrate the effects of small-amplitude in-phase forcing. Figure 7.14 shows the $\Delta p'_{RMS}$, where it is shown that there in still some reduction in the initial shear layer, but the region of reduction is significantly smaller comparing the cases with positive gain values in Fig. 7.4. Again, the shape of $\Delta p'_{RMS}$ takes a symmetric shape in the initial region since the actuators operate independently. Downstream, there is significant amplification of the pressure fluctuation, especially for the gain value of -1.0 between $X/H = 5 - 10$. Such amplification is not exhibited by the cases with positive gains or the single-mode case.

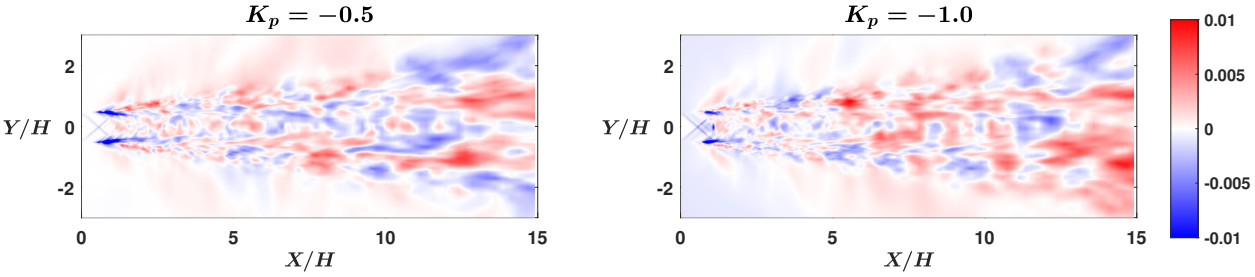

Figure 7.14 Contours of $\Delta p'_{RMS}$ for feed-forward cases with negative gain values; negative values indicate reduction.

Individual spectra along the initial shear layer are shown in Fig. 7.15. The probe locations here are exactly the same as in Fig. 7.5. Here, it is shown that the negative gain values do not reduce the peaks at Strouhal numbers 0.08 and 0.15. For the probe at $X/H = 0.4$, the high frequency fluctuations are not reduced with the negative gain values, whereas it was significantly reduced with positive gain values (see Fig. 7.5). Again, it is shown that

the feed-forward control is impacting a broad range of Strouhal numbers, but with negative gains, reduction is not observed.

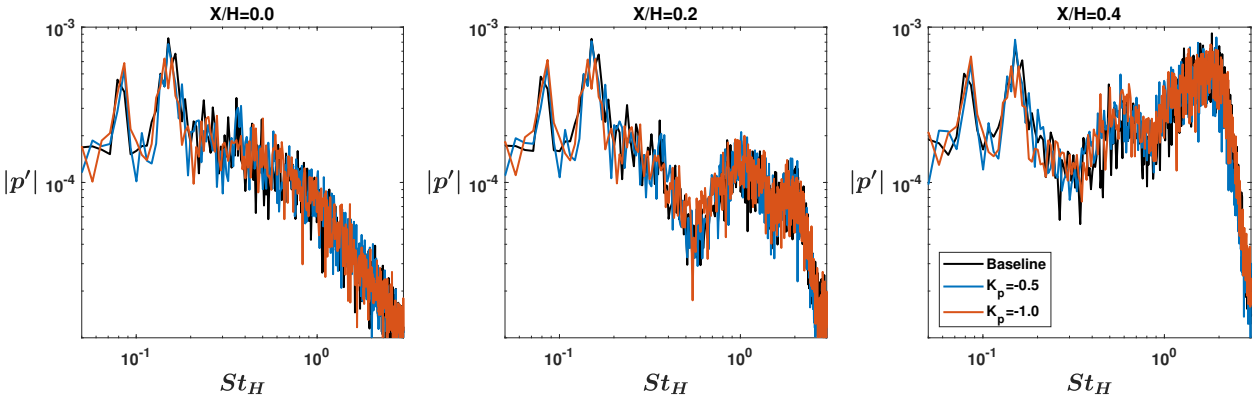

Figure 7.15 Minor plane shear layer spectra for negative gain cases.

Far field directivity is shown in Fig. 7.16. In the minor plane, the negative gains did not reduce noise by any meaningful amount. The gain of -0.5 had negligible differences from the baseline case. The gain value of -1.0 actually increased the peak-to-peak noise by around 1dB and created a general noise increase between directivity angles of 40° and 65°. This contrasts greatest with the case of $K_p = 1.0$ in Fig. 7.7, which shows a peak-to-peak noise reduction and general noise reduction for a broad range of directivity angles. In the major plane, there is some reduction in peak-to-peak noise of up to 0.5dB and a general reduction for emissivity angles below 50°.

Spectra at the peak emissivity angle in the minor plane is shown in Fig. 7.17. For $K_p = -0.5$, there is not much difference in spectra compared to the baseline, which isn't too surprising since the two directivity patterns were very similar. Looking at the spectra for $K_p = -1.0$, there is an increase in the SPL for a wide range of Strouhal numbers between 0.05 and 0.30, which caused the 1dB increase in OASPL. Again, it is shown that the feed-forward controller impacts a wide range of Strouhal numbers, which ultimately appears in the far field noise.

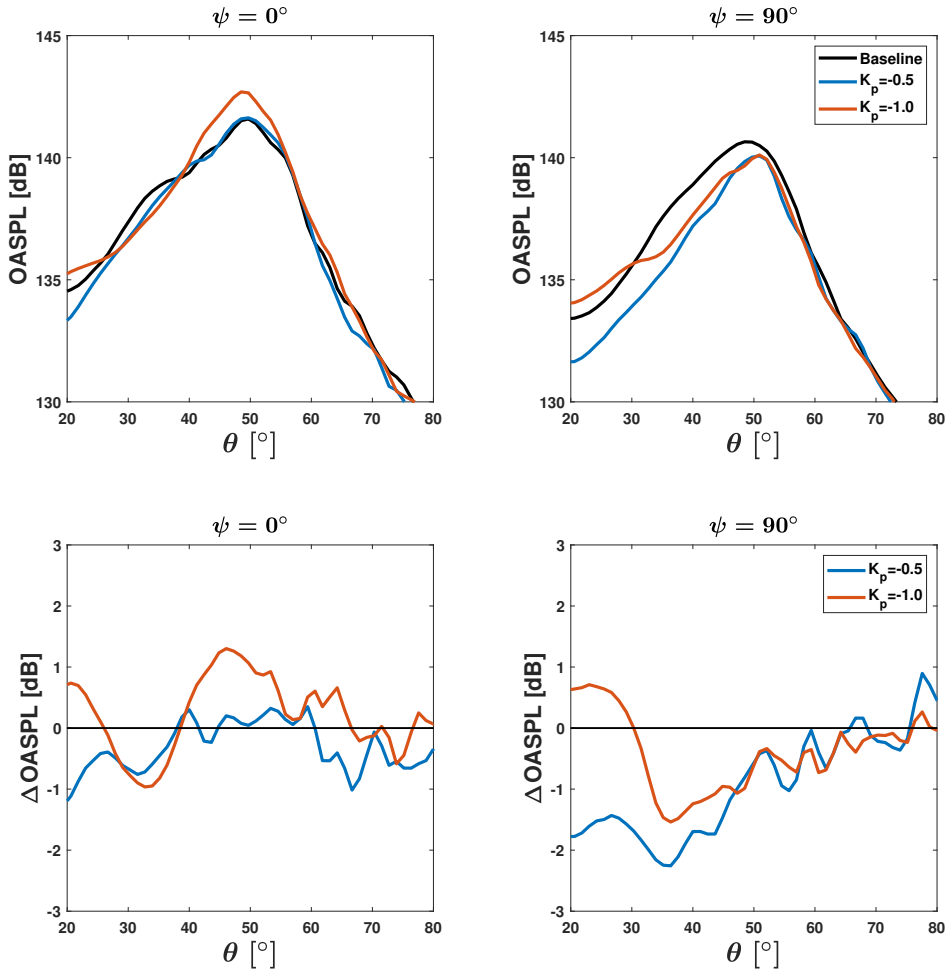

Figure 7.16 $OASPL$ (top) and $\Delta OASPL$ (bottom) for negative gains in the minor plane (left) and major plane (right).

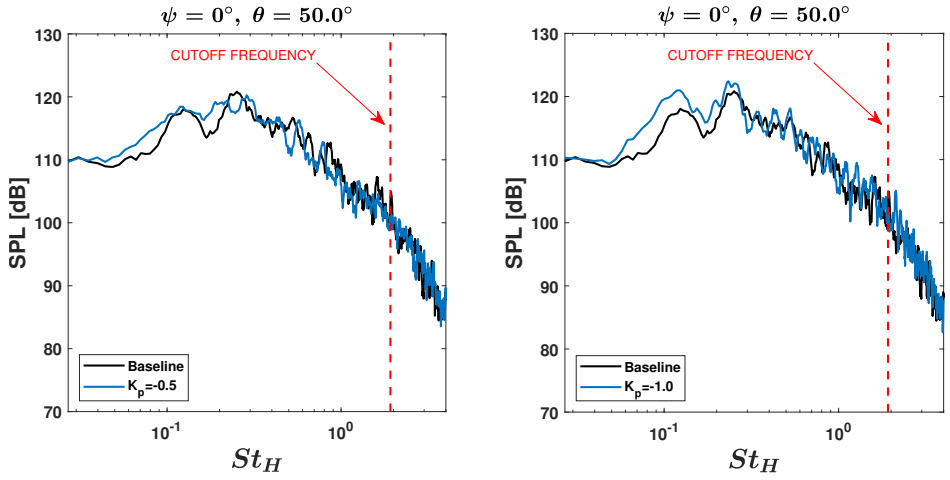

Figure 7.17 SPL spectra in the minor plane at the peak directivity angle for negative gain cases.

7.3 Conclusions from Feed-Forward Cases

In this work, a first principles approach is taken to reduce the noise in a supersonic rectangular jet via excitation. Since the large-scale turbulence in the jet can be decomposed into various frequency components, the concept of cancelling waves is implemented in the excitation prescription via a feed-forward controller. A total of 8 sensor-actuator pairs are placed on the upper and lower nozzle surfaces where the sensor reads an instantaneous pressure perturbation and the actuator responds with the opposite of that perturbation scaled with a proportional gain. Cases are first considered with positive gain values that should excite with cancelling waves. Negative gains are later considered to show the impacts of additive waves. This excitation strategy is unique because there are very limited prior publications using any sort of controller to drive the excitation.

For the cases with positive gain values, it is shown that the feed-forward controller reduces the RMS pressure fluctuations in the initial shear layer region. This contrasts with the more traditional single-mode excitation case, which actually increases the near nozzle fluctuations. The maximum reduction in near field fluctuations was 68% from the $K_p = 1.5$ case. The $K_p = 1.0$ case had only a slightly lower maximum near field reduction. Since a near 100% reduction is not attained, it is speculated that there exists a maximum reduction the feed-forward control can attain on its own. The near-nozzle spectra show a reduction for a wide range of Strouhal numbers, giving weight to the concept of cancelling waves. Analysis of the frequency components of the near field turbulence shows a general reduction in peak downstream fluctuations for a range of Strouhal numbers between 0.10 and 0.35 with the greatest reduction generally coming from the $K_p = 1.0$ case, which also exhibited the greatest downstream reduction in p'_{RMS}. SPOD analysis in the near field minor plane shows that the feed-forward controller is primarily impacting the first mode and reduces the dominant radiating waves at Strouhal numbers 0.15 and 0.25. This again contrasts with the single-mode comparison, which primarily impacts the second mode even though it has a significantly higher input energy. In the far field, the $K_p = 1.0$ case attained roughly a

0.5dB reduction in peak-to-peak noise compared to the baseline case. It also reduced the noise by up to 2dB for a wide range of directivity angles in the vicinity of the peak. This case highlights an overall improvement in noise reduction over the single-mode excitation case. All other feed-forward cases had similar levels of performance to the single-mode case. In the major plane, all feed-forward cases performed very similarly to the single-mode case and reduced the peak noise by up to 1dB.

For the cases with negative gain values, there is some reduction in the RMS pressure fluctuation in the near field, but it is not nearly as significant as the that of the positive gain cases. The downstream fluctuations are shown to be significantly amplified especially for the case of $K_p = -1.0$. Near-nozzle spectra did not exhibit the same reduction as the positive gain cases and actually created a slight amplification. In the far field, the gain of -0.5 had minimal impact on the minor plane OASPL and peak spectra. However, the gain value of -1.0 increased the peak noise by around 1dB and the spectra showed an amplification for a wide range of Strouhal numbers.

It is ultimately concluded that using the feed-forward controller can be effective for noise reduction if the proportional gain is around 1.0. Gains higher than 1.5 or lower than 0.5 are not recommended as they run the risk of either increasing the turbulent fluctuations over baseline in the case of the former or not generating enough cancellation in the case of the latter. Depending on directivity angle a far field noise reduction of up to 2dB can be obtained with a gain value of 1.0. Negative gain values are shown to increase the noise and are not recommended for noise reduction.

REFERENCES

[1] Salehian, S., and Mankbadi, R., "Numerical Simulation of Acoustic Shielding Effect on Supersonic Jets," *AIAA Propulsion and Energy Forum*, 2019, pp. Paper 2019–3822. https://doi.org/10.2514/6.2019-3822.

[2] Heeb, N., Mora, P., and Gutmark, E., "Investigation of the Noise from a Rectangular Supersonic Jet," *19th AIAA/CEAS Aeroacoustics Conference*, 2013. https://doi.org/10.2514/6.2013-2239.

[3] Doychak, J., "Department of Navy Jet Noise Reduction Project Overview," *Partners in Environmental Technology Technical Symposium & Workshop*, 2010.

[4] Mankbadi, R., and Liu, J. T. C., "Sound Generated Aerodynamically Revisited: Large-Scale Structures in a Turbulent Jet as a Source of Sound," *Philosophical Transactions of the Royal Society of London. Series A, Mathematical and Physical Sciences*, Vol. 311, No. 1516, 1984, pp. 183–217. https://doi.org/10.1098/rsta.1984.0024.

[5] Lighthill, M. J., "On sound generated aerodynamically I. General theory," *Proceedings of the Royal Society of London. Series A, Mathematical and Physical Sciences*, Vol. 211, No. 1107, 1952, pp. 564–587. https://doi.org/10.1098/rspa.1952.0060.

[6] Tam, C. K. W., and Tanna, H. K., "Shock Associated Noise of Supersonic Jets from Convergent-Divergent Nozzles," *Journal of Sound and Vibration*, Vol. 81, No. 3, 1982, pp. 337–358. https://doi.org/10.1016/0022-460X(82)90244-9.

[7] Tam, C. K. W., "Stochastic Model Theory of Broadband Shock Associated Noise from Supersonic Jets," *Journal of Sound and Vibration*, Vol. 116, No. 2, 1987, pp. 265–302. https://doi.org/10.1016/S0022-460X(87)81303-2.

[8] Gojon, R., Gutmark, E., and Mihaescu, M., "Antisymmetric Oscillation Modes in Rectangular Screeching Jets," *AIAA Journal*, Vol. 57, No. 8, 2019. https://doi.org/10.2514/1.J057514.

[9] Tyliszczak, A., and J., G. B., "DNS and LES of Excited Rectangular Jets," *International Symposium On Turbulence and Shear Flow Phenomena (TSFP-8)*, 2013. https://doi.org/10.1615/TSFP8.2200.

[10] Lighthill, M. J., "On sound generated aerodynamically II. Turbulence as a source of sound," *Proceedings of the Royal Society of London. Series A, Mathematical and Physical Sciences*, Vol. 222, 1954, pp. 1–32. https://doi.org/10.1098/rspa.1954.0049.

[11] Nichols, J. W., Ham, F. E., and Lele, S. K., "High-fidelity large-eddy simulation for supersonic rectangular jet noise prediction," *17th AIAA/CEAS Aeroacoustics Conference*, 2011. https://doi.org/10.2514/6.2011-2919.

[12] Lyrintzis, A. S., and Coderoni, M., "Overview of the Use of Large-Eddy Simulations in Jet Aeroacoustics," *AIAA Journal*, Vol. 58, No. 4, 2020. https://doi.org/10.2514/1.J058498.

[13] Bres, A., and Lele, S. K., "Modelling of jet noise: a perspective from large-eddy simulations," *Philosophical Transactions: Mathematical, Physical and Engineering Sciences*, Vol. 377, No. 2159, 2019, pp. 1–23. https://doi.org/10.1098/rsta.2019.0081.

[14] Bodony, D. J., and Lele, S. K., "Current Status of Jet Noise Predictions Using Large-Eddy Simulations," *AIAA Journal*, Vol. 46, No. 2, 2008. https://doi.org/10.2514/1.24475.

[15] Colonius, T., and Lele, S. K., "Computational aeroacoustics: progress on nonlinear problems of sound generation," *Progress in Aerospace Sciences*, Vol. 40, 2004, pp. 345–416. https://doi.org/10.1016/j.paerosci.2004.09.001.

[16] Tam, C. K. W., and Webb, J. C., "Dispersion-Relation-Preserving Finite Difference Schemes for Computational Acoustics," *Journal of Computational Physics*, Vol. 107, 1993, pp. 262–281. https://doi.org/10.1006/jcph.1993.1142.

[17] Hixon, R., Shih, S. H., and Mankbadi, R. R., "Evaluation of Boundary Conditions for Computational Aeroacoustics," *NASA Technical Memorandum 106645*, 1995.

[18] Hixon, R., "Evaluation of a High-Accuracy MacCormack-Type Scheme Using Benchmark Problems," *NASA Contractor Report 202324*, 1997.

[19] Bogey, C., Bailly, C., and Juve, D., "Computation of Flow Noise Using Source Terms in Linearized Euler's Equations," *AIAA Journal*, Vol. 40, No. 2, 2002. https://doi.org/10.2514/2.1665.

[20] Salehian, S., Good, P., Golubev, V. V., and Mankbadi, R. R., "An OpenFoam-Based LEE Solver for Prediction of Noise Generated by a Supersonic Jet Issued from a Rectangular Nozzle," *AIAA SciTech Forum*, 2023, pp. Paper 2023–0613. https://doi.org/10.2514/6.2023-0613.

[21] Mankbadi, R. R., Hixon, R., Shih, S., and Povinelli, L. A., "Use of Linearized Euler Equations for Supersonic Jet Noise Prediction," *AIAA Journal*, Vol. 36, No. 2, 1998, p. 140–147. https://doi.org/10.2514/2.7495.

[22] Shih, S. H., Hixon, D. R., and Mankbadi, R. R., "Zonal Approach for Prediction of Jet Noise," *Journal of Propulsion and Power*, Vol. 13, No. 6, 1997, p. 745–752. https://doi.org/10.2514/2.5247.

[23] Dahl, M. D., Hixon, R., and Mankbadi, R. R., "Computation of Large-Scale Structure Jet Noise Sources with Weak Nonlinear Effects Using Linear Euler," *9th AIAA/CEAS Aeroacoustics Conference and Exhibit*, 2003, pp. Paper 2003–3254. https://doi.org/10.2514/6.2003-3254.

[24] Gutmark, E., Schadow, K. C., and Bicker, C. J., "Near Acoustic Field and Shock Structure of Rectangular Supersonic Jets," *AIAA Journal*, Vol. 28, No. 7, 1990. https://doi.org/10.2514/3.25187.

[25] Samimy, M., Webb, N., Esfahani, A., and Leahy, R., "Perturbation-Based Active Flow Control in Overexpanded to Underexpanded Supersonic Rectangular Twin Jets," *Journal of Fluid Mechanics*, Vol. 959, 2023, p. Paper A13. https://doi.org/10.1017/jfm.2023.139.

[26] Raman, G., and Rice, E. J., "Instability modes excited by natural screech tones in a supersonic rectangular jet," *Physics of Fluids*, Vol. 6, 1994, p. 3999. https://doi.org/10.1063/1.868389.

[27] Chakrabarti, S., Gaitonde, D. V., and Unnikrishnan, S., "The Dynamics of Azimuthal Modes in Rectangular Jets," *AIAA Aviation 2020 Forum*, 2020, pp. Paper 2020–3000. https://doi.org/10.2514/6.2020-3000.

[28] Wu, G., Lele, S., and Jeun, J., "Towards Large Eddy Simulations of Supersonic Rectangular Jets including Screech," *25th AIAA/CEAS Aeroacoustics Conference*, 2019. https://doi.org/10.2514/6.2019-2520.

[29] Chakrabarti, S., Gaitonde, D., Unnikrishnan, S., Stack, C., Baier, F., Karnam, A., and Gutmark, E., "Turbulent Statistics of a Hot, Overexpanded Rectangular Jet," *Journal of Propulsion and Power*, Vol. 38, No. 3, 2022, p. 421–436. https://doi.org/10.2514/1.B38073.

[30] Crawley, M., Kearney-Fischer, M., and Samimy, M., "Control of a Supersonic Rectangular Jet Using Plasma Actuators," *18th AIAA/CEAS Aeroacoustics Conference*, 2012, pp. Paper 2012–2211. https://doi.org/10.2514/6.2012-2211.

[31] Rask, O., Kastner, J., and Gutmark, E., "Understanding How Chevrons Modify Noise in a Supersonic Jet with Flight Effects," *AIAA Journal*, Vol. 49, No. 8, 2011. https://doi.org/10.2514/1.J050628.

[32] Heeb, R., Gutmark, E., and Kailasanath, K., "Investigation of Chevron Penetration's

Effect on Supersonic Jet Noise Reduction," *AIAA Journal*, Vol. 54, No. 3, 2016. https://doi.org/10.2514/1.J054361.

[33] Mora, P., Baier, F., and Gutmark, E., "Acoustics from a Rectangular C-D Nozzle Exhausting over a Flat Surface," *AIAA SciTech Forum*, 2016, pp. Paper 2016–1884. https://doi.org/10.2514/6.2016-1884.

[34] Mankbadi, R. R., and Salehian, S., "A proposed wavy shield for suppression of supersonic jet noise utilizing reflections," *International Journal of Aeroacoustics*, Vol. 20, No. 1-2, 2021, pp. 4–34. https://doi.org/10.1177/1475472X20978385.

[35] Raman, G., and Rice, E., "Axisymmetric Jet Forced by Fundamental and Subharmonic Tones," *AIAA Journal*, Vol. 29, No. 7, 1989, p. 1114–1122. https://doi.org/10.2514/3.10711.

[36] Mankbadi, R. R., Shih, S. H., Hixon, D. R., and Povinelli, L. A., "Direct Computation of Sound Radiation by Jet Flow Using Large-Scale Equations," Technical Memorandum 106877, NASA, 1995.

[37] Samimy, M., Adamovich, I., Webb, B., Kastner, J., Hileman, J., Keshav, S., and Palm, P., "Development and Characterization of Plasma Actuators for High-Speed Jet Control," *Experiments in Fluids*, Vol. 37, 2004, p. 577–588. https://doi.org/10.1007/s00348-004-0854-7.

[38] Samimy, M., Kearny-Fischer, M., Kim, J.-H., and Sinha, A., "High-Speed and High-Reynolds-Number Jet Control Using Localized Arc Filament Plasma Actuators," *Journal of Propulsion and Power*, Vol. 28, No. 2, 2012, p. 269–280. https://doi.org/10.2514/1.B34272.

[39] Cluts, J., Kuo, C.-W., and Samimy, M., "Effects of Excitation Frequency and Azimuthal Mode on the Flow, Pressure, and Acoustic Fields of Supersonic Jets," *22nd*

AIAA/CEAS Aeroacoustics Conference, 2016, pp. Paper 2016–2940. https://doi.org/10.2514/6.2016-2940.

[40] Esfahani, A., Webb, N., and Samimy, M., "Coupling Modes in Supersonic Twin Rectangular Jets," *AIAA SciTech Forum*, 2021. https://doi.org/10.2514/6.2021-1292.

[41] Gaitonde, D. V., and Samimy, M., "Coherent structures in plasma-actuator controlled supersonic jets: Axisymmetric and mixed azimuthal modes," *Physics of Fluids*, Vol. 23, 2011, p. 095104. https://doi.org/10.1063/1.3627215.

[42] Gaitonde, D. V., "Analysis of the Near Field in a Plasma-Actuator-Controlled Supersonic Jet," *AIAA Journal of Propulsion and Power*, Vol. 28, No. 2, 2012, p. 281–292. https://doi.org/10.2514/1.B34289.

[43] Sinha, A., Towne, A., Colonius, T., Schlinker, R. H., Reba, R., Simonich, J. C., and Shannon, D. W., "Active Control of Noise from Hot Supersonic Jets," *AIAA Journal*, Vol. 56, No. 3, 2018, p. 933–948. https://doi.org/10.2514/1.J056159.

[44] Lakshmi Narasimha Prasad, A., and Unnikrishnan, S., "Effect of Plasma Actuator-Based Control on Flow-Field and Acoustics of Supersonic Rectangular Jets," *Journal of Fluid Mechanics*, Vol. 964, 2023, p. Paper A11. https://doi.org/10.1017/jfm.2023.354.

[45] Mankbadi, R. R., "On the Interaction Between Fundamental and Subharmonic Instability Waves in a Turbulent Round Jet," *Journal of Fluid Mechanics*, Vol. 160, 1985, p. 385–419. https://doi.org/10.1017/S0022112085003536.

[46] Lee, S., and Liu, J., "Multiple Coherent Mode Interaction in a Developing Round Jet," *AIAA 2nd Shear Flow Conference*, 1989, pp. Paper 1989–0967. https://doi.org/10.2514/6.1989-967.

[47] Dahl, M. D., and Mankbadi, R. R., "Analysis of Three-Dimensional, Nonlinear Development of Wave-Like Structure in a Compressible Round Jet," *8th AIAA/CEAS*

Aeroacoustics Conference & Exhibit, 2002, pp. Paper 2002–2451. https://doi.org/10.2514/6.2002-2451.

[48] Mankbadi, R. R., Malczewski, B. J., and Golubev, V. V., "Coherent Fundamental-Harmonic Interactions in a Compressible Shear Layer via Integral Nonlinear Instability Approach," *AIP Advances*, Vol. 12, No. 4, 2022, p. Paper 045127. https://doi.org/10.1063/5.0077291.

[49] Malczewski, B. J., Good, P., and Mankbadi, R. R., "3D Nonlinear Integral Technique Based on Linearized Euler Equations for the Prediction of Supersonic Rectangular Jet Noise," *AIAA SciTech 2023 Forum*, 2023. https://doi.org/10.2514/6.2023-0023.

[50] Malczewski, B. J., and Mankbadi, R. R., "Symmetric Mode-Mode Interactions in a Supersonic Rectangular Jet," *AIAA SciTech 2024 Forum*, 2024, pp. Paper 2024–2466. https://doi.org/10.2514/6.2024-2466.

[51] Arbey, H., and Ffowcs Williams, J. E., "Active cancellation of pure tones in an excited jet," *Journal of Fluid Mechanics*, Vol. 149, 1984, p. 445–454. https://doi.org/10.1017/S0022112084002743.

[52] Mankbadi, R. R., "Multifrequency Excited Jets," *Physics of Fluids A: Fluid Dynamics*, Vol. 3, No. 4, 1991, p. 595–605. https://doi.org/10.1063/1.858121.

[53] Natarajan, M., Freund, J. B., and Bodony, D. J., "Control of Supersonic Jet Noise Using Linear Feedback," *22nd AIAA/CEAS Aeroacoustics Conference*, 2016. https://doi.org/10.2514/6.2016-3055.

[54] Karban, U., Martini, E., and Jordan, P., "Modeling Closed-Loop Control of Installed Jet Noise Using Ginzburg-Landau Equation," *Flow, Turbulence and Combustion*, 2023. https://doi.org/10.1007/s10494-023-00508-0.

[55] Maia, I. A., Jordan, P., Cavalieri, V. G., Martini, E., and Silvestre, F. J., "Closed-loop control of forced turbulent jets," *arXiv*, 2020. https://doi.org/10.48550/arxiv.2009.09299.

[56] Malczewski, B. J., and Mankbadi, B. M., "Modeling Symmetric Coherent Mode Interactions in a Supersonic Rectangular Jet," *AIAA Journal*, Vol. 62, No. 4, 2023. https://doi.org/10.2514/1.J063421.

[57] Bogey, C., and Bailly, C., "Influence of nozzle-exit boundary-layer conditions on the flow and acoustic fields of initially laminar jets," *Journal of Fluid Mechanics*, Vol. 663, 2010, pp. 507–538. https://doi.org/10.1017/S0022112010003605.

[58] Speth, R. L., and Gaitonde, D. V., "Nozzle-Exit Boundary-Layer Effects on a Controlled Supersonic Jet," *AIAA Journal*, Vol. 53, No. 7, 2015. https://doi.org/10.2514/1.J053615.

[59] Malczewski, B. J., Mankbadi, R. R., and Golubev, V. V., "Control of a Compressible Shear Layer via Fundamental-Harmonic Interactions," *AIAA SciTech 2022 Forum*, 2021. https://doi.org/10.2514/6.2022-1151.

[60] Lee, K., and Liu, J. T. C., "Mixing Enhancement in High-Speed Turbulent Shear Layers Using Excited Coherent Modes," *AIAA Journal*, Vol. 36, No. 11, 1998, p. 2027–2035. https://doi.org/10.2514/2.303.

[61] Cohen, J., and Wygnanski, I., "The evolution of instabilities in the axisymmetric jet. Part 1. The linear growth of disturbances near the nozzle," *J. Fluid Mech.*, Vol. 176, 1987, p. 191–219. https://doi.org/10.1017/S0022112087000636.

[62] Cohen, J., and Wygnanski, I., "The evolution of instabilities in the axisymmetric jet. Part 2. The flow resulting from the interaction between two waves," *J. Fluid Mech.*, Vol. 176, 1987, p. 221–235. https://doi.org/10.1017/S0022112087000624.

[63] Viswanath, K., Johnson, R., Corrigan, A., Kailasanath, K., Mora, P., Baier, F., and Gutmark, E., "Flow Statistics and Noise of Ideally Expanded Rectangular and Circular Jets," *AIAA Journal*, Vol. 55, No. 10, 2017, p. 3425–3439. https://doi.org/10.2514/1.J055717.

[64] Salehian, S., and Mankbadi, R., "Jet Noise in Airframe Integration and Shielding," *Applied Sciences*, Vol. 10, No. 2, 2020, p. 511. https://doi.org/10.3390/app10020511.

[65] Malczewski, B., "A Reduced-Order Model Bi-Modal Excitation of a Supersonic Planar Jet," Master's thesis, Embry-Riddle Aeronautical Univ., Daytona Beach, FL, Aug 2021.

[66] Visbal, M., and Gaitonde, D., "High-Order-Accurate Methods for Complex Unsteady Subsonic Flows," *AIAA Journal*, Vol. 37, No. 10, 1999, pp. 1231–1239. https://doi.org/10.2514/2.591.

[67] Pletcher, R. H., Tannehill, J. C., and Anderson, D., *Computational Fluid Mechanics and Heat Transfer*, CRC Press, 2012.

[68] Unnikrishnan, S., and Gaitonde, D. V., "Acoustic, hydrodynamic and thermal modes in a supersonic cold jet," *Journal of Fluid Mechanics*, Vol. 800, 2016, pp. 387–432. https://doi.org/10.1017/jfm.2016.410.

[69] Roe, P. L., "Approximate Riemann Solvers, Parameter Vectors, and Difference Schemes," *Journal of Computational Physics*, Vol. 43, No. 2, 1981, p. 357–372. https://doi.org/10.1016/0021-9991(81)90128-5.

[70] Van Leer, B., "Towards the Ultimate Conservative Difference Scheme. V. A Second-Order Sequel to Godunov's Method," *Journal of Computational Physics*, Vol. 32, No. 1, 1979, p. 101–136. https://doi.org/10.1016/0021-9991(79)90145-1.

[71] Pulliam, T. H., and Chaussee, D., "A Diagonal Form of an Implicit Approximate-

Factorization Algorithm," *Journal of Computational Physics*, Vol. 39, No. 2, 1981, p. 347–363. https://doi.org/10.1016/0021-9991(81)90156-X.

[72] Di Francescantonio, P., "A New Boundary Integral Formulation for the Prediction of Sound Radiation," *Journal of Sound and Vibration*, Vol. 202, No. 4, 1997, pp. 491–509. https://doi.org/10.1006/jsvi.1996.0843.

[73] Spalart, P. R., and Shur, M. L., "Variants of the Ffowcs Williams-Hawkings equation and their coupling with simulations of hot jets," *International Journal of Aeroacoustics*, Vol. 8, No. 5, 2009. https://doi.org/10.1260/147547209788549280.

[74] Mendez, S., Shoeybi, M., Lele, S. K., and Moin, P., "On the use of the Ffowcs Williams-Hawkings equation to predict far-field jet noise from large-eddy simulations," *International Journal of Aeroacoustics*, Vol. 12, No. 1-2, 2013, pp. 1–20. https://doi.org/10.1260/1475-472X.12.1-2.1.

[75] Lyrintzis, A., "Surface integral methods in computational aeroacoustics - From the (CFD) near-field to the (Acoustic) far-field," *International Journal of Aeroacoustics*, Vol. 2, No. 2, 2003, pp. 95–128. https://doi.org/10.1260/147547203322775498.

[76] Brentner, K. S., and Farassat, F., "Analytical Comparison of the Acoustic Analogy and Kirchhoff Formulation for Moving Surfaces," *AIAA Journal*, Vol. 36, No. 8, 1998. https://doi.org/10.2514/2.558.

[77] Welch, P. D., "The Use of Fast Fourier Transform for the Estimation of Power Spectra: A Method Based on Time Averaging Over Short, Modified Periodograms," *IEEE Transactions on Audio and Electroacoustics*, Vol. 15, No. 2, 1967, pp. 70–73. https://doi.org/10.1109/TAU.1967.1161901.

[78] Shur, M. L., Spalart, P. R., and Strelets, M. K., "Noise prediction for increasingly complex jets. Part I: Methods and tests," *International Journal of Aeroacoustics*, Vol. 4, No. 3-4, 2005, pp. 213–246. https://doi.org/10.1260/1475472054771376.

[79] Mendez, S., Shoeybi, M., Lele, S. K., and Moin, P., "On the use of the Ffowcs Williams-Hawking equation to predict far-field jet noise from large-eddy simulations," *International Journal of Aeroacoustics*, Vol. 12, No. 1-2, 2013. https://doi.org/10.1260/1475-472X.12.1-2.1.

[80] Tam, C. K. W., and Webb, J. C., "Dispersion-Relation-Preserving Finite Difference Schemes for Computational Acoustics," *Journal of Computational Physics*, Vol. 107, 1993, pp. 262–281. https://doi.org/10.1006/jcph.1993.1142.

[81] Bezanson, J., Edelman, A., Karpinski, S., and Shah, V. B., "Julia: A fresh approach to numerical computing," *SIAM Review*, Vol. 59, No. 1, 2017, pp. 65–98. https://doi.org/10.1137/141000671, URL https://epubs.siam.org/doi/10.1137/141000671.

[82] Salehian, S., Malczewski, B. J., and Mankbadi, R. R., "Coherent Structure in a Rectangular Supersonic Jet and Its Role in Peak Noise Radiation," *AIAA SciTech 2024 Forum*, 2024, pp. Paper 2024–2631. https://doi.org/10.2514/6.2024-2631.

[83] Schmidt, O. T., and Colonius, T., "Guide to Spectral Proper Orthogonal Decomposition," *AIAA Journal*, Vol. 58, No. 3, 2020. https://doi.org/10.2514/1.J058809.

[84] Jordan, P., and Colonius, T., "Wave Packets and Turbulent Jet Noise," *Annual Review of Fluid Mechanics*, Vol. 45, No. 1, 2013, pp. 173–195. https://doi.org/10.1146/annurev-fluid-011212-140756.

[85] Malczewski, B. J., Golubev, V. V., Mankbadi, R. R., and Salehian, S., "Large-Eddy Simulations of Bi-Model Excitation in a Supersonic Rectangular Jet," *30th AIAA/CEAS Aeroacoustics Conference 2024*, 2024. https://doi.org/10.2514/6.2024-3148.

[86] Malczewski, B. J., Salehian, S., Golubev, V. V., and Mankbadi, R. R., "Large-Eddy Simulations of Noise Reduction via Fundamental-Harmonic Interactions in a Supersonic Rectangular Jet," *International Journal of Aeroacoustics*, 2024. To be published.

PUBLICATIONS

1. Malczewski, B.J., Mankbadi, R.R., "Modeling Symmetric Coherent Mode Interactions in a Supersonic Rectangular Jet," AIAA Journal, December 2023, https://doi.org/10.2514/1.J063421

2. Mankbadi, R.R., Malczewski, B.J., Golubev, V.V., 03/2022, "Coherent fundamental-harmonic interactions in a compressible shear layer via integral nonlinear instability approach," AIP Advances 12, March 2022, https://doi.org/10.1063/5.0090544.

3. Malczewski, B.J., Mankbadi, R.R., Golubev, V.V.," Control of a Compressible Shear Layer Via Fundamental-Harmonic Interactions," AIAA SciTech 2022, December 2021, https://doi.org/10.2514/6.2022-1151.

4. Malczewski, B.J., Good, P.P., Mankbadi, R.R., "3D Nonlinear Integral Technique Based on Linearized Euler Equations for the Prediction of Supersonic Rectangular Jet Noise Sources," AIAA SciTech 2023, January 2023, https://doi.org/10.2514/6.2023-0023.

5. Malczewski, B.J., Mankbadi, R.R., Golubev, V.V., Salehian, S., Prasad, C., "Large-Eddy Simulations of Fundamental-Harmonic Coherent Structure Interactions in a Supersonic Rectangular Jet," AIAA SciTech 2024, January 2024, https://doi.org/10.2514/6.2024-2308.

6. Malczewski, B.J., Mankbadi, R.R., "Symmetric Mode-Mode Interactions in a Supersonic Rectangular Jet," AIAA SciTech 2024, January 2024, https://doi.org/10.2514/6.2024-2466.

7. Salehian, S., Malczewski, B.J., Mankbadi, R.R., "Coherent Structure in a Rectangular Supersonic Jet and Its Role in Peak Noise Radiation," AIAA SciTech 2024, January 2024, https://doi.org/10.2514/6.2024-2631.

8. Malczewski, B. J., Golubev, V. V., Mankbadi, R. R., Salehian, S., "Large-Eddy Simulations of Bi-Modal Excitation in a Supersonic Rectangular Jet," 30th AIAA/CEAS Aeroacoustics Conference, June 2024, https://doi.org/10.2514/6.2024-3148.

9. Malczewski, B. J., MacKunis, W., Mankbadi, R. R., Salehian, S., "Pure Cancellation of Noise in a Supersonic Rectangular Jet," AIAA Aviation Forum, July 29-August 2 2024, https://doi.org/10.2514/6.2024-3594.

10. Malczewski, B. J., Salehian, S., Golubev, V. V., Mankbadi, R. R., "Large-Eddy Simulations of Noise Reduction via Fundamental-Harmonic Interactions in a Supersonic Rectangular Jet," International Journal of Aeroacoustics, (submitted).

11. Malczewski, B. J., MacKunis, W., Mankbadi, R. R., Salehian, S., "Noise Reduction in a Supersonic Rectangular Jet via Feed-Forward Control," AIAA Journal, (submitted).